

January 2015

# A Pseudo Non-Cartesian Pulse Sequence For Hyperpolarized Xenon-129 Gas MRI of Rodent Lungs At Low Magnetic Field Strength

Krzysztof Wawrzyn

*The University of Western Ontario*

Supervisor

Giles Edmund Santyr

*The University of Western Ontario*

Graduate Program in Medical Biophysics

A thesis submitted in partial fulfillment of the requirements for the degree in Master of Science

© Krzysztof Wawrzyn 2014

Follow this and additional works at: <http://ir.lib.uwo.ca/etd>



Part of the [Medical Biophysics Commons](#)

---

## Recommended Citation

Wawrzyn, Krzysztof, "A Pseudo Non-Cartesian Pulse Sequence For Hyperpolarized Xenon-129 Gas MRI of Rodent Lungs At Low Magnetic Field Strength" (2014). *Electronic Thesis and Dissertation Repository*. Paper 2606.

**A PSEUDO NON-CARTESIAN PULSE SEQUENCE FOR  
HYPERPOLARIZED XENON-129 GAS MRI OF RODENT  
LUNGS AT LOW MAGNETIC FIELD STRENGTH**

**(Thesis format: Monograph)**

**by**

**Krzysztof Wawrzyn**

**Graduate Program in Medical Biophysics**

**A thesis submitted in partial fulfillment  
of the requirements for the degree of  
Master of Science**

**The School of Graduate and Postdoctoral Studies  
The University of Western Ontario  
London, Ontario, Canada**

**© Krzysztof Wawrzyn 2014**

## Abstract

**Background:** Early diagnosis of radiation-induced lung injury (RILI) following radiation therapy is critical for prevention of permanent lung damage. Pulmonary imaging using magnetic resonance imaging (MRI) of the apparent diffusion coefficient (ADC) of hyperpolarized xenon ( $^{129}\text{Xe}$ ) gas shows promise for early measurement of RILI.

**Methods:** An ultra-short echo time imaging sequence based on a pseudo-Cartesian  $k$ -space trajectory, known as *Sectoral*, is implemented at low magnetic field (0.07 T) for efficient use of the non-renewable magnetization of hyperpolarized  $^{129}\text{Xe}$  gas. A pilot study was performed to demonstrate the feasibility of ADC mapping using the *Sectoral* sequence on healthy and 2-weeks post irradiated rats.

**Results:** A significant ( $p < 0.05$ ) correlation between *mean* ADC values from *Sectoral* ADC maps and the mean linear intercept ( $L_m$ ), as a measure of interalveolar wall distance, from histological sections of the lungs was observed ( $p = 0.0061$ ) and a significant ( $p < 0.05$ ) separation between healthy and irradiated lungs was observed with full width at half maximum ADC ( $p = 0.0317$ ).

**Conclusion:** *Sectoral* MRI with  $^{129}\text{Xe}$  is feasible in rats. Decreases in ADC were measured following lung irradiations which correlate with  $L_m$ .

## Keywords

Hyperpolarized xenon gas,  $^{129}\text{Xe}$  MRI, Radiation-Induced Lung Injury, RILI, low field MRI,  $T_1$  mapping, ADC mapping,  $p_A\text{O}_2$  mapping, magnetic field gradient monitor, *Sectoral*.

## Acknowledgments

I would like to express my sincere gratitude to the following individuals whose support made this thesis possible:

- My supervisor, Dr. Giles Santyr, for allowing me the opportunity to conduct research in his group at Robarts Research Institute at Western University. His mentorship provided me with a well-rounded educational experience allowing me to develop various skills. I thank him for his expertise, guidance, encouragement, and patience throughout my thesis research.
- My advisory committee, Dr. Blaine Chronik and Dr. Charles McKenzie, for finding the time to provide guidance and support for my graduate work.
- Dr. Alexei Ouriadov, for his guidance with almost all aspects of my research. He has been a great resource by helping me with various questions on MRI physics, pulse sequences, and data processing. Working with him has provided me with a unique opportunity to gain a wider range of practical experience. I consider working with him to have been an enormous benefit.
- Elaine Hegarty for assisting me in every *in vivo* experiment with all animal preparation, running the ventilator, and performing histology. She also greatly contributed to rat irradiations and improving the xenon polarizer to a level that produced a workable signal.
- Dr. Eugene Wong for contributing towards the rat irradiations.
- All of my fellow colleagues and past/present members of the Santyr lab for providing support and helpful discussions. In particular, Ozkan Doganay, Susannah Hickling, Adam Farag, and Yonathan Araya.
- My parents, Irena and Stanislaw Wawrzyn, for their support and faith in me throughout all of my studies.
- My fiancée, Christine Tarapacki, for her unwavering love, quiet patience, and understanding.
- The following sources of funding: NSERC, ORF and CIHR.

# Table of Contents

Abstract .....	ii
Acknowledgments.....	iii
Table of Contents .....	iv
List of Tables .....	vii
List of Figures .....	viii
List of Appendices .....	xiv
List of Abbreviations and Symbols.....	xv
Chapter 1 : Introduction .....	1
1 Introduction.....	1
1.1 Rationale and Motivation .....	1
1.2 Pulmonary Physiology.....	2
1.2.1 Healthy Lungs.....	2
1.2.2 Lung Cancer and Radiation Therapy .....	2
1.2.3 Radiation-induced Lung Injury (RILI) .....	3
1.2.4 Animal Models of RILI .....	4
1.3 Diagnostic Measurements of RILI .....	5
1.3.1 Pulmonary Function Tests .....	5
1.3.2 Chest Radiography/Computed Tomography .....	6
1.3.3 Nuclear Medicine Methods/PET/SPECT .....	6
1.3.4 Magnetic Resonance Imaging.....	7
1.3.5 Hyperpolarized MRI of RILI.....	7
1.4 Physics of Nuclear Magnetic Resonance (NMR).....	8
1.4.1 Nuclear Spin and Magnetic Moments.....	8
1.4.2 Quantum Mechanical Description of NMR.....	9
1.4.3 Polarization and Bulk Magnetization.....	10
1.4.4 Dynamics of Magnetization in the Presence of a Time-Varying Applied Magnetic Field .....	12
1.4.5 Spin Relaxation Mechanisms.....	14
1.4.6 MRI Signal Detection and Measurement.....	16
1.5 Hyperpolarized Gas Production .....	17
1.5.1 Properties of $^3\text{He}$ and $^{129}\text{Xe}$ .....	18
1.5.2 Spin Exchange Optical Pumping of $^{129}\text{Xe}$ .....	19
1.5.3 Practical Considerations with Hyperpolarized $^{129}\text{Xe}$ .....	20
1.6 Hyperpolarized $^{129}\text{Xe}$ Imaging at Low Magnetic Field.....	20
1.6.1 Low Field Considerations for $^{129}\text{Xe}$ MRI.....	20
1.6.2 Spatial Frequency and Phase-encoding .....	21
1.6.3 Pulse Sequence Considerations for Hyperpolarized $^{129}\text{Xe}$ .....	26
1.6.4 Signal-to-noise Ratio in Hyperpolarized MRI.....	27
1.6.5 Signal Decay during Hyperpolarized $^{129}\text{Xe}$ Imaging.....	28
1.6.6 Eddy Currents .....	34
1.6.7 Cartesian Acquisitions .....	35
1.6.8 Non-Cartesian Acquisitions .....	37
1.6.9 Pseudo-Cartesian Imaging .....	37

1.7	<i>Sectoral</i> Pulse Sequence for Hyperpolarized $^{129}\text{Xe}$ in the Low-Field MRI System .....	39
1.7.1	Gradient Waveform Characterization .....	39
1.7.2	<i>Sectoral</i> Pulse Sequence .....	40
1.7.3	$T_1$ and $p_A\text{O}_2$ Mapping .....	41
1.7.4	Diffusion Mapping .....	41
1.7.5	Post Processing .....	42
1.8	Hypothesis and Objectives .....	43
1.9	Thesis Outline .....	43
Chapter 2 : Methodology .....		46
2	Introduction .....	46
2.1	Xenon-129 Polarization and Delivery .....	46
2.2	Phantom Preparation .....	47
2.3	Animal Preparation .....	48
2.3.1	Irradiations .....	48
2.3.2	Surgical Procedure .....	49
2.3.3	Ventilation .....	50
2.4	Low Field MRI .....	51
2.5	<i>In Vitro</i> FGRE MRI Experiments .....	53
2.6	<i>In Vitro</i> <i>Sectoral</i> MRI Experiments .....	54
2.6.1	$T_1$ and $p_A\text{O}_2$ Experiments .....	54
2.6.2	ADC Experiments .....	55
2.7	<i>In Vivo</i> MRI Experiments .....	56
2.7.1	ADC Experiments .....	56
2.8	Histological Analysis .....	56
2.9	Pre-scan Calibrations .....	57
2.10	MRI SNR Efficiency Calculations .....	59
2.11	Data Processing and Analysis .....	60
2.11.1	$T_1$ and $p_A\text{O}_2$ Mapping .....	60
2.11.2	ADC Mapping .....	61
2.12	<i>In vivo</i> Statistical Analysis .....	61
Chapter 3 : Results .....		63
3	Introduction .....	63
3.1	<i>In Vitro</i> .....	63
3.1.1	FGRE versus <i>Sectoral</i> Proton Imaging .....	63
3.1.2	FGRE versus <i>Sectoral</i> $^{129}\text{Xe}$ Imaging .....	64
3.1.3	<i>Sectoral</i> ADC Measurements .....	65
3.1.4	<i>Sectoral</i> $T_1$ and $p_A\text{O}_2$ Measurements .....	69
3.2	<i>In Vivo</i> .....	74
3.2.1	FGRE and <i>Sectoral</i> $^{129}\text{Xe}$ Imaging .....	74
3.2.2	<i>Sectoral</i> ADC Measurements of RILI .....	75
Chapter 4 : Discussion and Future Work .....		79
4	Introduction .....	79
4.1	Gradient Waveform Mapping .....	79
4.2	Comparisons of FGRE and <i>Sectoral</i> .....	80
4.3	ADC of Phantoms .....	83

4.4	T <sub>1</sub> and p <sub>A</sub> O <sub>2</sub> of Phantoms.....	84
4.5	Ventilation Imaging of Rat Lungs .....	85
4.6	ADC of Rat Lungs.....	85
4.7	Summary of Thesis.....	89
	References.....	90
	Appendix A: Gradient Waveform Mapping .....	96
	A.1 Methodology.....	96
	A.2 Results .....	100
	Appendix B: Histological Interpretation.....	102
	Appendix C: Animal Use Protocol Approval .....	103
	Curriculum Vitae .....	104

## List of Tables

Table 1-1: Dependence of SNR of field strength, $B_0$ (adapted from (47)).	27
Table 1-2: Statistical characteristics of 2-D trajectories (59).	38
Table 1-3: Statistical characteristics of 3-D trajectories (59).	38
Table 2-1: Representative tip angles with corresponding pulse width, for a series of 16 VFA RF pulses used in <i>SB-Sectoral</i> .	58
Table 3-1: Summary of $^1\text{H}$ resolution phantom imaging results.	64
Table 3-2: Summary of $^{129}\text{Xe}$ syringe phantom imaging results.	65
Table 3-3: Mean and standard deviation of ADC values with corresponding FWHM ADC values obtained from the Gaussian distribution of each ADC histogram, for each ADC map. Data reported were obtained from $^{129}\text{Xe-N}_2$ mixture filled syringe using <i>MB-Sectoral</i> and two <i>SB-Sectoral</i> trials.	67
Table 3-4: Mean and standard deviation of $T_1$ values with corresponding FWHM ADC values obtained from the Gaussian distribution of each $T_1$ histogram, for each $T_1$ map. Data reported were obtained from $^{129}\text{Xe-O}_2$ mixture filled syringe using <i>MB-Sectoral</i> and two <i>SB-Sectoral</i> trials.	72
Table 3-5: Mean and standard deviation of $p_{\text{A}}\text{O}_2$ values with corresponding FWHM ADC values obtained from the Gaussian distribution of each $p_{\text{A}}\text{O}_2$ histogram, for each $p_{\text{A}}\text{O}_2$ map. Data reported were obtained from $^{129}\text{Xe-O}_2$ mixture filled syringe using <i>MB-Sectoral</i> and two <i>SB-Sectoral</i> trials.	72
Table 3-6: <i>In vivo</i> comparison using the different sequences.	75
Table 3-7: <i>In vivo</i> mean of ADC values, FWHM ADC values, and $L_m$ from histological analysis.	77
Table B-1: Representative average $L_m$ values of each rat cohort.	102



## List of Figures

Figure 1-1: Schematic of airway branching in the lung, adapted from (1).....	2
Figure 1-2: Splitting of spin states for a spin $\frac{1}{2}$ system in an external magnetic field $\vec{B}_0$ . .....	10
Figure 1-3: A Boltzmann distribution of individual magnetic moments in a macroscopic sample can be expressed as a single net magnetization vector along the $z$ -axis (adapted from (35))......	12
Figure 1-4: The motion of the magnetization as observed in the laboratory frame of reference in response to an excitation pulse of $90^\circ$ .....	14
Figure 1-5: An example of an MRI pulse sequence diagram. The vertical axis is the amplitude and the horizontal axis is time. A pair of frequency and phase encode gradients are shown prior to the echo of the MRI signal. A readout gradient on $G_x$ is switched on when the echo signal appears and the signal is digitized during data acquisition (DAQ).23	23
Figure 1-6: The 2-D $k$ -space matrix in Cartesian coordinates. ....	24
Figure 1-7: The diffusion bipolar trapezoidal gradient with amplitude $G$ , ramp time $\tau$ , lobe duration $\delta$ , and diffusion time $\Delta$ . ....	32
Figure 1-8: A schematic of gradient pulses. The eddy currents induce a magnetic field that adds to the ideal gradient waveform to form a manifested response. A compensated gradient waveform (i.e. pre-emphasis) reduces the effect of eddy currents in the desired waveform. ....	35
Figure 1-9: A pulse sequence diagram (left) and $k$ -space trajectory (right) for the example of a FGRE Cartesian $k$ -space acquisition. ....	36
Figure 1-10: Pure phase-encoding gradient waveforms for a <i>Sectoral</i> sequence of ideal $G_x$ (left) and ideal $G_y$ (right).....	39

Figure 1-11: An example of a pulse sequence diagram (left) of a single $k$ -space trajectory (blue sector) for a 16-sector MB- <i>Sectoral</i> acquisition (right). .....	41
Figure 1-12: A diagram of the diffusion-weighted <i>Sectoral</i> pulse sequence including a bipolar trapezoidal gradient pulse with diffusion time, $\Delta$ , lobe duration, $\delta$ , ramp time, $\tau$ , and gradient magnitude, $G$ . .....	42
Figure 2-1: Photograph of the acrylic resolution phantom (left) and a corresponding schematic diagram with shown dimensions. The $^{129}\text{Xe}$ gas resides in the empty space of the phantom container. ....	48
Figure 2-2: Photograph of the flow-through syringe phantom. ....	48
Figure 2-3: Photograph of $^{60}\text{Co}$ irradiator with animal positioning system and isoflurane vaporizer (left). Positioning system seen from top view showing custom-built animal positioning stage and lead collimator with rat in prone (top-right) and supine (bottom-right) positions. ....	49
Figure 2-4: Animal ventilation control unit with gas reservoir. ....	51
Figure 2-5: Low magnetic field (74 mT) MRI system. ....	52
Figure 2-6: Transmit only/receive only saddle RF coil tuned to 0.883 MHz ( $^{129}\text{Xe}$ ) or 3.163 MHz ( $^1\text{H}$ ). ....	52
Figure 2-7: Insertable RF coil with tracheostomized rat. ....	53
Figure 2-8: The VFA calibrated signals from a typical $^{129}\text{Xe}$ <i>Sectoral</i> phantom measurement with appropriate power leading to a constant response with less than 5% variability. ....	58
Figure 2-9: Representative FID for $^{129}\text{Xe}$ in a phantom with a measured $T_2^*$ of 192 ms. $T_2^*$ was calculated offline in MATLAB with exponential curve fitting. ....	59
Figure 3-1: $^1\text{H}$ resolution phantom images acquired with the FGRE (left) and SB- <i>Sectoral</i> (right) sequence. ....	64

Figure 3-2:  $^{129}\text{Xe}$  flow-through syringe phantom images acquired with the FGRE (left), SB-*Sectoral* (middle), and MB-*Sectoral* (right) sequences. .... 65

Figure 3-3: Representative diffusion-weighted MB-*Sectoral*  $^{129}\text{Xe}$  phantom results filled with pure  $^{129}\text{Xe}$ . Shown are: un-weighted image (top-left), diffusion-weighted image (top-right), corresponding ADC-map (bottom-left) and histogram (bottom-right). *Mean* ADC =  $0.051 \pm 0.003 \text{ cm}^2/\text{s}$  and FWHM ADC =  $0.008 \text{ cm}^2/\text{s}$ . .... 66

Figure 3-4: Representative diffusion-weighted MB-*Sectoral*  $^{129}\text{Xe}$  phantom results with 6.4 ml of  $\text{N}_2$  added. Shown are: un-weighted image (top-left), diffusion-weighted image (top-right), corresponding ADC-map (bottom-left) and histogram (bottom-right). *Mean* ADC =  $0.073 \pm 0.015 \text{ cm}^2/\text{s}$  and FWHM ADC =  $0.037 \text{ cm}^2/\text{s}$ . .... 67

Figure 3-5: Results of the phantom experiments using MB-*Sectoral*. Plots of ADC pixel average versus prepared  $\text{N}_2$  volume for five scans (left). The vertical error bars represent the pixel deviation in each map represented from the ROI. The horizontal error bars correspond to the precision of the prepared  $\text{N}_2$  volumes ( $\pm 0.2 \text{ ml}$ ) in the syringe. Reciprocals of *mean* ADC values (right) with significant ( $p < 0.05$ ) linear regression fit. Calculated  $p = 0.024$  and  $r^2 = 0.86$ . .... 68

Figure 3-6: Results of the two phantom experiments using SB-*Sectoral*. Plots of ADC pixel average versus prepared  $\text{N}_2$  volume for seven scans (top row). The vertical error bars represent the pixel deviation in each map represented from the ROI. The horizontal error bars correspond to the precision of the prepared  $\text{N}_2$  volumes ( $\pm 0.2 \text{ ml}$ ) in the syringe. Reciprocals of *mean* ADC values (bottom row) with significant ( $p < 0.05$ ) linear regression fit. For experiment 1,  $p = 0.001$  and  $r^2 = 0.90$  and experiment 2,  $p = 0.004$  and  $r^2 = 0.84$ . .... 68

Figure 3-7: Representative *Sectoral*  $T_1$ -maps before (left) and after (right)  $B_1$  correction using a  $B_1$  map (middle). .... 70

Figure 3-8: Representative  $T_1$ -weighted MB-*Sectoral*  $^{129}\text{Xe}$  phantom experiment filled with pure  $^{129}\text{Xe}$ . Un-weighted image (top-left),  $T_1$ -weighted image (top-right),

corresponding  $T_1$ -map (middle-left) & histogram (bottom-left), and the corresponding  $p_{AO_2}$ -map (middle-right) & histogram (bottom-right). Mean  $T_1 = 41.21 \pm 1.72$  s, FWHM  $T_1 = 4.05$  s, mean  $p_{AO_2} = 0.0057 \pm 0.003$  atm, and FWHM  $p_{AO_2} = 0.0006$  atm. .... 71

Figure 3-9: Representative  $T_1$ -weighted MB-*Sectoral*  $^{129}\text{Xe}$  phantom experiment with 2.4 ml of  $\text{O}_2$  added. Un-weighted image (top-left),  $T_1$ -weighted image (top-right), corresponding  $T_1$ -map (middle-left) & histogram (bottom-left), and the corresponding  $p_{AO_2}$ -map (middle-right) & histogram (bottom-right). Mean  $T_1 = 7.31 \pm 0.66$  s, FWHM  $T_1 = 1.55$  s, mean  $p_{AO_2} = 0.0321 \pm 0.004$  atm, and FWHM  $p_{AO_2} = 0.0092$  atm. .... 71

Figure 3-10: Results of the phantom experiments using MB-*Sectoral*. Plots of  $T_1$  (left) and corresponding  $p_{AO_2}$  (right) pixel average versus prepared  $\text{O}_2$  volume for four scans. The vertical error bars represent the pixel deviation in each map represented from the ROI. The horizontal error bars correspond to the precision of the prepared  $\text{O}_2$  volumes. The solid line shows the expected results. The solid line shows a significant ( $p < 0.05$ ) linear regression fit of  $p_{AO_2}$  values. Calculated  $p = 0.01$  and  $r^2 = 0.98$ . .... 72

Figure 3-11: Results of the two phantom experiments using SB-*Sectoral*. Plots of  $T_1$  (top-row) and corresponding  $p_{AO_2}$  (bottom-row) pixel average versus prepared  $\text{O}_2$  volume for five scans. The vertical error bars represent the pixel deviation in each map represented from the ROI. The horizontal error bars correspond to the precision of the prepared  $\text{O}_2$  volumes. The solid line shows a significant ( $p < 0.05$ ) linear regression fit of  $p_{AO_2}$  values. For experiment 1,  $p = 0.001$  and  $r^2 = 0.98$  and experiment 2,  $p = 0.0002$  and  $r^2 = 0.99$ . . 73

Figure 3-12: Photograph of a rat lung (left). Representative MB-*Sectoral* 2-D whole-lung projection image of a rat lung in coronal view (middle) and axial view (right) obtained at low field with  $^{129}\text{Xe}$ . FOV =  $112 \times 112$  mm<sup>2</sup>. .... 74

Figure 3-13: 2-D coronal *in vivo*  $^{129}\text{Xe}$  rat lung MRI obtained at low field with: FGRE (left), SB-*Sectoral* (middle), and MB-*Sectoral* (right). FGRE and SB-*Sectoral* used 1 breath hold and MB-*Sectoral* used 16 breath holds. .... 75

Figure 3-14: Representative rat lung ADC-maps for healthy (top-left) with corresponding histogram (bottom-left) and irradiated (top-right) with corresponding histogram (bottom-right). The mean and standard deviation of ADC values, with corresponding FWHM ADC values obtained from the Gaussian distribution of each ADC histogram, for each ADC map of all rat lungs can be found in Table 3-7..... 76

Figure 3-15: FWHM ADC values for healthy and irradiated cohorts. Results are obtained using a two-tailed (Mann Whitney) unpaired t-test. At the  $p < 0.05$  level, the differences of the population means are significantly different. The calculated  $p = 0.0317$ ..... 77

Figure 3-16: Summary of data obtained for 9 lung specimens (4 healthy, 4 irradiated, 1 healthy outlier). Each data point is a mean calculated across all imaging pixels for a given ADC map. The horizontal axis shows  $L_m$  obtained from direct histological measurements on the same lungs. Linear regression fit with 95% confidence band of the best-fit line and residual plot with significance  $p < 0.05$ . After excluding the outlier, the calculated  $p = 0.0061$  and  $r^2 = 0.7408$ ..... 78

Figure A-1: A photograph of the probe head setup with phantom for gradient waveform mapping. The plastic circular phantom contained 2.0 ml of water and 1.0 ml of Magnevist and was placed within a small surface coil wound from Litz wire..... 96

Figure A-2: Pulse sequence diagram for the MFGM acquisition to measure the gradient waveform. Small tip angle RF pulses were applied to produce a FID from the phantom. A series of points for each acquisition during phase-encoding time  $t_p$  were sampled..... 98

Figure A-3: Pre-emphasized (green) and ideal (blue) trajectories through  $k$ -space, or frequency-encoding waveform, for the  $x$ -axis (left) and  $y$ -axis (right) gradient of the 11<sup>th</sup> sector..... 98

Figure A-4: Reduced pre-emphasized (green) and ideal (blue) trajectories through  $k$ -space, or frequency-encoding waveform, for the  $x$ -axis gradient of the 11<sup>th</sup> sector..... 99

Figure A-5: Pre-emphasized (green) and ideal (blue) trajectories through  $k$ -space, or pure phase-encoding waveform, for the  $x$ -axis gradient of the 11<sup>th</sup> sector..... 99

Figure A-6: Measured gradient waveforms without (left) and with (right) coefficient correction. The prescribed input waveform (blue) was stepwise with each gradient step corresponding to 24 points (24  $\mu$ s) and measured waveform (red) experienced within the sample space. .... 100

Figure A-7: Representative input (blue) and measured (red) *Sectoral* trajectories through  $k$ -space, or frequency-encoding waveform, for the  $x$ -axis gradient of the 11<sup>th</sup> sector (left) and the  $y$ -axis gradient of the 12<sup>th</sup> sector (right). .... 101

Figure A-8: Representative ideal (blue) and measured (red) *Sectoral* trajectories through  $k$ -space, or pure phase-encoding waveform, for the  $x$ -axis gradient of the 11<sup>th</sup> sector (left) and the  $y$ -axis gradient of the 12<sup>th</sup> sector (right). .... 101

Figure B-1: H&E stained histology. Healthy lung tissue from healthy rat (left). Damaged rat lung tissue two weeks post irradiation treatment (right). This specimen shows clear thickening of the alveolar septa compared with the healthy lung, which could reasonably explain the observed correlation in calculated ADC values. However, such thickening was not seen throughout all irradiated lungs which factors into the results. .... 102

## List of Appendices

Appendix A: Gradient Waveform Mapping .....	96
Appendix B: Histological Interpretation.....	102
Appendix C: Animal Use Protocol Approval .....	103

## List of Abbreviations and Symbols

1-D, 2-D, 3-D	One, two, and three dimensional
$^3\text{He}$	Helium-3
$^{13}\text{C}$	Carbon-13
$^{60}\text{Co}$	Cobalt-60
$^{129}\text{Xe}$	Xenon-129
ADC	Apparent diffusion coefficient
BW	Receive bandwidth
COPD	Chronic obstructive pulmonary disease
CT	Computed tomography
D	Self-diffusion coefficient
Eqn.	Equation
FEV <sub>1</sub>	Forced expiratory volume in 1 second
Fig.	Figure
FID	Free induction decay
FOV	Field of view
FWHM	Full-width at half maximum
G	Maximal gradient strength
H&E	Hematoxylin and eosin
HNG	Hyperpolarized noble gases
L <sub>m</sub>	Mean linear intercept
MB- <i>Sectoral</i>	Multi breath <i>Sectoral</i>
MFGM	Magnetic field gradient monitor
MRI	Magnetic resonance imaging
NSCLC	Non-small cell lung cancer
NMR	Nuclear magnetic resonance
p <sub>A</sub> O <sub>2</sub>	Alveolar partial pressure of oxygen
PET	Positron emission tomography
PIP	Peak inspiratory pressure
ppm	Parts per million
PSI	Pounds per square inch
Rb	Rubidium
RF	Radiofrequency
RILI	Radiation induced lung injury
RP	Radiation-associated acute pneumonitis
RT	Radiation therapy
SB- <i>Sectoral</i>	Single breath <i>Sectoral</i>
SEOP	Spin exchange optical pumping
SCLC	Small cell lung cancer
SNR	Signal-to-noise ratio
SPECT	Single photon emission computed tomography
S <sub>0</sub>	Signal of normal un-weighted image
S <sub>i</sub>	Signal of weighted image
T <sub>1</sub>	Longitudinal relaxation time



$T_2$	Transverse relaxation time
TE	Echo time
$T_{\text{read}}$	Readout time
TR	Repetition time
VFA	Variable flip angle
$\Delta$	Diffusion time
$\Delta t_{\text{os}}$	Oxygen-sensitization time delay

## Chapter 1: Introduction

### 1 Introduction

This chapter provides an overview of the rationale and motivation for the thesis project. Background information of current lung measurement techniques and their advantages and limitations will be discussed. Other topics that will be covered are general NMR/MRI physics, hyperpolarization techniques, low-field considerations, and imaging pulse sequences. An overview of the imaging techniques, particularly with the *Sectoral* imaging sequence is also presented. This chapter concludes with a clear statement of the research problem, hypothesis, and objectives of the thesis.

#### 1.1 Rationale and Motivation

Respiratory diseases are a burden on health care and are often under-diagnosed. In particular, lung cancer accounts for one-quarter of all cancer related mortalities worldwide. Radiation therapy is a standard treatment, but since the lungs are a radiosensitive organ, the outcome following treatment can lead to healthy tissue damage, specifically, radiation-induced lung injury (RILI). RILI may potentially cause the radiation therapy plan to be shortened or discontinued all together, before the desired dose is administered to the cancerous tumour. Therefore, early diagnosis of RILI is critical for prevention of permanent lung damage. Current diagnostic and monitoring methods for RILI tend to focus primarily on global lung function. X-ray imaging techniques (e.g. CT imaging) currently used for examining the morphological changes associated with RILI do provide regional information, but often require the use of ionizing radiation and can only detect the late and irreversible stages. In many cases, detection is too late to make any adjustments to the radiation therapy in order to mitigate the effects. Magnetic resonance imaging (MRI) with hyperpolarized gas for pulmonary imaging shows promise for earlier measure of the RILI associated response. This thesis examines the potential application of a novel unpublished imaging sequence for low field MRI, coupled with hyperpolarized  $^{129}\text{Xe}$  gas, as an imaging tool for probing the lungs damaged by irradiation.

## 1.2 Pulmonary Physiology

### 1.2.1 Healthy Lungs

The lungs are a complex organ located in the chest and are part of the respiratory system (1). The role of the lungs is ventilation/perfusion and gas exchange for oxygen intake and carbon dioxide removal. A schematic diagram of the branching structure of the lungs is shown in **Figure 1-1**. The lungs start with a tube-shaped airway called the trachea and branches into two narrower airways that continue to branch multiple times into bronchioles. At the end of the bronchioles there are small sacs called alveoli that are the sites of gas exchange. Oxygen that is inhaled diffuses from the alveoli into the capillaries. Carbon dioxide diffuses from capillaries into the alveoli to be exhaled. The lungs have developed important and sensitive structures and physiological relationships for efficient air passage and gas exchange.

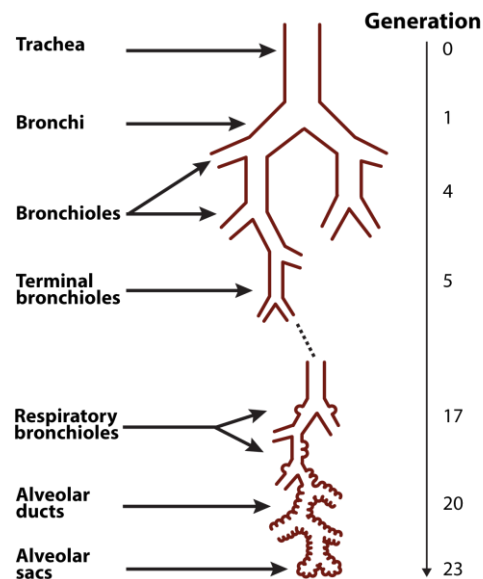


**Figure 1-1:** Schematic of airway branching in the lung, adapted from (1).

### 1.2.2 Lung Cancer and Radiation Therapy

Lung cancer is a major health burden that accounts for one-quarter of all cancer-related mortalities in Canada (2) and the United States (3), making it the leading cause of cancer related deaths. The Canadian Cancer Society has estimated that 20,000 deaths and 25,500 new cases were caused by lung cancer in 2013 (2). In the United States, an estimated

159,000 deaths and 224,000 new cases are anticipated in 2014 (3). Lung cancer is divided into two major classes: small cell lung cancer (SCLC) and non-small cell lung cancer (NSCLC). NSCLC accounts for approximately 85% to 90% of all diagnosed lung cancer cases, with the remainder being SCLC (4,5). Radiation therapy (RT) is an essential therapeutic modality that is a standard treatment for patients with both NSCLC and SCLC. RT works by delivering brief individual doses of ionizing radiation in the form of high energy x-rays (or photons) to the affected cancerous area while minimizing damage to the healthy tissue. This is best achieved by conforming, or shaping, the RT beams while delivering the radiation from different directions to match the shape of the target tumour. Successful treatment with RT depends on numerous factors, including, ability to localize dose, total absorbed radiation dosage, dosage size and rate, fractionation, beam alignment, and use of chemotherapy (6). Furthermore, patient-related factors affect outcome, including pre-existing disease, poor lung function, and genetic predispositions. However, the main limitation of RT is the added toxicity to the surrounding healthy lung tissue, compromising the effectiveness of the RT plan.

### 1.2.3 Radiation-induced Lung Injury (RILI)

The lung is relatively sensitive to ionizing radiation (7,8) yet, it is often inadvertently irradiated as part of RT programs to treat tumours of the lung, esophagus, and breast. Consequently, several potential sources of error in RT can lead to further damage of healthy lung tissue. Respiratory motion and setup errors during RT can cause uncertainties in tumour position, dosage calculations, and delivery (9). Even with conformal radiation therapy, instances of lung injury of varying degree are still reported (10,11). This is because RT applied conformally is an imperfect process, where miscalculations and variations in lung tumour volume and location can lead to dosimetric consequences.

The degree of normal tissue damage is described by two distinct toxic endpoints and is collectively referred to as Radiation-induced Lung Injury (RILI). These toxic endpoints exist in the form of: (i) radiation-associated acute pneumonitis (RP) and (ii) pulmonary fibrosis. Both acute pneumonitis and pulmonary fibrosis are common outcomes of RT

and may affect physiological function of the lung, including efficient gas exchange, perfusion and ventilation or airflow (6). These side effects can also greatly reduce the quality of the patient's life. The severity of RILI is influenced by multiple factors including the genetic predispositions, existing lung diseases, weakened pulmonary function, and age of the individual.

Acute RP is the initial complication of RILI and develops between 1 to 3 months after RT (6). Symptoms include inflammation, shortened breath, dry cough, and fever. Incidence of RP is higher with greater dose and volume. The majority of patients with acute RP will develop progressive pulmonary fibrosis. Pulmonary fibrosis is the secondary complication of RILI and may develop between 6 to 24 months after exposure (12). Symptoms include dyspnea and scarring that reduces lung function. Pulmonary fibrosis is irreversible and may lead to death.

The occurrence of RILI often limits the radiation dose in RT that is needed to effectively destroy tumour cells. Timely detection of early acute pneumonitis in individuals at risk provides an opportunity to modify the treatment strategy before acute pneumonitis and irreversible fibrosis occur. RILI is estimated to occur in 5-35% of patients undergoing thoracic RT. Diagnosis of pneumonitis was challenging to determine in 28% of screened patients suspected of having pneumonitis after RT (13). Uncertainties related to other medical conditions include cardiac disease, infection, and emphysema. Since the RT plan is delivered conformally, the assessment of RILI response using medical imaging methods may lead to more individualized therapy and could prevent, interrupt, or delay the progression of RILI. Several medical imaging methods are currently used to predict and detect RILI. However, imaging studies to assess early response are lacking.

#### 1.2.4 Animal Models of RILI

Lung injury is a clinical concern and therefore rodent models are important for providing information on lung disease progression. Before being translated into standard clinical practice, success of techniques must be demonstrated in animal models for safety and efficacy. Rodent and human lungs are different but have similar effects of radiation, such as pneumonitis. Furthermore, a rodent model is beneficial due to the ability to control the

variables. Many patients have additional lung problems, like chronic obstructive pulmonary disease (COPD), which makes the rodent model an attractive choice for biomedical research (14,15).

The response of RILI follows a well-characterized progression (16): (i) latent period or delay to the injury, (ii) acute phase of pneumonitis, (iii) final late stage of pulmonary fibrosis. This sequence of events is seen in mammals allowing for use of small animal models such as laboratory rats to study the response of RILI. For this thesis, rat models are used since they have been widely used in other experiments and preclinical studies.

### 1.3 Diagnostic Measurements of RILI

The extent of RILI can be measured and quantified using various medical imaging techniques and pulmonary function tests. It is helpful to have suitable and accurate methods for measuring early lung-level injury to aid in identifying individuals that could benefit from pharmacological medication and are critical in optimizing any current or future diagnostic or therapeutic regimes. Quality-of-life is expected to be substantially increased if RILI is detected in the early stage. Therefore, the goal is to detect RILI early in order to mitigate and treat lung tissue.

#### 1.3.1 Pulmonary Function Tests

Pulmonary function tests measure global lung function and are used clinically to measure multiple lung parameters, including lung volumes, rates of air flow, and gas ventilation performance. The standard clinical mode of evaluation for pulmonary function is spirometry, a breathing test that measures the volume and rate of inhalation/exhalation of air out of the lungs (17). Spirometry is a cost-effective and non-invasive technique, requiring subject cooperation. The patient breathes into a spirometer to inhale maximally followed by completely exhaling in the shortest capable amount of time. The most common spirometric measure is the forced expiratory volume in one second ( $FEV_1$ ). Change in  $FEV_1$  may be consistent with changes in restrictive processes associated with pulmonary fibrosis. Spirometry is limited in that it is difficult to perform in animals. In patients, it depends on patient effort and may be a poor indicator in elderly and pediatric

populations. Furthermore, it provides global functional information about the lung but doesn't provide any regional information to accurately describe disease heterogeneity (18). Patients with COPD commonly manifest comorbidities which may influence the FEV<sub>1</sub> measures (19,20). Therefore, spirometry may be insensitive to early disease and gradual progression.

### 1.3.2 Chest Radiography/Computed Tomography

Chest radiography and computed tomography (CT) are standard x-ray imaging techniques used for screening and assessing RILI. Chest radiographs are able to detect RILI associated changes 2 to 3 months following RT (6). CT is more sensitive in detecting RILI than chest radiographs, allowing for earlier detection (21). CT uses the absorption by biological tissue of x-rays from multiple projections to produce two-dimensional (2-D) images of anatomical structure. The tissue is imaged using an external x-ray source. Since the lungs are a radiosensitive organ (22) the accumulated dose limits the frequency of application of these techniques. CT often only detects the late irreversible stage of pulmonary fibrosis. The limitation of CT screening is the high frequency of false positive findings, leading to high costs, further diagnostics, and patient anxiety. Radiation-associated lung injury has also been detected and assessed using micro-CT in mice (23).

### 1.3.3 Nuclear Medicine Methods/PET/SPECT

Functional imaging within the lung using single-photon emission computer tomography (SPECT) measurements and positron emission tomography (PET) provide quantitative functional information including ventilation and perfusion of the lung. In PET, positron-emitting radioisotopes are used as tracer agents. PET is based on the detection of two collinear 511-keV  $\gamma$ -rays resulting from the annihilation of a positron and its antiparticle, an electron. In SPECT, radioisotopes are inhaled or injected into the venous system and are transported into the small lung capillaries of the lung. SPECT utilizes long-lived emitting isotopes with lower energy  $\gamma$ -emitting isotopes, whereas PET uses short-lived positron emitting isotopes. Regional pulmonary blood flow is proportional to the concentration of the radioisotopes. Perfusion and ventilation mapping is possible with

SPECT (24). SPECT has been used to measure gas exchange of regional and whole lung and shows potential for elucidating mechanisms responsible for distributions of regional ventilation and perfusion. Both SPECT and PET are limited by spatial resolution and delivery of additional radiation dose.

### 1.3.4 Magnetic Resonance Imaging

Magnetic resonance imaging (MRI) is an advantageous technique due to its lack of ionizing radiation dose, excellent soft tissue contrast, and multi-planar imaging capabilities. The first 2-D images using nuclear magnetic resonance (NMR) were generated in 1973 by Lauterbur using a series of 1-D projections (25). Today, MRI is widely used to non-invasively obtain high-resolution images of internal body anatomy and certain aspects of body function with excellent soft-tissue contrast. However, conventional proton MRI presents a challenge for pulmonary imaging. The lungs are mostly gas space with very little proton density. This low tissue density, coupled with the effects of varying local magnetic fields which cause a short signal lifetime in the complicated geometry of the lung, lead to a very low MRI signal. Moreover, lung MRI signal can be further degraded by image artifacts arising from respiratory motion (26).

### 1.3.5 Hyperpolarized MRI of RILI

Hyperpolarization is a pre-magnetized form of MRI with up to five orders of magnitude higher signal than that achievable by conventional means. Hyperpolarized noble gases (HNG) can be used as contrast agents for lung MRI. In 1994, Albert *et al.* reported the first hyperpolarized lung images of a mouse using  $^{129}\text{Xe}$  (27). HNG imaging of the lungs is a non-invasive approach with no associated x-ray dose, making it well suited for both rodent and human lung imaging. Initial studies have focused on ventilation and diffusion-weighted imaging. Both hyperpolarized helium-3 ( $^3\text{He}$ ) and xenon-129 ( $^{129}\text{Xe}$ ) gases are safe for human inhalation and are commonly used for HNG pulmonary MRI. In HNG MRI, the gas nuclei give rise to the MRI signal and reveal ventilated regions in the lungs. The non-ventilated areas show no MRI signal. Previous studies have shown human lungs with ventilation changes before and after RT using  $^3\text{He}$  (28–30). Regional measurements with  $^3\text{He}$  MRI have shown structural and functional lung irregularities to evaluate RILI



(31). Recently, Fox *et al.* have used  $^{129}\text{Xe}$  in a rat model to show gas exchange abnormalities in the early phase of RILI two weeks post-irradiation, which correlate with mean linear intercept ( $L_m$ ) obtained from histology (32).  $L_m$  is a measure of surface area to volume ratio and a commonly reported metric for quantifying of lung damage. In addition to hyperpolarized gases, metabolic magnetic resonance spectroscopy and MRI of RILI with hyperpolarized carbon-13 ( $^{13}\text{C}$ ) have been demonstrated (33) and early changes were attributed to RP (34).

## 1.4 Physics of Nuclear Magnetic Resonance (NMR)

### 1.4.1 Nuclear Spin and Magnetic Moments

Nucleons (i.e. neutrons and protons) of an atom possess nuclear spin, a quantum mechanical property represented by a spin quantum number,  $\vec{I}$ . If the neutrons and protons are both paired, the overall spin of the nucleus is zero ( $\vec{I} = 0$ ), and no NMR signal arises. However, unpaired neutrons and/or protons can lead to a nucleus with spin  $\vec{I} = \frac{1}{2}$ , providing an NMR/MRI signal. Since, most NMR/MRI applications involve  $\vec{I} = \frac{1}{2}$ , only such spin systems are considered here. A particle characterized by a spin  $\vec{I} = \frac{1}{2}$  also comprises of an inherent angular momentum,  $\vec{J}$ , related by:

$$\vec{J} = \hbar \vec{I}, \quad [1.1]$$

where  $\hbar$  represents the quantization of angular momentum and is called the Planck's constant. The non-zero nuclear spin gives rise to a magnetic moment,  $\vec{\mu}$ , along the spin axis, which is proportional to the total intrinsic angular momentum:

$$\vec{\mu} = \gamma \vec{J}. \quad [1.2]$$

The nuclei specific proportionality constant,  $\gamma$ , is called the gyromagnetic ratio and can be expressed in units of megahertz per tesla (MHz/T) by  $\gamma = \frac{\gamma}{2\pi}$  (e.g.  $\gamma = 42.58$  MHz/T for  $^1\text{H}$ , 32.43 MHz/T for  $^3\text{He}$  and 11.78 MHz/T for  $^{129}\text{Xe}$ ).

When placed within a static external magnetic field ( $\vec{B}_0 = B_0 \hat{z}$ ), the magnetic moment will experience a torque,  $\vec{N}$ , described by:

$$\vec{N} = \vec{\mu} \times \vec{B}_0. \quad [1.3]$$

The magnetic field is assumed to be applied along the  $z$ -axis and subscripted with a '0'. The torque causes the magnetic moment to precess around the direction of the field at a frequency proportional to the external magnetic field acting on it, expressed by the Larmor frequency,  $\vec{\omega}$ :

$$\vec{\omega} = \gamma \vec{B}_0. \quad [1.4]$$

The magnetic moment is at an angle to the field, tracing out a circle around the direction of the field in whichever orientation it is in.

#### 1.4.2 Quantum Mechanical Description of NMR

Quantum mechanically, the magnetic moments with a net spin of  $\frac{1}{2}$  will have two possible quantum energy spin states, a low energy state or spin-up ( $m_{\uparrow}$ ) and a high energy state or spin-down ( $m_{\downarrow}$ ). In the absence of an external magnetic field, the quantum spin states are degenerate. However, in the presence of an external magnetic field, the interaction causes the energy of the nuclear magnetic moment to split into the two energy states, as shown in **Figure 1-2**.

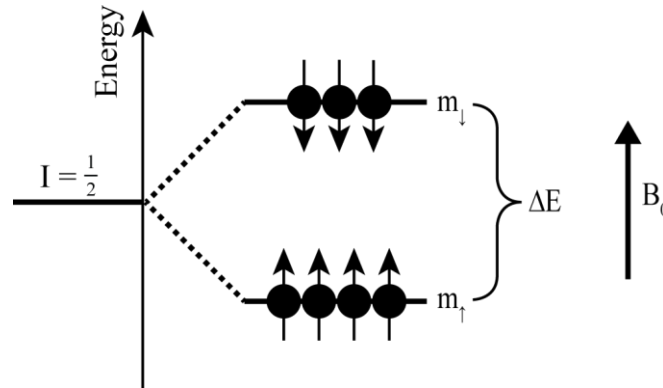


**Figure 1-2:** Splitting of spin states for a spin  $\frac{1}{2}$  system in an external magnetic field  $\vec{B}_0$ .

These energy states are called Zeeman levels and the splitting of the energy levels is called the Zeeman Effect. The energy of a magnetic moment for nuclei with spin  $\frac{1}{2}$ , in a magnetic field  $\vec{B}_0$  is given by:

$$E = \pm \frac{1}{2} \gamma \hbar B_0. \quad [1.5]$$

A transition between the Zeeman levels represents a change in energy:

$$\Delta E = \gamma \hbar B_0. \quad [1.6]$$

### 1.4.3 Polarization and Bulk Magnetization

The difference in energy between the Zeeman levels is directly proportional to the strength of the external magnetic field and inversely proportional to the temperature. Both Zeeman levels are stable energy states. The orientation of the spin state will depend on its internal energy, in order to occupy the lowest energy state. For a collection of magnetic moments, there is a statistical distribution between the two states given by the Boltzmann distribution. The ratio of spins in the two states depends on the Boltzmann factor according to:

$$\frac{m_{\downarrow}}{m_{\uparrow}} = \exp\left(-\frac{\Delta E}{k_B T}\right), \quad [1.7]$$

where  $k_B$  is the Boltzmann constant and  $T$  is the absolute temperature.

The lower-energy state is slightly favored, so that there are more nuclei in the spin-up state than the spin-down state. Nuclei can move between the two states simply by gaining or losing electromagnetic radiation (EM) in the form of photons. The frequency of EM radiation required to cause transition between the two energy levels of spin is the Larmor frequency and can be calculated using **Eqn. [1.4]**.

The fractional excess of spins in the lower energy state defines the polarization,  $P$ :

$$P = \frac{m_{\uparrow} - m_{\downarrow}}{m_{\uparrow} + m_{\downarrow}}. \quad [1.8]$$

The thermal equilibrium polarization follows the Boltzmann distribution (**Eqn. [1.7]**) and can be re-written as:

$$P = \frac{1 - \exp\left(\frac{-\gamma\hbar B_0}{k_B T}\right)}{1 + \exp\left(\frac{-\gamma\hbar B_0}{k_B T}\right)}. \quad [1.9]$$

Instead of describing individual magnetic moments, it is easier to represent their average ensemble, precessing at the Larmor frequency, as a single vector sum (**Figure 1-3**). This vector sum is called the bulk magnetization,  $\vec{M}$ , and is defined as the volume density of magnetic moments:

$$\vec{M} = \sum_{i=1}^N \vec{\mu}_i = \rho_0 \bar{\mu} P, \quad [1.10]$$

where  $\rho_0$  is the density of the magnetic moments. In the high temperature approximation ( $kT \gg \mu B$ ), the equilibrium magnetization ( $M_0$ ) can be approximated as:

$$M_0 = \frac{\rho_0 \gamma^2 \hbar^2}{4k_B T} B_0. \quad [1.11]$$

Treating the behavior of the magnetic moments in terms of magnetization allows us to drop the quantum mechanical description and use classical mechanics onwards. The advantage of using a classical description allows for simpler description of the NMR and MRI experiments.

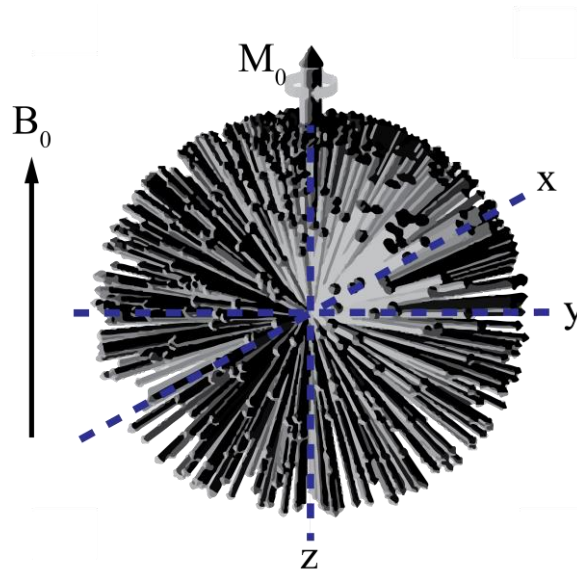


**Figure 1-3:** A Boltzmann distribution of individual magnetic moments in a macroscopic sample can be expressed as a single net magnetization vector along the  $z$ -axis (adapted from (35)).

#### 1.4.4 Dynamics of Magnetization in the Presence of a Time-Varying Applied Magnetic Field

The net magnetization,  $M_0$ , resulting from a static field  $B_0$ , itself cannot be measured at equilibrium (i.e. parallel with  $B_0$  in the  $z$ -direction). The equilibrium state of the nuclei must first be perturbed to excite the orientation of  $\vec{M}_0$ , allowing its precession to be detectable. Initially, there is no magnetization in the transverse plane perpendicular to  $\vec{B}_0$ . The  $\vec{B}_0$  field is always on, hence it is often referred to as the static external magnetic field. Instead,  $\vec{M}_0$  must be tipped from the  $z$ -plane into the  $x$ - $y$  plane (**Figure 1-4**). If a time-varying magnetic field,  $\vec{B}_1$ , is applied at the radiofrequency (RF) with a matching Larmor frequency (i.e. resonance), the magnetization vector,  $\vec{M}_0$ , can be perturbed, by tipping it towards the  $x$ - $y$  plane (**Figure 1-4**). This is achieved by turning on a secondary

time dependent (i.e. oscillating) magnetic field  $\vec{B}_1$  briefly as an excitation RF pulse that oscillates at the Larmor frequency perpendicular to  $\vec{B}_0$ . The time-varying field,  $\vec{B}_1$ , is generally circularly polarized and appears as a stationary transverse field in the rotating frame. Therefore,  $\vec{B}_1$  can tip (or nutate) the net magnetization from the longitudinal axis to the transverse plane by a certain flip angle (**Eqn. [1.12]**). The flip angle generated by an RF pulse is given by:

$$\alpha = \gamma \int_0^{\tau_p} |\mathcal{B}_1(t)| \cdot dt, \quad [1.12]$$

where  $\alpha$  is the tip angle,  $\tau_p$  is the pulse duration, and  $\vec{B}_1$  the RF pulse field strength. For  $\alpha = \pi/2$ , this RF excitation pulse tips the  $M_z$  vector entirely into the transverse plane, and is referred to as a  $90^\circ$  pulse. Another important effect on the spins is phase coherence. The RF pulse brings all of the spins into coherence, meaning they will point in the same direction at the end of the RF pulse. Once in the transverse plane,  $M_{xy}$  induces a voltage in a receiver coil which is sensitive only to the magnetization perpendicular to  $\vec{B}_0$ . After the RF pulse is removed, the coil detects the oscillating magnetic field from the nuclear spins and induces a voltage varying at the Larmor frequency which decays in time as the nuclei then rapidly dephase with respect to each other (transverse relaxation,  $T_2$ ) and return to equilibrium with the static field (longitudinal relaxation,  $T_1$ ), called a free induction decay (FID). These relaxation processes will be discussed in detail next.

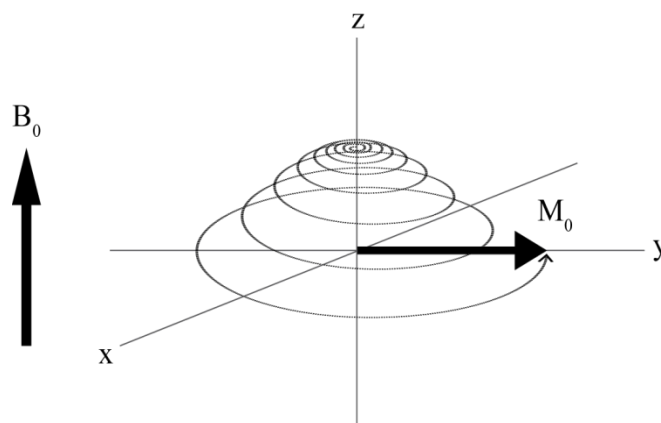


**Figure 1-4:** The motion of the magnetization as observed in the laboratory frame of reference in response to an excitation pulse of  $90^\circ$ .

### 1.4.5 Spin Relaxation Mechanisms

A  $\vec{B}_1$  field applied along the  $x$ -direction with an excitation RF pulse of flip angle  $90^\circ$  (or  $\pi/2$ ) will cause the magnetization vector to nutate into the transverse axis, aligning it in the  $y$ -direction. Immediately after the application of the RF pulse, the net magnetization will begin to relax towards equilibrium by two separate relaxation mechanisms. First, the decay of  $M_{xy}$ , due to spin dephasing following phase coherence after the RF pulse, referred to as spin-spin or transverse relaxation. Second, the regrowth of  $M_z$ , due to realigning spins with the static magnetic field due to energy loss to the lattice, referred to as spin-lattice or longitudinal  $T_1$  relaxation. As will be described later, for hyperpolarized gas the  $T_1$  appears as a decay as the spins return to their thermal equilibrium state of  $^{129}\text{Xe}$  ( $\sim 0$ ). It is important to note that both mechanisms occur simultaneously.

#### 1.4.5.1 Longitudinal $T_1$ Relaxation

An exponential recovery of magnetization longitudinal to  $\vec{B}_0$  occurs due to an energy exchange between spins and the surrounding lattice. A loss of spin system energy occurs as the spins return to their thermal equilibrium with the lattice. As spins re-establish their thermal equilibrium state, they decrease from a high to low energy state, releasing RF energy back into the surrounding environment. This spin-lattice relaxation follows an exponential curve and is characterized by a tissue-specific exponential time decay constant, known as the longitudinal relaxation time or  $T_1$ .  $T_1$  is the length of time for the

longitudinal magnetization to relax back to 63% of the initial longitudinal magnetization. The time dependence of the longitudinal magnetization vector  $M_z$  during  $T_1$  relaxation is described by:

$$M_z(t) = M_z(0)e^{-t/T_1} + M_0(1 - e^{-t/T_1}), \quad [1.13]$$

where  $M_z(0)$  is the initial longitudinal magnetization at time zero. If the RF flip angle is zero (i.e.  $\alpha = 0$ ) then  $M_z(0) = 1$ , and if  $\alpha = 90^\circ$  then  $M_z(0) = 0$ . The return of magnetization to thermal equilibrium is described by the second term in **Eqn. [1.13]**. The process to fully restore  $\vec{M}_0$  along the  $z$ -axis typically occurs within several seconds. The  $T_1$  relaxation is greatly affected by fluctuating local magnetic fields in the lattice. Hence, direct dipolar interactions with other magnetic moments in the lattice, as well as paramagnetic molecules such as molecular oxygen, also greatly contribute to  $T_1$  relaxation.

#### 1.4.5.2 Transverse $T_2$ Relaxation

A gradual exponential decay of magnetization transverse to  $\vec{B}_0$  occurs due to an energy exchange between spins. No energy is lost from the spin system, but a decay (or dephasing) mechanism of transverse magnetization  $M_{xy}$  occurs that is caused by a loss of phase coherence. Dephasing arises because a small frequency exists between magnetic moments of neighbouring nuclei due to differences in local magnetic field. Local magnetic field inhomogeneities that are both internal to the nuclear system (intrinsic) as well as external to  $\vec{B}_0$  (extrinsic) contribute to spin-spin relaxation. This spin-spin relaxation is characterized by an intrinsic time constant, known as the transverse relaxation time or  $T_2$ .  $T_2$  is the length of time for the transverse magnetization to decay to 37% of the initial transverse magnetization. The transverse magnetization vector  $M_{xy}$  during transverse relaxation is described by:

$$M_{xy}(t) = M_0(e^{-t/T_2}), \quad [1.14]$$



where  $\vec{M}_0$  is the equilibrium magnetization. The dephasing of nuclei through an inhomogeneous magnetic field adds an irreversible component, adding to the rate of relaxation. If a sample is placed inside an inhomogeneous external magnetic field, the spins will precess at different frequencies relative to the variations in  $\vec{B}_0$ . This extrinsic dephasing due to magnetic field inhomogeneities is characterized by the time constant  $T_2'$ . The apparent transverse relaxation time  $T_2^*$  takes both intrinsic and extrinsic mechanisms into account and can be described by:

$$\frac{1}{T_2^*} = \frac{1}{T_2} + \frac{1}{T_2'} . \quad [1.15]$$

$T_2^*$  is shorter than  $T_2$  because there is additional dephasing components of the transverse magnetization caused by the magnetic field inhomogeneities characterized by  $T_2'$ .  $T_2^*$  decay is a rapid process that causes  $M_{xy}$  to decay from maximum to zero in a matter of a few milliseconds.

#### 1.4.6 MRI Signal Detection and Measurement

The detection of the MRI signal relies on Faraday's law of electromagnetic induction. An inductive pickup (receiver) coil, placed perpendicular to the transverse plane, is used to detect an induced voltage caused by the temporal evolution of the sample's transverse magnetization  $M_{xy}$ . The receiver coil must be tuned to the resonance frequency of the nuclei of interest to allow for proper coupling to the magnetization. The voltage induced by the oscillating magnetic field varies at the Larmor frequency and can be expressed as:

$$V(t) = -\frac{d}{dt} \int_{V_s}^0 (B_1(\vec{r}))_{xy} \cdot (M_{xy}(\vec{r}, t)) dV . \quad [1.16]$$

The calculated integral is over the entire volume of the sample,  $V_s$ . All of the information about the species present, including the Larmor frequency as a function of time, is contained in the received voltage. The magnitude, frequency and phase of the voltage is proportional to the spin density, spin relaxation, and spin precession. Thus, this induced voltage in the coil becomes the received signal,  $S(t)$ , expressed as:

$$S(t) = M_0(1 - e^{-TR/T_1})(e^{-TE/T_2^*}). \quad [1.17]$$

The typical NMR experiment acquires signal from the entire volume of the sample. This detected signal is referred to as the free induction decay (FID) and is detected immediately after an RF pulse is applied without using any spatial encoding gradients. The FID follows an exponential decay because it is modulated by transverse relaxation mechanisms ( $T_2^*$  above) as it returns to its equilibrium state. The amount of nuclei that contributes to  $M_0$  is proportional to the strength of the detected signal and the magnitude of the signal is proportional to the density of the sample. The FID is often routinely used to experimentally optimize the MRI system in pre-scan steps to locate the resonance frequency peak, calibrate the RF power and shim the static magnetic field.

## 1.5 Hyperpolarized Gas Production

In conventional proton MRI, the signal that is detected at thermal equilibrium levels represents approximately 1 ppm of the available nuclei. However, it is possible to prepare some noble gases in a pre-magnetized form, referred to as *hyperpolarized*. Hyperpolarized noble gases (HNG) are prepared using a spin exchange optical pumping process (36) and can be directly used for lung imaging. The magnetization achieved in this form of MRI is up to five orders of magnitude higher than that achievable by conventional means. HNG imaging permits direct visualization of these gases reflecting lung anatomy. This non-invasive technique can also be used to measure lung function without the need for ionizing radiation. Both hyperpolarized helium-3 ( $^3\text{He}$ ) and xenon-129 ( $^{129}\text{Xe}$ ) can be hyperpolarized; however,  $^{129}\text{Xe}$  is expected to be the gas that will be the most clinically useful as  $^3\text{He}$  is rare and expensive. By using  $^{129}\text{Xe}$  for lung MRI, spatially localized information can be obtained, showing anatomical structure and function. The anatomical information obtained is typically in the form of static ventilation maps and apparent diffusion coefficients (ADC), and are useful for quantifying RILI. The functional information is in the form of regional alveolar partial pressure of oxygen ( $p_{\text{A}}\text{O}_2$ ) and is obtained by measuring  $T_1$  relaxation of  $^{129}\text{Xe}$  in the lungs.  $^{129}\text{Xe}$  ventilation MRI shows promise for differentiating healthy lungs from those with pathologies. Investigating ventilation dynamics provides more information into lung

pathophysiology. Since the polarization is independent of the magnetic field strength, low field strengths can be exploited to reduce costs without sacrificing image quality and will be discussed in detail in **section 1.6**.

### 1.5.1 Properties of $^3\text{He}$ and $^{129}\text{Xe}$

Both  $^3\text{He}$  and  $^{129}\text{Xe}$  have non-zero nuclear spin of  $\frac{1}{2}$  and are suitable for imaging. Their nuclei density is lower compared to proton but their much higher nuclear polarization, due to hyperpolarization, can more than offset this. This leads to a large magnetization magnitude and thus a high achievable MRI signal. Both gases are stable and chemically inert, making them safe for human inhalation. The orbital electron shells in  $^3\text{He}$  and  $^{129}\text{Xe}$  are filled thus minimizing electric and magnetic field gradients at the nucleus and reducing interactions with other atoms and molecules, leading to longer  $T_1$ .

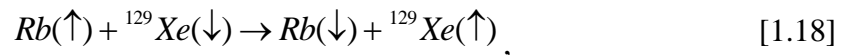
$^3\text{He}$  is an attractive noble gas for lung imaging with a larger magnetic moment and longer longitudinal relaxation times compared to  $^{129}\text{Xe}$  (37). Compared to  $^{129}\text{Xe}$ , a greater signal-to-noise ratio (SNR) is achievable with  $^3\text{He}$  because the gyromagnetic ratio is about 2.75 times larger and high levels of attainable polarization are achievable (38).  $^3\text{He}$  is the rarely occurring form of inert helium gas ( $^4\text{He}$ ). The exceedingly rare  $^3\text{He}$  is obtained as a by-product of nuclear weapon manufacturing from tritium decay. Furthermore, the required time to polarize  $^3\text{He}$  is lengthy (10-20 hours) for useful volumes. The solubility of  $^3\text{He}$  is negligible in the blood and is therefore restricted to morphological studies of the airways, bronchi, and alveolar structures (39).

$^{129}\text{Xe}$  is an attractive noble gas for lung imaging due to its much greater natural abundance compared to  $^3\text{He}$ .  $^{129}\text{Xe}$  is a plentiful by-product of the liquid air industry that accounts for 26% of all naturally occurring xenon.  $^{129}\text{Xe}$  is highly lipophilic making it soluble in blood and tissues (40). This high affinity for lipids and other body tissues (e.g. blood) permits imaging of tissues distant from the lung, providing additional information about blood vasculature, alveolar surface area, or septal thickness (27). In high concentrations,  $^{129}\text{Xe}$  can have an anesthetic effect.

Future  $^3\text{He}$  supplies are unpredictable and therefore widespread clinical use with it has been limited. Since the leading alternative is  $^{129}\text{Xe}$ , having a high abundance and lower cost, the work in this thesis will focus on applications with  $^{129}\text{Xe}$ , though it is equally applicable to  $^3\text{He}$ .

### 1.5.2 Spin Exchange Optical Pumping of $^{129}\text{Xe}$

The hyperpolarization of  $^{129}\text{Xe}$  is prepared by spin exchange using an optically pumped alkali metal vapour pumped with a diode laser (41). Spin exchange optical pumping (SEOP) is a multi-step procedure that combines optical pumping of Rubidium (Rb) atoms and spin exchange between the Rb and  $^{129}\text{Xe}$  nuclei (42). First, Rb vapours combine with a gas mixture of  $^{129}\text{Xe}$ ,  $^4\text{He}$ , and  $\text{N}_2$  inside an optical pumping cell within the presence of a magnetic field. The Rb vapour is optically excited via circularly polarized light tuned to the transition wavelength of 795 nm. As the gas mixture flows constantly through the optical pumping cell, Rb undergoes electronic polarization and serves as a spin transferring medium. Nitrogen acts as quenching gas, by suppressing the re-radiation of photons, to reduce depolarization of the electron spins. Helium is added for pressure broadening of the Rb spectral lines so that Rb matches the laser absorption linewidth. Second, the polarization from valence electrons of Rb transfer to unpolarized  $^{129}\text{Xe}$  nuclei through collisions between  $^{129}\text{Xe}$  and Rb atoms. The entire process undergoes a Fermi interaction:



where  $\uparrow$  represents the spin up state or  $+1/2$  and  $\downarrow$  represents to spin-down state or  $-1/2$ . The final result is a hyperpolarization of  $^{129}\text{Xe}$  (41). The achievable polarization depends on the efficiency of the hyperpolarization process. In practice, typical levels of polarization obtainable are 5-25% over a wide range of conditions including laser power, gas mixture, temperature, field strength, and pressure. After the mixture exits the cell, the gas is cooled to liquid nitrogen temperatures ( $-196\text{ }^\circ\text{C}$ ) and  $^{129}\text{Xe}$  is stored by solidification. It exhibits a long relaxation time in the solid state while a small permanent magnet is used to maintain the polarization. In this form, the  $T_1$  of  $^{129}\text{Xe}$  is about 3 hours.

The  $^{129}\text{Xe}$  is then quickly thawed and dispensed into a special non-permeable Tedlar® bag for delivery.

### 1.5.3 Practical Considerations with Hyperpolarized $^{129}\text{Xe}$

The most distinguishing feature of hyperpolarized  $^{129}\text{Xe}$  is its non-equilibrium spin polarization. Consequently, the longitudinal magnetization available during imaging is non-renewable. Therefore, the application of excitation RF pulses for imaging will progressively and irreversibly diminish the available magnetization which is not recoverable without further optical pumping. During imaging, the magnetization is continuously depleted and thus needs to be managed wisely. Special care must also be taken to minimize external contributions to  $T_1$  relaxation. In hyperpolarized  $^{129}\text{Xe}$  MRI the  $T_1$  relaxation determines the decay of longitudinal magnetization towards thermal equilibrium. Oxygen is paramagnetic and can thus alter the local fields of  $^{129}\text{Xe}$  when collisions of both gases occur, consequently further reducing its  $T_1$  relaxation time. The paramagnetic effect of oxygen causes a gradual depolarization of  $^{129}\text{Xe}$  and the rate of depolarization depends on the partial pressure of oxygen. This rapid decay of  $T_1$  plays an important role in efficient experimental planning. It is therefore ideal to have the polarizer system responsible for gas preparation on site, oxygen-free and easily accessible.

## 1.6 Hyperpolarized $^{129}\text{Xe}$ Imaging at Low Magnetic Field

This section contains select background information that is important for understanding hyperpolarized  $^{129}\text{Xe}$  MRI, particularly at low magnetic field strengths.

### 1.6.1 Low Field Considerations for $^{129}\text{Xe}$ MRI

Numerous compelling motives exist for imaging with  $^{129}\text{Xe}$  at low magnetic fields ( $< 0.1$  T) including field-independent polarization (43), improved scanner designs (44), lower running costs (i.e. installation, hardware, shielding, etc...) (45), reduced susceptibility (46) and specific absorption rate (SAR) (47). Conventionally, in proton MRI, a higher magnetic field strength ( $\sim 1$  T) leads to greater signal. Although  $^1\text{H}$  atomic densities in tissue are large, they have weak nuclear polarization at thermal (Boltzmann) equilibrium.

The thermal MRI signal obtained is proportional to the square of the field strength and SNR varies linearly with the field strength. A special feature of imaging with hyperpolarized  $^{129}\text{Xe}$  is that the available magnetization is independent of magnetic field strength (43). The optimum field strength for clinical imaging with hyperpolarized  $^{129}\text{Xe}$  has been predicted to be around 0.1-0.6 T (46,48). This is because the major contributing factor is the frequency of the noise when it goes from the coil-dominated regime to the sample-dominated regime above 0.1 T. Therefore, there exists no benefit in terms of SNR for imaging with hyperpolarized  $^{129}\text{Xe}$  in the coil-dominated noise regime at higher field strengths (49). This reduces the need for heavy and expensive superconducting magnets found in conventional MRI systems. Low field strength also allows for a variety of feasible field strengths with the potential for open magnet designs, allowing flexible scanner geometries (i.e. permitting upright imaging).

However, most  $^{129}\text{Xe}$  studies to date employ high field MRI scanners designed for proton because  $^1\text{H}$  imaging can be easily employed for anatomical localization or shimming and it is convenient for researchers to simply adopt existing technology. Imaging at high fields is made additionally challenging due to susceptibility-induced effects at the air-tissue boundaries. Slightly different magnetic fields exist at these sharp boundaries that create micro-gradients which cause more rapid dephasing of the nuclei. Thus a  $T_2^*$  reduction occurs at high fields resulting in images with degraded SNR and susceptibility artifacts. These underlying motivations support the idea that imaging at low field is a viable alternative for imaging with  $^{129}\text{Xe}$  and may be preferred.

### 1.6.2 Spatial Frequency and Phase-encoding

The excitation RF pulse applied to the entire sample volume will generate an MRI signal containing a single resonance frequency. Before an image can be formed, the different regions of the sample must be distinguished from each other. The signal that is received goes through spatial encoding using some combination of additional magnetic field gradients ( $G_x$ ,  $G_y$ , or  $G_z$ ) to obtain 2-D or 3-D images. By intentionally adding or subtracting a weaker magnetic field in the direction as  $\vec{B}_0$  but varying spatially, a sample will experience different field strengths at different locations causing the nuclei to

resonate at different frequencies. Frequency and phase measurements are used to distinguish the MRI signals at the different positions in 2-D. The instantaneous frequency at each point in one direction (i.e.  $x$ -direction) is described by:

$$\Delta\omega(x,t) = \gamma(G_x(t) \cdot x). \quad [1.19]$$

The phase-encoding gradient in one direction (i.e.  $y$ -direction) causes phase accumulation to occur described by:

$$\varphi(y,t) = \gamma \int_0^t (G_y(\tau) \cdot y) d\tau. \quad [1.20]$$

The gradients are typically applied as short duration pulses in synchrony with the RF, often referred to as lobes. The controlled interplay of gradient pulses with RF pulses and data acquisition (DAQ) is referred to as an imaging pulse sequence. A pulse sequence diagram is a simple means of illustrating the time-ordered application of the RF and gradient pulses (**Figure 1-5**). After the excitation RF pulse, a gradient echo is generated by the application of a gradient of equal area but with the opposite polarity. Alternatively, a spin echo can be produced by applying a  $180^\circ$  refocusing pulse, following the excitation RF pulse.

The two variables of interest in any sequence is the echo time (TE) and the repetition time (TR). The TE is the time between the RF excitation pulse and center of the readout gradient. The TR is the time between repeating RF pulses and the readout time ( $T_{read}$ ) is the acquisition period.

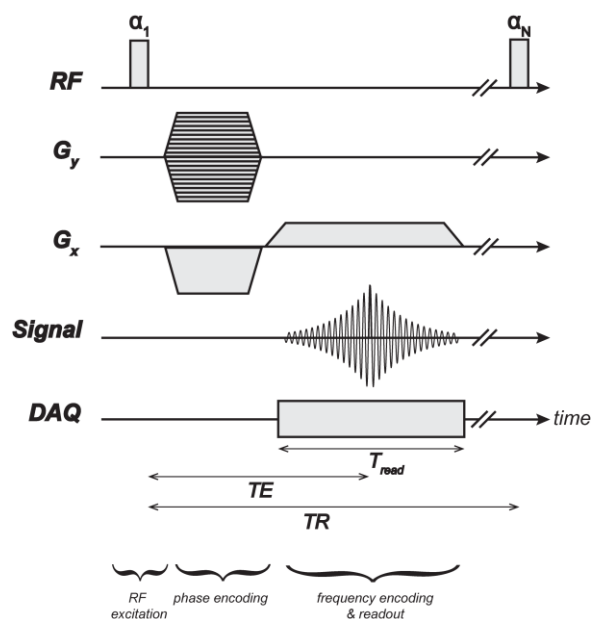


**Figure 1-5:** An example of an MRI pulse sequence diagram. The vertical axis is the amplitude and the horizontal axis is time. A pair of frequency and phase encode gradients are shown prior to the echo of the MRI signal. A readout gradient on  $G_x$  is switched on when the echo signal appears and the signal is digitized during data acquisition (DAQ).

### 1.6.2.1 Fourier Imaging and $k$ -space

In MRI, the 2-D spectrum of an object being imaged is stored in a convenient raw data matrix of individual spatial frequencies and phases, termed  $k$ -space (**Figure 1-6**). To fill  $k$ -space, the MRI scanner manipulates the object magnetization using externally applied RF pulses and spatial encoding gradients. The  $k$ -space trajectory is determined by the spatial encoding gradients. Each point of  $k$ -space is itself a spatial frequency component of the object. Objects without fine structure or detail have low spatial frequencies and the MRI signal will be concentrated in the center of  $k$ -space. The low frequency, high magnitude values that fill the center of  $k$ -space dominate the image contrast. Conversely, objects with fine detail have high spatial frequencies and the MRI signal will extend to the edges of  $k$ -space. The higher spatial frequency values of  $k$ -space data determine the detailed content of the object. Depending on the  $k$ -space ordering scheme employed (i.e. imaging pulse sequence), these details can be emphasized or reduced.



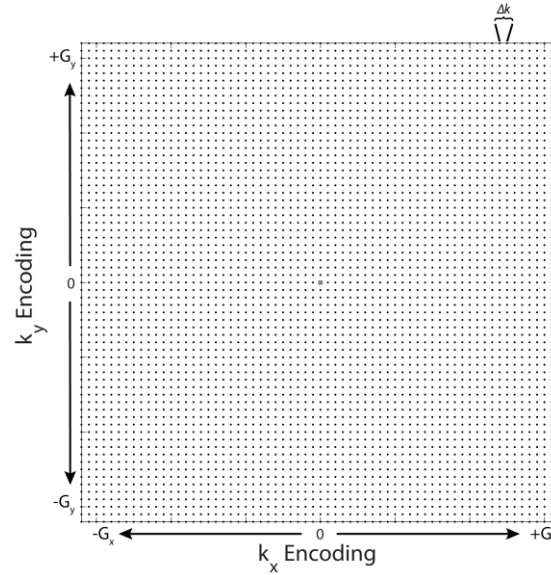


**Figure 1-6:** The 2-D  $k$ -space matrix in Cartesian coordinates.

The measured MRI signal is the sum of all the signals detected from each voxel  $m(x,y)$  of the sample:

$$S(k_x, k_y, t) = \iint m(x, y) \cdot e^{-i2\pi(xk_x(t) + yk_y(t))} dx dy. \quad [1.21]$$

The acquired signal contains the 2-D spectral information (Fourier transform) of the object:

$$M(u, v) = F_{2D} \{m(u, v)\} = \iint m(x, y) e^{-i2\pi(xu + vy)} dx dy. \quad [1.22]$$

The received MRI signal of the sample is equal to the 2-D Fourier transform of the objects initial magnetization evaluated at locations  $k_x$  and  $k_y$ . The trajectory of the applied encoding gradients determines the  $k$ -space position through the following relations:

$$k_x(t) = \int_0^t G_x(t') dt', \quad [1.23]$$

and

$$k_y(t) = \int_0^t G_y(t') dt' , \quad [1.24]$$

where  $t$  is gradient pulse duration.

The  $k$ -space matrix is in a complex form, with real and imaginary parts. The final object  $m(x, y)$  is reconstructed by applying the inverse 2-D Fourier transform of the sampled  $k$ -space data following acquisition:

$$m(x, y) = F_{2D}^{-1} \left\{ M \left( k_x(t), k_y(t) \right) \right\}. \quad [1.25]$$

This combination of complex data is referred to as a magnitude image and is the common form in MRI. The field of view (**FOV**) of the matrix prescribes the smallest volume size of the object that can be represented in the image by:

$$FOV_x = \frac{1}{\gamma \cdot \Delta G_{x,\max} \cdot \Delta t} , \quad [1.26]$$

and

$$FOV_y = \frac{1}{\gamma \cdot \Delta G_y \cdot \tau_y} , \quad [1.27]$$

where  $\Delta G_x$  and  $\Delta G_y$  is the gradient step of  $x$  or  $y$ ,  $\Delta t$  is the dwell time, and  $\tau$  is the gradient duration. The image pixel dimension is related to the dimension of the matrix:

$$\Delta x = \frac{FOV_x}{N_x} , \quad [1.28]$$

and

$$\Delta y = \frac{FOV_y}{N_y} , \quad [1.29]$$

where  $N$  is the number of sampling points in  $x$  or  $y$  direction. The receive bandwidth ( $BW$ ) is the reciprocal of the dwell time ( $\Delta t$ ):

$$BW = \frac{1}{\Delta t}, \quad [1.30]$$

where  $\Delta t$  is the time duration between digitized points.

### 1.6.3 Pulse Sequence Considerations for Hyperpolarized $^{129}\text{Xe}$

A pulse sequence is an ordered combination of gradient and RF pulses used to acquire raw data from a sample which is then used to form an image. The pulse programmer controls the pulse sequence parameters (amplitude, phase, frequency, etc...) of the imaging scan. The pulse sequence instructions are located on the console. Special consideration of the pulse sequence parameters is required because different nuclei behave differently and must be manipulated appropriately to produce an image. The pulse sequence is applied during an imaging scan to record the data using computer console software when the sample is ready to be imaged. In addition to producing spatial localization, pulse sequences have several other purposes. They generate contrast between diverse tissues and between healthy and pathological tissue. An imaging sequence needs to be capable of covering the desired anatomical structure with the appropriate contrast within a particular time frame. For example, within a single breath hold.

In MRI, there are two major categories of pulse sequences: spin echo and gradient echo. Gradient echo offers enhanced speed for hyperpolarized  $^{129}\text{Xe}$  imaging achieved by a combination of very small flip angles and short repetition times (TR). Spin echo requires large flip angles and is generally not amenable to hyperpolarized MRI and will not be discussed further in this thesis.

Unlike conventional proton MRI, hyperpolarized  $^{129}\text{Xe}$  MRI is not constrained by the need to wait for all the longitudinal magnetization to recover before the next RF pulse (i.e. saturation recovery) during imaging, therefore very short TR's are possible without sacrificing SNR. Hyperpolarization is diminished during RF pulsing required by the

imaging process. The total acquisition time is limited by hardware constraints, since the lifetime of the hyperpolarization is typically much longer than the imaging time.

In general, numerous pulse sequences exist for filling  $k$ -space. In sequential or linear  $k$ -space ordering, the line is acquired from maximum positive (negative) to maximum negative (positive) values. In the centric type of  $k$ -space ordering, the lowest frequency values are sampled first with positive and negative values alternating. This leads to contrast dominated by the beginning of the acquisition period. A particular pulse sequence is typically chosen based on ease of implementation, acquisition speed, spatial resolution, contrast, SNR, or artifact tolerance. Each type of sequence has its own limitations and tradeoffs.

#### 1.6.4 Signal-to-noise Ratio in Hyperpolarized MRI

The SNR is defined as the ratio between the signal intensity and background noise in air. In conventional proton MRI, the thermal polarization is proportional to the field strength ( $B_0$ ), thus providing better SNR at greater field strengths. Parra-Robles *et al.* (46) predicted that imaging with hyperpolarized gas at a field strength of 0.1 T is optimal to maximize clinical SNR. At higher than optimal field strengths ( $> 0.1$  T) the source of noise is typically dominated by the sample and in the case of hyperpolarized  $^{129}\text{Xe}$ , the SNR is independent of field strength. Therefore, unlike with conventional MRI, imaging with  $^{129}\text{Xe}$  at higher than optimal field strengths will not provide further SNR improvements. At lower field strengths ( $< 0.1$  T) the source of noise is typically dominated by the receiver coil and the relationship between  $^{129}\text{Xe}$  SNR and field strength is approximately linear, depending on the coil. The relationship between SNR and  $B_0$  is summarized in **Table 1-1**.

**Table 1-1:** Dependence of SNR of field strength,  $B_0$  (adapted from (47)).

	<b>Lower field (<math>&lt; 0.1</math> T)</b>	<b>Higher field (<math>&gt; 0.1</math> T)</b>
	Coil-dominated noise ( $\text{Noise} \propto B_0^{1/4}$ )	Sample dominated-noise ( $\text{Noise} \propto B_0$ )
<b>Thermally Polarized</b> ( $\text{Signal} \propto B_0^2$ )	$\text{SNR} \propto B_0^{7/4}$	$\text{SNR} \propto B_0$

$$\begin{array}{lll} \text{Hyperpolarized } ^{129}\text{Xe} & SNR \propto B_0^{3/4} & SNR = B_0 \text{ independent} \\ (\text{Signal} \propto B_0) & & \end{array}$$


---

To characterize the quality of the image it is useful to compare the signal to the background noise (SNR). SNR is a fundamental imaging metric that is often used to assess image quality:

$$SNR = \frac{S_{mean}}{\sigma_{air}}, \quad [1.31]$$

where  $S_{mean}$  is the mean of the MRI signal at a region-of-interest (ROI), and  $\sigma_{air}$  is the standard deviation of the noise measured from either an ROI in the background surrounding the object or the  $k$ -space signals acquired from an empty RF coil.

### 1.6.5 Signal Decay during Hyperpolarized $^{129}\text{Xe}$ Imaging

The general signal equation for hyperpolarized  $^{129}\text{Xe}$  gas MRI is given by:

$$S \propto P \cdot \rho \cdot \sin(\alpha) \cdot e^{(-TR/T_1)} \cdot e^{(-b \cdot \text{ADC})} \cdot e^{(-TE/T_2^*)}. \quad [1.32]$$

It contains a number of well-known terms. The initial polarization,  $P$ , nuclei density,  $\rho$ , and RF pulse,  $\sin(\alpha)$ , determine the actual signal. The  $b$ -value is a factor of diffusion weighted sequences, summarizing the influence of the gradients on the diffusion weighted signal. The apparent diffusion coefficient (ADC) summarizes the magnitude of diffusion within the tissue. A term for  $T_1$ , diffusion, and  $T_2^*$  contribute to signal decay and image blurring. All of these terms in the signal equation need to be taken into account in order to develop an efficient imaging method for low field MRI using  $^{129}\text{Xe}$ . In general, every imaging pulse sequence has a certain degree of signal attenuation due to relaxation mechanisms.

#### 1.6.5.1 Variable Flip Angles

By definition, hyperpolarized  $^{129}\text{Xe}$  is in a non-equilibrium state whereby the nuclear moments are polarized beyond the Boltzmann level. Between RF pulses during imaging, the longitudinal relaxation will not recover the polarization. Unlike  $^1\text{H}$  MRI where re-

polarization of the nuclei occurs after each RF pulse, no re-growth exists when imaging with hyperpolarized  $^{129}\text{Xe}$ . The depletion of polarization occurs due to both  $T_1$  effects and RF irradiation in the sample. When constant small flip angles are used as RF excitation pulses, the signal intensity generated from the transverse magnetization at each encoding step declines at a constant rate. This results in  $k$ -space weighting that acts as a  $k$ -space filter, which leads to significant image blurring. To avert this and compensate for the declining  $T_1$ , a variable flip angle (VFA) approach is used to manage the magnetization throughout  $k$ -space acquisition. The VFA scheme counter balances the signal decay during imaging by progressively increasing the flip angle  $\alpha$ , at each RF pulse, achieving a constant signal during  $k$ -space acquisition. The optimal flip angle progression for each  $i^{\text{th}}$  encoding can be approximated by (50):

$$\alpha_i = \tan^{-1}\{exp[-(N-i)TR/T_1]/\sqrt{N-i}\}, \quad [1.33]$$

where  $N$  is the total number of RF pulses. The final duration of the last RF pulse corresponds to a flip angle of  $90^\circ$  so that the finite polarization is used up completely at the end of the image acquisition. This leads to a constant transverse magnetization (i.e. signal) after each RF pulse. In practice, miscalibration of the transmitter or an inhomogeneous transmit field ( $B_1$ ) for the RF coil can result in undesirable flip angles (51), requiring correction by  $B_1$  mapping determined by:

$$B_{1,map} = \cos\left(\sin^{-1}\left(\frac{S_i/S_0}{\sin 45^\circ}\right)\right), \quad [1.34]$$

where  $S_i$  is the  $T_1$ -weighted image and  $S_0$  is the un-weighted image.

### 1.6.5.2 Signal Loss Due to $T_1$

The imaging time needs to take into account the lifetime of the  $^{129}\text{Xe}$  gas. The lungs contain paramagnetic molecular oxygen ( $\text{O}_2$ ) that destroys the polarization of the  $^{129}\text{Xe}$ . Essentially, the  $T_1$  relaxation of  $^{129}\text{Xe}$  magnetization is increased by the exposure to  $\text{O}_2$ . Applying multiple breaths of  $^{129}\text{Xe}$  before the full  $^{129}\text{Xe}$  bolus is inhaled for imaging washes out oxygen and therefore preserves the signal. When the hyperpolarized state is

achieved, a decay of longitudinal magnetization will occur with the  $T_1$  time relaxation constant:

$$\frac{1}{T_1} = \frac{1}{T_{1,surf}} + \frac{1}{T_{1,grad}} + \frac{1}{T_{1,O_2}}. \quad [1.35]$$

The contributions of  $^{129}\text{Xe}$  longitudinal relaxation are due to interactions with the sample surface  $T_{1,surf}$ , oxygen  $T_{1,O_2}$  and diffusion through magnetic-field gradient inhomogeneities  $T_{1,grad}$  approximated by:

$$\frac{1}{T_{1,grad}} = D_{Xe} \frac{|\nabla B_x|^2 + |\nabla B_y|^2}{B_0^2}, \quad [1.36]$$

where  $D_{Xe}$  is the self-diffusion coefficient of  $^{129}\text{Xe}$ ,  $|\nabla B_x|$  and  $|\nabla B_y|$  are the transverse magnetic-field inhomogeneities, and  $B_0$  is the static external magnetic field along the  $z$ -axis. The  $T_1$ -weighted signal is calculated and mapped by:

$$T_{1,map} = \frac{\Delta t_{os}}{-\ln(S_i/S_0)}, \quad [1.37]$$

where  $\Delta t_{os}$  is the oxygen-sensitization time delay between a normal un-weighted image,  $S_0$ , and  $p_A\text{O}_2$ -weighted image,  $S_i$ . Since  $T_1$  strongly depends on the concentration of  $\text{O}_2$  (52) it can be used to estimate alveolar oxygen partial pressure ( $p_A\text{O}_2$ ) in the lungs (53).  $p_A\text{O}_2$  is directly related to  $T_1$  relaxation due to  $\text{O}_2$  concentration by the relaxivity,  $\kappa$ , of  $^{129}\text{Xe}$  (50):

$$\frac{1}{T_1} \propto \kappa \int_0^t p_A\text{O}_2 \cdot dt, \quad [1.38]$$

where  $\kappa = 4.3 \text{ atm}^{-1}\text{s}^{-1}$  (53). Since  $T_1$  relaxation of  $^{129}\text{Xe}$  is dominated by  $\text{O}_2$ , it is possible to compute  $p_A\text{O}_2$  maps directly from a  $T_1$  map using:

$$p_{A}O_{2,map} = \frac{1}{T_1 \cdot \kappa} , \quad [1.39]$$

where  $T_1$  is inversely proportional to  $p_{A}O_2$  with a coefficient of proportionality (i.e. relaxivity)  $\kappa$  (50). The significance of  $p_{A}O_2$  measurements is the fact that an increase in  $p_{A}O_2$  is observed in regions of diseased lungs where  $O_2$  and  $CO_2$  exchange is impaired (54).

### 1.6.5.3 Attenuation due to Molecular Diffusion

The diffusion of  $^{129}\text{Xe}$  atoms can influence the observed signal decay. Molecular motion of  $^{129}\text{Xe}$  nuclei due to random collisions with other nuclei causes dephasing that is not recoverable. This random displacement of molecules resulting from the thermal energy of molecules is referred to as Brownian motion. In free space, the tendency to diffuse arbitrarily in any given direction is referred to as isotropic diffusion. On average, a molecule will remain in the same location but at any given time,  $t$ , its position,  $r$ , will be a distance away from its initial location according to the Einstein equation:

$$\langle r^2 \rangle = 6Dt , \quad [1.40]$$

where the diffusion coefficient  $D$ , statistically describes the  $^{129}\text{Xe}$  molecules traveling over a distance. In the presence of diffusion, the normal re-phasing of spins following a gradient echo becomes imperfect and the attenuation of the signal depends on spin phase dispersal. Imaging pulse sequences can be made sensitive to diffusion effects by adding a specific bipolar gradient refocusing pulse as shown in **Figure 1-7**. Essentially, the  $^{129}\text{Xe}$  MRI signal is sensitized to diffusion by the application of a bipolar magnetic field gradient pulse.



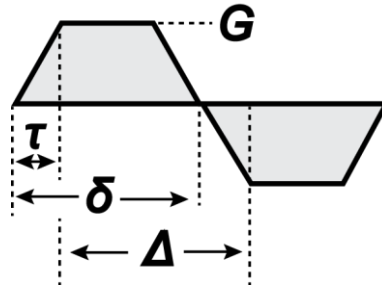


**Figure 1-7:** The diffusion bipolar trapezoidal gradient with amplitude  $G$ , ramp time  $\tau$ , lobe duration  $\delta$ , and diffusion time  $\Delta$ .

At the end of the applied diffusion gradient pulse, the accumulated phase dispersion is proportional to the root-mean-square displacement of the spins,  $\bar{x}$ , in the direction that the gradients were applied. The  $\bar{x}$  is expressed by:

$$\bar{x} = \sqrt{2Dt}, \quad [1.41]$$

where the diffusion constant,  $D$ , characterizes the gas studied at time,  $t$ . The degree of diffusion weighting is described by a  $b$ -value and depends on the shape, size, and diffusion time of the diffusion gradient pulse. For a bipolar trapezoidal pulse (**Figure 1.7**), the  $b$ -value is given by:

$$b = (\gamma G)^2 \cdot \left[ \tau^2 \left( \Delta - \frac{\tau}{3} \right) + \tau \left( \delta^2 - 2\Delta\delta + \Delta\tau - \frac{7}{6}\delta\tau + \frac{8}{15}\tau^2 \right) \right], \quad [1.42]$$

with lobe duration,  $\delta$ , ramp time,  $\tau$ , and gradient magnitude,  $G$ . The varying diffusion time,  $\Delta$ , influences the measured diffusion and is defined as the elapsed time between leading edges of the bipolar lobes. In tissues, such as the lung, free diffusion is impeded by several mechanisms, including the anatomical barriers and mixtures of molecules, leading to an *apparent diffusion coefficient* (ADC) that reflects the overall apparent diffusion measured, including the change imposed by disease. If two or more images are acquired at different  $b$ -values, the ADC can be extracted from their ratio:

$$ADC_{map} = \frac{-\ln(S_i/S_0)}{b}, \quad [1.43]$$

where the  $b$ -value dependent diffusion-weighted signal,  $S_i$ , is normalized by a non-diffusion-weighted signal,  $S_0$ , with  $b = 0$  to account for transverse relaxation effects. Increased diffusion gradient amplitudes permit higher  $b$ -values and greater diffusion weighting. An ADC map is a pixel-by-pixel representation, showing the amount of diffusion contrast in the object. Furthermore, due to restricted diffusion and anisotropy, the ADC values are expected to be a function of  $b$  and  $\mathbf{A}$  (though that is not studied in this thesis). The low self-diffusion coefficient of  $^{129}\text{Xe}$  may be desirable for certain diffusion experiments, allowing longer diffusion times more amenable to clinical hardware constraints (e.g. TE). By mixing the  $^{129}\text{Xe}$  with  $\text{N}_2$ , the diffusion-coefficient of the mixture can be increased, permitting shorter MRI diffusion experiments. The significance of diffusion measurements is that the ADC of hyperpolarized  $^{129}\text{Xe}$  can be useful for early detection of microstructural changes associated with lung disease (55).

#### 1.6.5.4 Attenuation due to $T_2^*$

A useful method to characterize material samples is by MRI transverse relaxation time, or  $T_2^*$ , measurements. The  $T_2^*$  value is directly related to the molecular movement of spin bearing molecules of interest. Some spatial frequencies can be influenced by  $T_2^*$  relaxation resulting in image blurring and loss of spatial resolution. This occurs when the high frequencies are acquired after the signal has decayed due to  $T_2^*$ . The  $T_2^*$  relaxation of  $^{129}\text{Xe}$  is strongly affected by susceptibility effects at tissue-air interfaces. Magnetic susceptibility is a natural property of tissues and a measure of how magnetized it becomes when exposed to a magnetic field. Differences in tissue susceptibility are responsible for varied degrees of magnetization in different tissues. These miniscule field changes increase the de-phasing of  $^{129}\text{Xe}$  spins around the sharp air-tissue boundaries, such as in the lungs, and thus decrease the signal intensity of the MRI signal in the area. Therefore,  $T_2^*$  decay manifests an exponential behavior over the area, giving a characteristic low signal, as well as susceptibility artifacts. The exponential  $T_2^*$  decay of  $^{129}\text{Xe}$  has a typical relaxation time of several tens or hundreds of milliseconds (depending on field strength). If the mobility of the spins is restricted, such as the case in the narrowing alveolar wall of inflamed lungs, the spin-to-spin interactions become less effective. In such cases, longer  $T_2^*$  values are expected and slower signal decays may be

observed. Therefore,  $T_2^*$  can be exploited to reveal information related to microstructure size by calculating a  $T_2^*$  map (56). The ratio of images obtained using different echo times (TE) contains useful information about  $T_2^*$  relaxation that can be extracted. The  $T_2^*$  weighted signal is calculated and mapped by:

$$T_2^*{}_{,map} = \frac{TE_i}{-\ln(S_i/S_0)}, \quad [1.44]$$

where scaling signal,  $S_0$ , and  $T_2^*$ -weighted signal,  $S_i$ , use a different TE. Since the magnetic susceptibility differences depend strongly on the magnetic field strength, the  $T_2^*$  of  $^{129}\text{Xe}$  depends strongly on the field strength. The  $T_2^*$  of  $^{129}\text{Xe}$  therefore increases at lower field strengths (< 0.1 T) because of reduced susceptibility differences. A feature exploitable but not shown for the measurements in this thesis.

### 1.6.6 Eddy Currents

Based on Faraday's law of induction, a change associated with a magnetic field induces a current in the conductor that is exposed to the field change. These currents induced in nearby conductive components of the MRI system are caused by rapid gradient switching and are known as eddy currents. The distribution and duration of the magnitude of the eddy currents depends on the gradient switching pattern, geometry of the conductor, and resistivity of the metal involved. Eddy currents generate their own fields and cause distortions in the intended waveforms when they combine, manifesting as signal loss and image artifacts. The effects of eddy currents can be reduced by using shielded gradient coils or corrected by deliberately pre-emphasizing the gradient waveforms in such a way that when they combine with the eddy current fields the output of the gradient waveform is closer to the ideal gradient waveform, called *pre-emphasis* (57). **Figure 1-8** shows an illustration of the entire effect of pre-emphasis on a trapezoidal gradient.

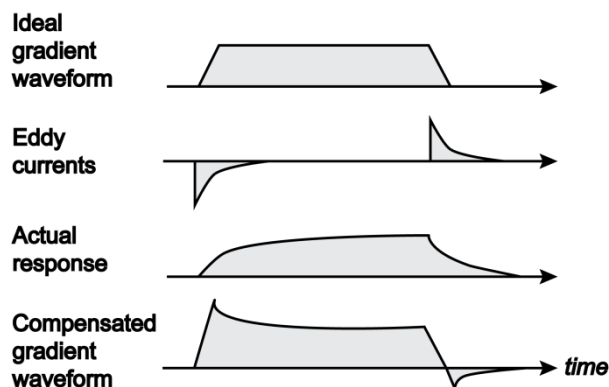


**Figure 1-8:** A schematic of gradient pulses. The eddy currents induce a magnetic field that adds to the ideal gradient waveform to form a manifested response. A compensated gradient waveform (i.e. pre-emphasis) reduces the effect of eddy currents in the desired waveform.

### 1.6.7 Cartesian Acquisitions

Conventional  $k$ -space acquisition schemes (i.e. trajectory) sample raw MRI data directly and conveniently along a Cartesian  $(x,y)$  grid. The most commonly used imaging sequence in  $^{129}\text{Xe}$  MRI is the Fast Gradient Recalled Echo (FGRE). FGRE fills the Cartesian  $k$ -space matrix using a rectilinear trajectory by sampling data line-by-line per excitation as shown in **Figure 1-9**. FGRE imaging begins with an RF pulse. The phase-encode gradient is applied along  $G_y$  that causes a column of phase accumulation in  $k_y$ -space. Then the frequency-encode gradient is applied along  $G_x$ . A negative amplitude gradient is applied at the same time as the phase-encode gradient to compensate for the later read-out gradient, to keep the echo centered.

A number of benefits of sampling with this trajectory exist. In FGRE, small flip angle techniques and reduced TR can be exploited for increased scan speed. They can be applied to provide  $T_1$ -weighted,  $T_2^*$ -weighted, and density-weighted contrast but the contrast depends on the ratio of  $T_2^*$  and  $T_1$ . Their imaging speed makes them suitable for breath-hold studies. Another benefit of Cartesian based imaging is that the acquired data is uniformly sampled and images can be quickly reconstructed using the 2-D Fourier transform. Cartesian based sequences remain popular as they are flexible and robust, provide easy implementation, and images are easily reconstructed.

Diffusion-sensitizing gradients cause a different random phase for each TR. Additionally, diffusion acquisitions require long TR on the order of seconds. Thus, increasing TR for each line will increase total scan time. The phase shifts that do occur due to local magnetic field inhomogeneities lead to  $T_2^*$  signal decay. Consequently, FGRE images are prone to phase artifacts due to magnetic susceptibility differences (58). There is no compensation in FGRE for effects of magnetic inhomogeneities and local susceptibility changes. The MRI signal decays over time due to  $T_2^*$  not  $T_2$ .

Several limitations exist for using FGRE with hyperpolarized  $^{129}\text{Xe}$  imaging. The hyperpolarized magnetization is in a non-equilibrium state and it is beneficial to minimize the number of excitation RF pulses for imaging. FGRE is undesirable for this purpose as each line of  $k$ -space data requires an RF pulse. This inefficient use of the non-renewable magnetization may lead to lower SNR. Only a few raw data lines are found near the  $k$ -space center. Furthermore, since the center of  $k$ -space is sampled after some time (i.e. TE) and not immediately after an RF pulse, significant  $T_2^*$  and diffusion effects occur. If the  $k$ -space acquisition settings are not carefully chosen, these problems may also impact non-Cartesian sampling schemes.

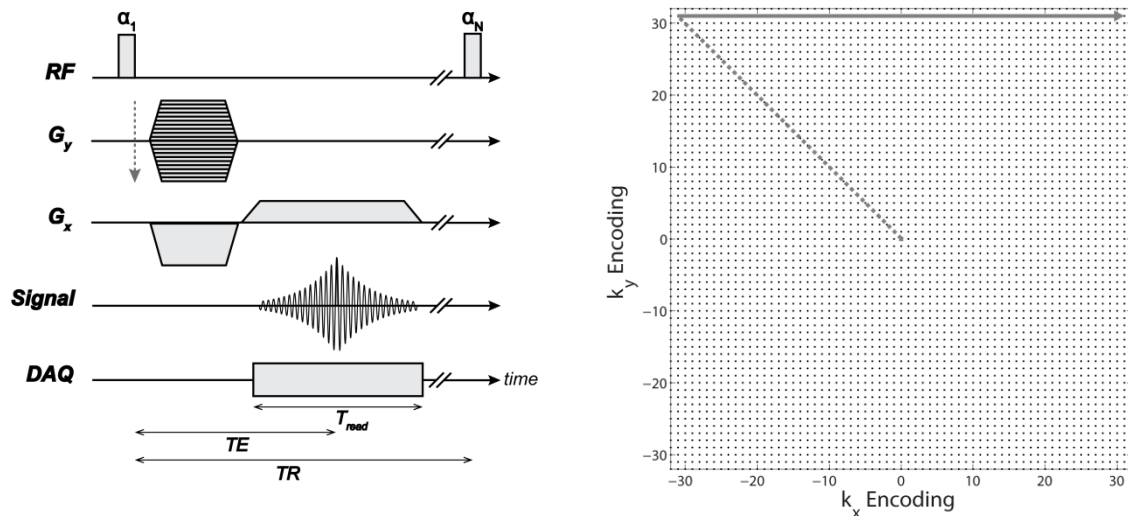


**Figure 1-9:** A pulse sequence diagram (left) and  $k$ -space trajectory (right) for the example of a FGRE Cartesian  $k$ -space acquisition.

### 1.6.8 Non-Cartesian Acquisitions

Alternatively,  $k$ -space can be sampled using a non-Cartesian trajectory. Different non-Cartesian trajectories will have different properties and implications for the reconstructed image. Various non-Cartesian strategies have been explored for hyperpolarized gas MRI, including but not limited to radial and spiral trajectories. Numerous benefits exist for sampling along a non-Cartesian trajectory based on the properties of the imaging sequence itself. An important property of non-Cartesian sequences is the rapid coverage of  $k$ -space trajectories resulting in efficient application of MRI gradient hardware. The total acquisition time is important, especially for lung imaging during single breath holds. Alternative non-Cartesian  $k$ -space trajectories have been investigated, for their time-reducing sampling capabilities. This is achieved by minimizing the number of RF excitations needed to cover  $k$ -space. In general, greater scan time efficiency is obtained with non-Cartesian acquisitions compared to conventional FGRE, through reconstruction (e.g. re-gridding) can be computationally intensive and susceptible to artifacts, often requiring careful calibration for each image.

### 1.6.9 Pseudo-Cartesian Imaging

Another approach to sampling and reconstructing imaging data efficiently involves pseudo-Cartesian algorithms. Pseudo-Cartesian strategies include the benefits of non-Cartesian trajectories without the need of special re-gridding and density weighting steps. Pure phase-encoding *Sectoral*-SPRITE is a centric technique for imaging in 2-D and 3-D (59). The  $k$ -space is filled by sampling small sectors of  $k$ -space at different orientations (**Figure 1-10**). Sampling patterns that utilize the *Sectoral* trajectory omit the  $k$ -space points outside a circle of radius equal to  $\sim 30\%$  of the matrix size in a Cartesian representation. In practice, some  $k$ -space points near the origin are also omitted. *Sectoral* lies between spiral and radial in terms of RF pulses required per image. Pseudo-Cartesian imaging with *Sectoral* has several advantages over other existing non-Cartesian trajectories. It provides images with high resolution and robust contrast using magnetization preparation methods. The *Sectoral* trajectories aim to improve SNR of the final image in a given acquisition time. No special re-gridding or density weighted steps are required before 2-D Fourier transformation. Greater uniformity and sampling

coverage occurs at the center of  $k$ -space and with the shorter divided parts of  $k$ -space trajectories (i.e. sectors) (**Table 1-2** and **Table 1-3**). Compared to radial, *Sectoral* uses fewer RF pulses which is desirable for hyperpolarized MRI. *Sectoral* is expected to use less gradient changes (duty-cycle) than spiral, resulting in a smaller  $b$ -value of the entire readout gradients. Finally, *Sectoral* has the additional advantage of reducing blurring compared to spiral or conical trajectories. After some modifications, the *Sectoral* trajectory is expected to be an appropriate strategy for  $^{129}\text{Xe}$  imaging of the lungs, particularly at low field strengths.

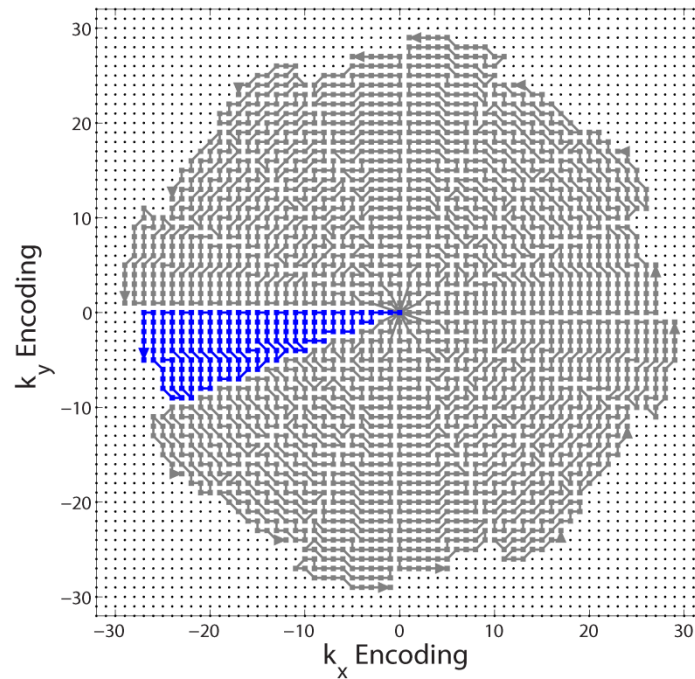


**Table 1-2:** Statistical characteristics of 2-D trajectories (59).

	<b>Spiral</b>	<b>Radial</b>	<b>Sectoral</b>
<b>Sector</b>	1	32	32
<b>Coverage (%)</b>	80.3	33.3	99.9
<b>Average sector (pts)</b>	2564	30	93
<b>Sector SD (%)</b>	0.0	16.2	10.3

**Table 1-3:** Statistical characteristics of 3-D trajectories (59).

	<b>Radial</b>	<b>Conical</b>	<b>Sectoral</b>
<b>Sector</b>	1026	1005	987
<b>Coverage (%)</b>	26.1	78.8	99.9
<b>Average sector (pts)</b>	37	115	127
<b>Sector SD (%)</b>	9.9	15.7	3.8

## 1.7 Sectoral Pulse Sequence for Hyperpolarized $^{129}\text{Xe}$ in the Low-Field MRI System

### 1.7.1 Gradient Waveform Characterization

The proposed *Sectoral* sequence involves strong read-out gradients and fast gradient switching simultaneously in two directions (**Figure 1-13**) to assure short encoding times. Inevitably, the application of pulsed magnetic-field gradients gives rise to eddy-currents in the sample, resulting in undesired gradient waveforms. During MRI, these eddy-current-induced gradients can further reveal themselves as degradations and artifacts in resulting images, particularly as geometric distortions (60). Unlike FGRE, the  $k$ -space traversal trajectory of *Sectoral* is non-rectilinear. Therefore, knowing the exact gradient waveforms becomes increasingly important. More specifically, the precise knowledge of data sample locations in  $k$ -space, corresponding to the applied waveforms, is crucial for *Sectoral* imaging.

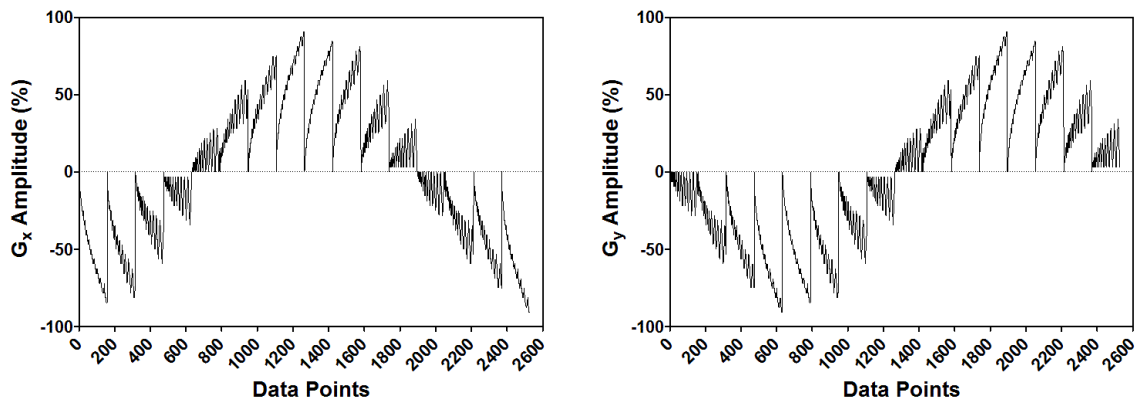


**Figure 1-10:** Pure phase-encoding gradient waveforms for a *Sectoral* sequence of ideal  $G_x$  (left) and ideal  $G_y$  (right).

Gradient waveform characterization provides a tool to measure the actual  $k$ -space locations and correct for any non-idealities caused by hardware imperfections. The pure phase encode magnetic field gradient monitor (MFGM) technique can be applied to identify and correct the root cause of magnetic field gradient corruption due to eddy-



currents in an MRI experiment (61). MFGM directly measures the temporal evolution of the magnetic field gradient from an input function and extracts the system impulse response. The impulse response is then used to prepare an optimized pre-emphasis input waveform that provides a desired gradient response (57).

During MFGM, continuous RF pulses measure the duration of waveforms without limitation on  $T_2^*$  decay. To avoid gradient dephasing, MFGM manages small separate gradient areas with a short phase-encoding time. MFGM relies on a small “pick-up” coil with an associated test sample to temporally and spatially monitor the gradient behavior of the sample space adjacent to the pick-up coil. With the MFGM approach it is desirable to receive a signal from a point source at a known offset from the gradient origin. MFGM permits multiple axes to be simultaneously measured. Eddy-current pre-emphasis compensation by modulation of gradient switching can further suppress the effects of unwanted persistent eddy currents in the MRI system.

### 1.7.2 *Sectoral* Pulse Sequence

The method proposed here for  $^{129}\text{Xe}$  MRI of the lungs at low magnetic field relies on the non-Cartesian trajectory of the *Sectoral*-SPRITE sequence (59). *Sectoral*-SPRITE is a pure phase-encoding technique that requires a single RF pulse for each sampled  $k$ -space corresponding data point. For example, a  $64 \times 64$  *Sectoral*-SPRITE image requires 2528 RF pulses to sample 2528 data points. This undesirable feature for  $^{129}\text{Xe}$  MRI is rectified by transforming the *Sectoral*-SPRITE sequence to a pure frequency-encoding *Sectoral* sequence, referred to simply as *Sectoral* hence on. *Sectoral* follows the same  $k$ -space trajectory as *Sectoral*-SPRITE but only requires a single RF pulse per sector. **Figure 1-14** illustrates a *Sectoral* pulse sequence diagram (left) from one of multiple  $k$ -space traversal trajectories (right) that make up a sector.

Two modes of *Sectoral* acquisition are developed and implemented in this thesis by making modifications to the imaging pulse sequence and data handling. The first is a mode in which the entire data acquisition is performed following a single gas insertion or breath hold and is referred to as single-breath *Sectoral*, or SB-*Sectoral*. In SB-*Sectoral*, all sectors are acquired from a continuous series of RF pulses, one pulse to the next, until

the entire imaging scan is complete and the magnetization has been fully depleted. The second is a multi-sector mode in which only a specified sector of the entire  $k$ -space acquisition (e.g. one sixteenth) is acquired following each gas insertion or breath hold and is referred to as multi-breath *Sectoral*, or *MB-Sectoral*. In *MB-Sectoral*, consecutive sectors are then repeated following a fresh gas insertion using individually applied pulse sequences, each requiring a separate scan. This results in improved SNR, at the expense of increased scan time.

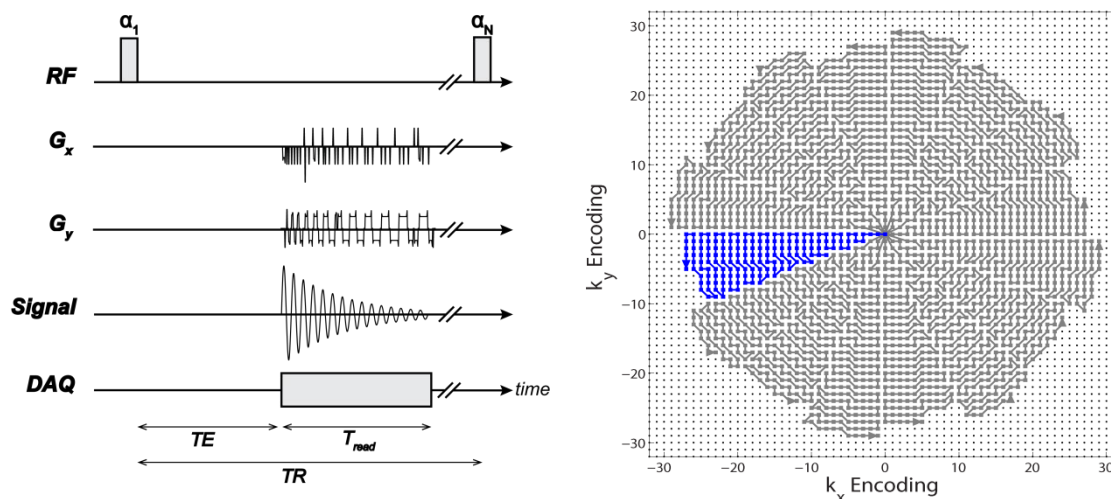


**Figure 1-11:** An example of a pulse sequence diagram (left) of a single  $k$ -space trajectory (blue sector) for a 16-sector *MB-Sectoral* acquisition (right).

### 1.7.3 $T_1$ and $p_AO_2$ Mapping

$T_1$  weighting (described in [section 1.6.5.2](#)) can be extracted from the ratio of two or more  $^{129}\text{Xe}$  images acquired during the same breath hold using *SB-Sectoral*, or multiple breath holds using *MB-Sectoral*. This temporal evolution of  $p_AO_2$  is extracted from the  $^{129}\text{Xe}$  signal decay curves of multiple appropriately timed *Sectoral* images acquired within a single breath hold. The  $p_AO_2$  mapping techniques based on this principle offers an opportunity to probe the regional changes associated with both instantaneous  $O_2$  concentration and rate of change.

### 1.7.4 Diffusion Mapping

ADC weighting (described in [section 1.6.5.3](#)) can be extracted from the ratio of two or more  $^{129}\text{Xe}$  images acquired during the same breath hold using *SB-Sectoral*, or multiple

breath holds using MB-*Sectoral*. In practice, the *Sectoral* technique can be sensitized to diffusion by inserting an appropriate bipolar gradient pulse, as illustrated in **Figure 1-15**.

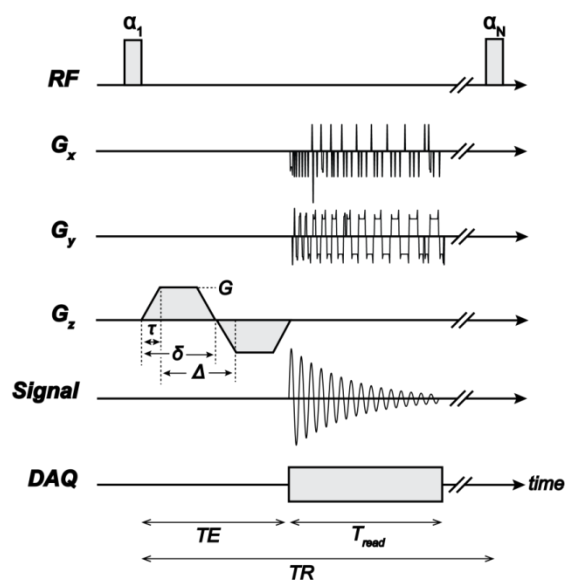


**Figure 1-12:** A diagram of the diffusion-weighted *Sectoral* pulse sequence including a bipolar trapezoidal gradient pulse with diffusion time,  $\Delta$ , lobe duration,  $\delta$ , ramp time,  $\tau$ , and gradient magnitude,  $G$ .

### 1.7.5 Post Processing

Post-processing methods refer to the manipulations of the signal or image that is performed to create the image (e.g. inverse Fourier transform), improve the MRI signal, signal-to-noise ratio (SNR), visual appearance of the image, or the accuracy of estimates of signal parameters (62). The MRI signal can be processed in either the time domain (i.e. free induction decay (FID)) or the frequency domain (i.e. spectrum), or both. Possible artifacts may be more pronounced in one domain over the other. Therefore, various post-processing techniques can be used depending on which domain is used and some may be applied in both domains with similar results. Although the signal, or image, may be enhanced by post-processing, the improved visual appearance of the signal or image may be at the expense of information. Filtering MRI data can improve SNR by increasing the magnitude of the low spatial frequencies at the cost of reducing spatial resolution by attenuating the high spatial frequencies, where the electronic noise is more pronounced. The following post-processing techniques have been applied in this thesis (62,63): signal

filter, zero fill, phase correction, baseline correction, conjugate  $k$ -space average, hamming filter, and a Rician noise distribution-based estimation.

## 1.8 Hypothesis and Objectives

The hypothesis of this research is as follows: *Sectoral* imaging for  $^{129}\text{Xe}$  lung imaging will provide improved SNR efficiency compared to conventional FGRE. Furthermore regional apparent diffusion coefficient reductions will be measurable using hyperpolarized  $^{129}\text{Xe}$  *Sectoral* MRI in a rodent model of RILI at low magnetic field that are consistent with histology.

The specific goals of this study include:

- (1) Implement and optimize the *Sectoral* pulse sequence on a  $^{129}\text{Xe}$  phantom using low field MRI.
- (2) Test and verify the advantage of the *Sectoral* imaging pulse sequence, over FGRE, by implementing it with a low field strength MRI system to image  $^{129}\text{Xe}$  in a phantom.
- (3) Modify the *Sectoral* sequence for structural and functional imaging, including ADC and  $p_{\text{A}}\text{O}_2$  mapping and test them on a phantom.
- (4) Perform *in vivo* rat lung  $^{129}\text{Xe}$  *Sectoral* measurements at low field.
- (5) Use structural mapping, including ADC, for investigations of rodent lung models of RILI. The objective is to investigate changes occurring in rat lungs using *Sectoral*.
- (6) Lastly, to compare imaging results with quantitative histology.

## 1.9 Thesis Outline

The work reported in this thesis was completed by me under the direct supervision of Dr. Giles Santyr in the Imaging Research Laboratories at Robarts Research Institute as a M.Sc. student in the Department of Medical Biophysics at Western University. This thesis work is a collaborative project between myself, Dr. Santyr, Dr. Alexei Ouriodov, and colleagues in Dr. Santyr's research group who assisted on occasion (e.g. Elaine

Hegarty). The following is an outline of the rest of my thesis and the explicit account of everyone's contributions are as follows:

**Chapter 2** outlines the research materials and methods used in the thesis for both *in vitro* and *in vivo* experiments. The implementation, utilization and calibration procedures for *Sectoral* and FGRE on a low field MRI system are detailed. The chapter also includes the methodologies for animal and gas preparation, histological and statistical analysis, image processing and SNR efficiency calculations.

**Chapter 3** presents the results from the experimental procedures described in **Chapter 2**. MRI using *Sectoral* and FGRE sequences *in vitro* are compared on the basis of SNR efficiency. *Sectoral* maps of ADC,  $T_1$ , and  $p_{AO_2}$  from a syringe phantom filled with different mixtures of  $^{129}\text{Xe-N}_2$  or  $^{129}\text{Xe-O}_2$  are demonstrated. The chapter concludes with rat lung ventilation and ADC maps from a pilot study using irradiated and healthy rat lungs.

**Chapter 4** discusses the findings from **Chapter 3** and gradient waveform mapping used in **Appendix A**. The optimization of the gradient waveform mapping technique, low field MRI hardware, and *Sectoral* imaging technique will be important in future work for further *in vivo* studies. Conclusions are drawn on the basis of the results obtained. Mainly that *Sectoral* shows promise to be a favourable tool for hyperpolarized  $^{129}\text{Xe}$  lung imaging at low field over the conventional FGRE approach.

I, Krzysztof Wawrzyn, operated and maintained the low field MRI system. I helped Dr. Ouriadov with the gradient waveform mappings, in particular with the phantom preparation, making the step-like waveform, and acquiring data. All pulse sequence control and calibration (VFA, shimming, etc...) was performed by me. I acquired all the MRI data and coded my own MATLAB routines, some of which I have adopted from previously developed IDL scripts prepared by Dr. Ouriadov. All image processing and analysis, including  $T_1$ ,  $p_{AO_2}$ , and ADC mapping, was done by me. I am solely responsible for performing all of the *in vitro* (phantom) experiments and I had assistance from Elaine Hegarty during all of the *in vivo* experiments. I operated the xenon polarizer and collected  $^{129}\text{Xe}$  for all of my experiments. I am responsible for constructing the

syringe flow through phantom used in this work. Occasionally, I helped perform maintenance on the polarizer (i.e. cutting tubes, leak tests, filter change etc...).

Dr. Giles Santyr provided overall guidance for the project and provided consultations and assistance with the thesis preparation.

Dr. Alexei Ouriadov programmed the original FGRE and *Sectoral* pulse sequences on the low field MRI system, as well as the initial data processing scripts in IDL. Dr. Ouriadov provided consultation and advice with the work involved in this thesis.

Elaine Hegarty, under the supervision of Dr. Santyr, assisted with operating the animal ventilator, doing all animal preparations during the *in vivo* experiments, performing histological preparation and interpretation, animal irradiations, rubidium filling of xenon cell, xenon polarizer maintenance.

Susannah Hickling, a previous 4<sup>th</sup>-year thesis student, worked on the *Sectoral* sequence. The MFGM technique used for her project employed a single RF pulse, but required greater waveform characterization time, and did not utilize normalization coefficients or pre-emphasis waveforms. She employed a previously developed, un-optimized *Sectoral* sequence for her thesis and used simulations requiring interpolation algorithms to account for non-ideal  $k$ -space trajectories, that required the calibrations described in this thesis in order to be reduced to practice.

## Chapter 2: Methodology

### 2 Introduction

In this chapter, the feasibility of producing images of phantoms filled with  $^1\text{H}$  (i.e. doped water) or hyperpolarized  $^{129}\text{Xe}$  using a novel unpublished imaging pulse sequence, called *Sectoral*, is described. The phantom measurements were performed at 74 mT using a home-built MRI system for small animal and phantom imaging (64). Both *Sectoral* and Fast Gradient Recalled Echo (FGRE) imaging were compared on the basis of SNR efficiency. This chapter details the procedures performed and explains the *Sectoral* mapping techniques for apparent diffusion coefficients (ADC), longitudinal relaxation time ( $T_1$ ), and alveolar partial pressure of oxygen ( $p_{\text{A}}\text{O}_2$ ) with hyperpolarized  $^{129}\text{Xe}$  within phantoms, in preparation for *in vivo* rat lung imaging. This chapter also includes the procedures for an *in vivo* pilot study where irradiated and healthy rat lungs were investigated using the diffusion-weighted *Sectoral* sequence and compared to histological interpretation.

#### 2.1 Xenon-129 Polarization and Delivery

The  $^{129}\text{Xe}$  gas was hyperpolarized by spin-exchange optical pumping (SEOP) with an in-house, custom-built, polarizer system (64). Naturally abundant  $^{129}\text{Xe}$  (26.4%) was polarized to levels of up to 5% in the continuous flow state. A gas mixture of 0.97% naturally-abundant xenon gas (containing 26%  $^{129}\text{Xe}$ ), 89.15% helium-4, and 9.86% nitrogen (Air Liquide, Burlington, Ontario, Canada) was introduced into the polarizer system. The gas flowed through the gas lines at a pressure of  $\sim 8.0$  PSI. A flow regulator controlled the flow rate through the system at 0.60 L/m during gas preparation. Residual  $\text{O}_2$  and moisture were removed from the lines to prevent contact with the rubidium using  $\text{O}_2$  (Chromatography Research Supplies, Louisville, USA) and water (Supelco, Bellefonte, USA) filters, respectively. Rubidium was heated from a glass trap, containing  $\sim 1.0$  g of rubidium, to  $\sim 270$  °C and the vaporized rubidium made contact with the gas mixture which flowed into an optical cell situated within a solenoid coil that produced a 50 Gauss homogenous magnetic field. A 60-W fiber laser (Coherent Inc., Santa Clara,

CA, USA) was used to illuminate the optical window of the cell in order to polarize the rubidium using circularly polarized light at 795 nm. The polarization of the rubidium electrons was then transferred to the  $^{129}\text{Xe}$  nuclei by collisions with the polarized rubidium. To avoid de-excitation (i.e. fluorescence) of the rubidium by reabsorption of photons from radiative decay of the excited state, a small amount of  $\text{N}_2$  in the mix was used as a buffer gas.  $\text{N}_2$  suppresses the re-radiation of photons by quenching the excited rubidium atoms. After exiting the optical cell, the gas mixture flowed through a filter filled with fiberglass wool to remove any rubidium atoms, which could otherwise depolarize the gas. After leaving the polarizer, the gas mixture passed through a 5-turn linear horizontal glass trap that was submerged in an insulated liquid nitrogen bath and surrounded by a 0.3 T permanent magnet. The xenon gas was cooled by the liquid nitrogen until it condensed, allowing the other gases to ventilate into the atmosphere. A typical collection time of 70 minutes resulted in a volume of  $\sim 360$  ml of xenon gas to accumulate in the trap. Following collection, the glass trap was vacuumed to remove any residual gasses. The glass trap was then rapidly heated with boiled water and the hyperpolarized xenon was thawed into a 360 ml sized Tedlar<sup>®</sup> bag (Jensen Inert, Coral Springs, USA).

## 2.2 Phantom Preparation

To determine the accuracy of the *Sectoral* imaging sequence and processing algorithm, two types of phantoms were used. To test the performance of the *Sectoral* sequence, the spatial resolution was assessed using a resolution phantom. A photograph of the cylinder-shaped acrylic resolution phantom is shown in **Figure 2-1**. The resolution phantom is a cylindrically shaped container, which holds an array of solid Delrin blocks of different dimensions, ranging in diameter from 2.0 mm to 10.0 mm. The resolution phantom had a diameter of 51 mm, depth of 30 mm, and volume of 33 ml. A second phantom (**Figure 2-2**) was constructed from two syringe tubes with a diameter of 20 mm and volume of 10.0 ml. This flow-through syringe was used to test the feasibility of the modified *Sectoral* sequence for structural and functional mapping. Both phantoms in this work were sealed, hollow and fillable with either water or  $^{129}\text{Xe}$  gas. *Sectoral* imaging was performed with  $^1\text{H}$  prior to  $^{129}\text{Xe}$ .



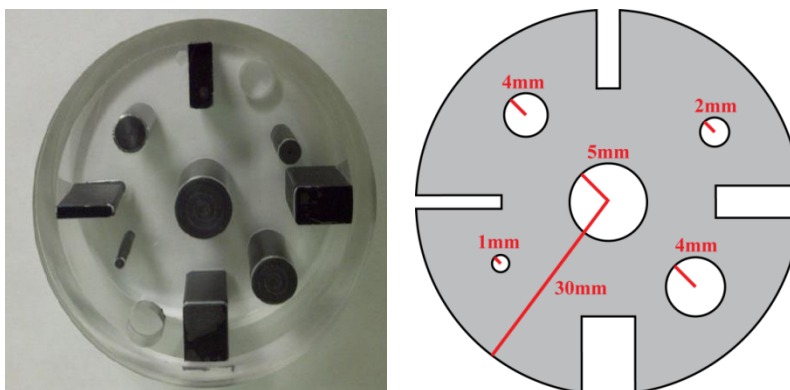


**Figure 2-1:** Photograph of the acrylic resolution phantom (left) and a corresponding schematic diagram with shown dimensions. The  $^{129}\text{Xe}$  gas resides in the empty space of the phantom container.



**Figure 2-2:** Photograph of the flow-through syringe phantom.

## 2.3 Animal Preparation

All animal procedures followed humane animal handling and protocols approved by Western University's Animal Care and Veterinary Services (AUP Number: 2007-083-09) and were consistent with procedures used by the Canadian Council on Animal Care (CCAC).

### 2.3.1 Irradiations

Nine male Sprague-Dawley rats (weight =  $444 \pm 29.6$  g on imaging) were obtained from Charles River Laboratories (Wilmington, MA) and divided into two cohorts: (i) irradiated and (ii) age-matched healthy control. The setup is shown in **Figure 2-3** Prior to irradiation, rats were anesthetized within a chamber using 5.0% isoflurane (VetEquip, Pleasanton, CA) delivered by a vaporizer (VetEquip, Pleasanton, CA). Once sedated, the

rats were then transferred to a nose cone mask with 2.0% flowing isoflurane and secured in a polyvinyl box. Four of the rats were irradiated uniformly with a total dose of 14 Gy using a  $^{60}\text{Co}$  source gamma irradiator at the London Regional Cancer Program center. The rats were irradiated for a total of 14 minutes (6.5 min in prone and 7.5 min in supine position) at a dose rate of  $134 \pm 1$  cGy/min at the calibration level for the distance of the lung from the  $^{60}\text{Co}$  source. The exposure times differed due to the positioning adjustments of the lungs at distances of 11 cm (prone) and 14 cm (supine). An animal positioning stage with a lead collimator (diameter = 4 cm) was used to deliver the radiation dose to the entire thorax. To ensure uniform dose, half of the dose was delivered to the rats in the supine position and the other half was delivered in the prone position. The rats were monitored daily for two weeks following the irradiation treatment. *Sectoral* imaging experiments (**section 2.7.1**) were performed two weeks post-irradiation to allow sufficient inflammation to occur due to the RILI response.

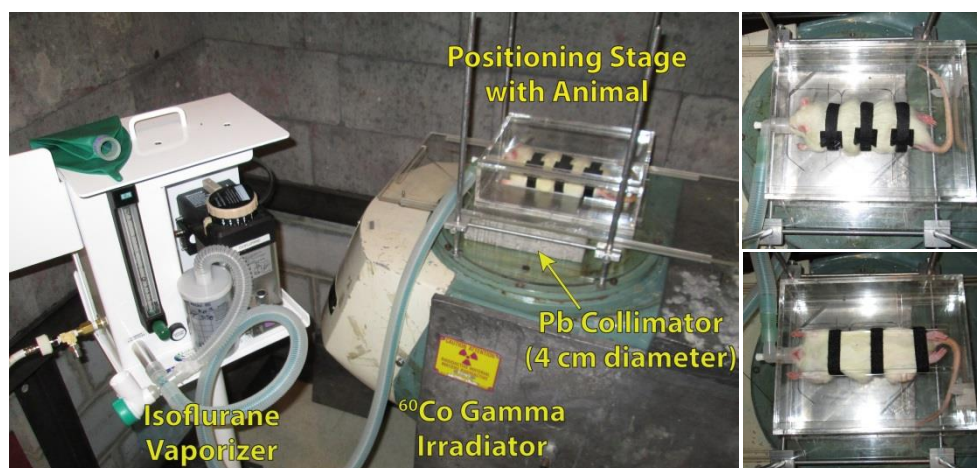


**Figure 2-3:** Photograph of  $^{60}\text{Co}$  irradiator with animal positioning system and isoflurane vaporizer (left). Positioning system seen from top view showing custom-built animal positioning stage and lead collimator with rat in prone (top-right) and supine (bottom-right) positions.

### 2.3.2 Surgical Procedure

All surgical procedures were done under deep anesthesia to prevent pain, distress or impairment to the animals. Prior to imaging, the rats were anesthetized using 5.0% isoflurane gas (Baxter Corporation, Mississauga, Canada) within a chamber using a vaporizer (VetEquip, Pleasanton, CA). Once sedated, the rats were then transferred to a

face mask with 2.0% flowing isoflurane gas. A bolus dose of ketamine (Bioniche Animal Health, Belleville, Canada) was given intramuscularly. A 26 G catheter was inserted into the tail vein. A bolus dose of propofol (AstraZeneca, Mississauga, Canada) was given intravascular. Rats remained unconscious for the entire duration of the experiment with a continuous dose of 10:1 propofol and ketamine intravascular at a dose rate of 45-60 mg/kg/h. To reduced salivary and tracheobronchial secretions, 5 IU of glycopyrrolate was administered intramuscularly. Lacrilube® (Allergan Inc, Markham, Canada) eye ointment was applied to both eyes to minimize the effect of dehydration. 0.25% Sensorcaine® was injected subcutaneously in the neck for local anesthesia. A 2.0 cm incision was made across the neck skin in order to expose the trachea for tracheal ligation. The rats were tracheostomized with a 16 G endotracheal tube (Becton Dickinson, Franklin Lakes, NJ). The trachea was tied tightly around the endotracheal tube using sutures (Johnson & Johnson, Ethicon, New Brunswick, NJ) to facilitate the isolation of the trachea and prevent  $^{129}\text{Xe}$  from leaking out and depolarizing.

### 2.3.3 Ventilation

Following surgery, the rats were transferred to the MRI system and placed supine in the RF coil while connected to an MR-compatible mechanical animal ventilator (GEHC, Malmo, Sweden) as shown in **Figure 2-4**. The rats were ventilated with medical air at a rate of 60 breaths per minute. Tedlar® bags filled with  $^{129}\text{Xe}$  were kept inside a pressurized reservoir in proximity of the magnet bore and connected to the ventilator. Breath holds of  $^{129}\text{Xe}$  were performed during imaging at a peak inspiratory pressure (PIP) of 12 cm H<sub>2</sub>O with each breath hold. Following the MRI experiments, rats were euthanized by intravenous injection of Euthanyl Forte (Bimeda-MTC, Cambridge, Canada). Post-mortem, rat lungs were extracted for histological interpretation described in **section 2.8**.

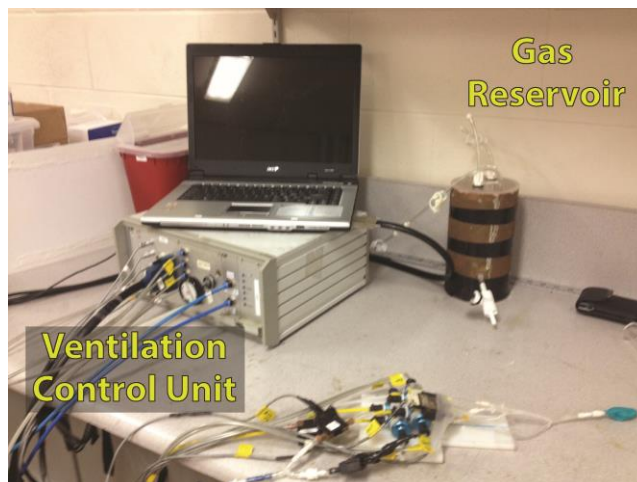


**Figure 2-4:** Animal ventilation control unit with gas reservoir.

## 2.4 Low Field MRI

All MRI was performed using a custom-built 74 mT low field resistive MRI system (**Figure 2-5**) equipped with a maximum  $x$ ,  $y$ , and  $z$  gradient intensity of 180 mT/m (64). The homogeneity of the  $\vec{B}_0$  field in this MRI system was  $\sim 65$  ppm and  $\sim 10$  ppm before and after passive and resistive gradient shimming, respectively. Passive shimming involving physical placement of ferrous material (i.e. pieces of steel) around the magnet, followed by resistive gradient shimming using additional windings built into the gradient coil subsystem, was beneficial. The magnet bore had a diameter of 18 cm and was oriented along the horizontal direction ( $z$ -axis). Two DC power supplies (XKW 80-37 Xantrex Technologies, Burnaby, BC, Canada) were used to power the magnetic field (79 V, 47.4 A, 3744 W). Chilled water circulating through hollow aluminum plates attached to the windings was used to cool the magnet. To filter out high frequency noise ( $>1.5$  MHz), three low-pass hardware filters ( $1 \times 3.0$  and  $2 \times 1.5$  MHz) were installed in the receive chain between the digital signal processor and RF amplifier for all  $^{129}\text{Xe}$  measurements.

Imaging samples were placed in a custom built transmit-only and receive-only saddle coil built using Litz wire (Kerrigan Lewis Wire Products, Chicago, IL) to reduce RF coil noise at low field frequencies (65). Two 8.5-cm-diameter rat-sized RF coils (**Figure 2-6**) tuned to different resonance frequencies (0.883 MHz for  $^{129}\text{Xe}$  and 3.163 MHz for  $^1\text{H}$ )

were used. A Tecmag Apollo LF-1 spectrometer (Tecmag Inc., Houston, TX, USA), triggered and controlled by Tecmag NTNMR version 2.4.24 pulse sequence software, was used to control the RF and gradient pulses, signal detection, and imaging pulse sequence timing. A low-pass digital filter on the console was used (1/3 or 1/5.5 of the sweep-width for *in vitro* or *in vivo*, respectively) for all sequences to increase SNR. The raw data were collected directly on the same workstation.

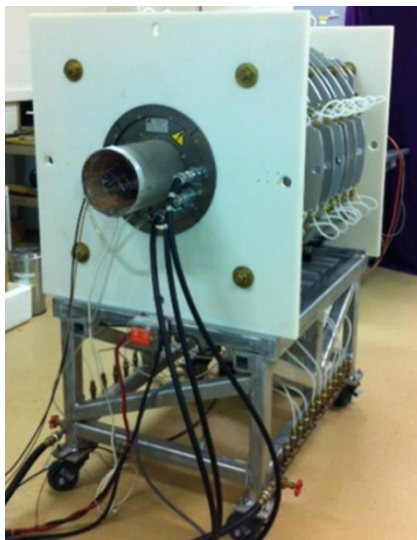


**Figure 2-5:** Low magnetic field (74 mT) MRI system.



**Figure 2-6:** Transmit only/receive only saddle RF coil tuned to 0.883 MHz ( $^{129}\text{Xe}$ ) or 3.163 MHz ( $^1\text{H}$ ).

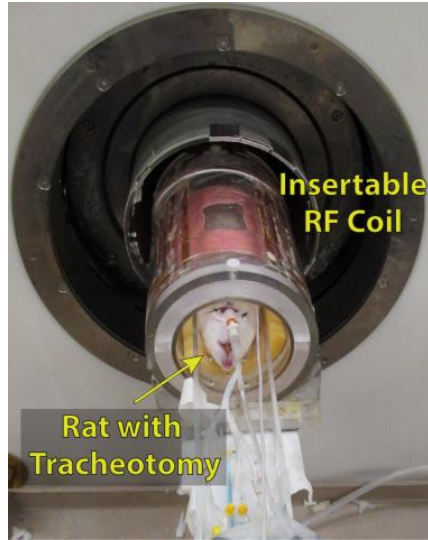


**Figure 2-7:** Insertable RF coil with tracheostomized rat.

## 2.5 *In Vitro* FGRE MRI Experiments

A 2-D fast gradient recalled echo (FGRE) sequence with centric phase-encoding was implemented on the low field MRI system. This type of sequence utilizes short TR ( $TR \ll T_1$  and  $< T_2^*$ ) made possible as  $^{129}\text{Xe}$  is not constrained by saturation recovery during imaging. The final sequence employed a matrix size of  $64 \times 64$ , and hence used 64 RF pulses to repeatedly refocus the echoes. The duration of each RF pulse was determined through a variable flip angle (VFA) scheme (66). Each applied RF pulse had a longer pulse width than the previous one with the aim of equalizing the signal intensity. In order to make an unbiased comparison to *Sectoral* acquired images, only the first 63% ( $N = 40$ ) of the echo phase-encoding was sampled. During the pre-scan calibration step a free induction decay (FID) of pre-freeze thawed  $^{129}\text{Xe}$  in the syringe phantom was acquired to check  $T_2^*$ . Prior to reconstruction, the matrix was zero-padded to produce a final  $64 \times 64$  image. The pulse sequence parameters for  $^1\text{H}$  imaging were:  $FOV = 87 \times 87 \text{ mm}^2$ ,  $\Delta x$  and  $\Delta y = 1.36 \times 1.36 \text{ mm}^2$ ,  $TR/TE = 600/5 \text{ ms}$ ,  $\Delta t = 20 \text{ } \mu\text{s}$ ,  $T_{read} = 12.8 \text{ ms}$ ,  $BW = 50 \text{ kHz}$ . In order to compare efficiency of FGRE imaging of hyperpolarized  $^{129}\text{Xe}$  with *Sectoral*, a 10.0 ml flow-through syringe phantom was used. For the case of  $^{129}\text{Xe}$  imaging, the FGRE pulse sequence parameters were:  $FOV = 76 \times 76 \text{ mm}^2$ ,  $\Delta x$  and  $\Delta y = 1.18 \times 1.18 \text{ mm}^2$ ,  $TR/TE = 10/4.8 \text{ ms}$ ,  $\Delta t = 20 \text{ } \mu\text{s}$ ,  $T_{read} = 12.8 \text{ ms}$ ,  $BW = 50 \text{ kHz}$ .

## 2.6 *In Vitro* Sectoral MRI Experiments

The *Sectoral*  $k$ -space trajectories were generated based on the analytical solutions of Khrapitchev (59). **Figure 1-14** shows the *Sectoral* pulse sequence diagram and complete  $k$ -space trajectory. First, an RF pulse of tip angle  $\alpha$  was applied to flip the magnetization into the transverse plane. Second,  $x$ -axis and  $y$ -axis frequency-encoding gradients were applied simultaneously throughout the readout window. Finally, the entire sequence was repeated for all 16 sectors of the  $k$ -space traversal trajectory, requiring 16 RF pulses. The VFA for each RF pulse was calibrated separately using **Eqn. [1.33]** as described in **section 1.6.5.1** and **section 2.9**.

A dead-time delay of 3 ms was added between the RF excitation and gradient waveform to reduce receiver over-voltage leading to a ring down response. Each sector waveform consisted of 1432 acquisition points. Every eighth acquisition point corresponds to a data point in  $k$ -space that fell directly onto a Cartesian grid, for a total of 158  $k$ -space points per sector. For 16 sectors of a  $64 \times 64$  matrix, the total number of sampled data points was 2528.

The pulse sequence parameters for  $^1\text{H}$  imaging were:  $FOV = 71 \times 71 \text{ mm}^2$ ,  $\Delta x$  and  $\Delta y = 1.11 \times 1.11 \text{ mm}^2$ ,  $TR/TE = 600/10 \text{ ms}$ ,  $\Delta t = 35 \text{ }\mu\text{s}$ ,  $T_{read} = 50.12 \text{ ms}$ ,  $BW = 28.5 \text{ kHz}$ . In order to compare efficiency of FGRE imaging of hyperpolarized  $^{129}\text{Xe}$  with *Sectoral*, a 10.0 ml flow-through syringe phantom was used. For the case of  $^{129}\text{Xe}$  imaging, the FGRE pulse sequence parameters were:  $FOV = 90 \times 90 \text{ mm}^2$ ,  $\Delta x$  and  $\Delta y = 1.4 \times 1.4 \text{ mm}^2$ ,  $TR/TE = 13/3 \text{ ms}$ ,  $\Delta t = 90 \text{ }\mu\text{s}$ ,  $T_{read} = 128.88 \text{ ms}$ ,  $BW = 11.1 \text{ kHz}$ .

### 2.6.1 $T_1$ and $p_{\text{A}}\text{O}_2$ Experiments

The short breath hold technique to measure  $p_{\text{A}}\text{O}_2$  was demonstrated in phantoms using *Sectoral* imaging. That is,  $p_{\text{A}}\text{O}_2$  mapping from a single pair of  $T_1$  weighted *Sectoral* images, acquired a few seconds apart during the same breath hold. To generate  $T_1$  weighting, two *Sectoral*  $^{129}\text{Xe}$  images separated by an oxygen-sensitization time  $\Delta t_{os}$  were obtained. During the  $\Delta t_{os}$  interval, the magnetization decayed by natural  $T_1$  relaxation, whereas during acquisition the RF pulses consume magnetization faster while



accounted for by VFA. This *Sectoral* pulse sequence allows  $T_1$  maps to be obtained by extracting the pixel-by-pixel ratio of the generated images and using **Eqn. [1.37]**. Three phantom experiments (1×MB-*Sectoral* and 2×SB-*Sectoral*) were performed to verify that regional  $p_{A}O_2$  distributions could be accurately measured with *Sectoral*. In each experiment, the syringe flow-through phantom was vacuumed and a measured volume of  $O_2$  was injected. Immediately prior to imaging, the  $^{129}Xe$  from an isolated Tedlar<sup>®</sup> bag was injected into the syringe flow-through phantom. The phantom was then sealed off and the imaging sequence was initiated. Non-selective RF excitations using VFA were used for all scans to obtain 2-D projection images. The *Sectoral*  $p_{A}O_2$ -mapping pulse sequence parameters were: matrix = 64×64,  $FOV = 90 \times 90 \text{ mm}^2$ ,  $\Delta x$  and  $\Delta y = 1.41 \times 1.41 \text{ mm}^2$ ,  $TR/TE = 142/3 \text{ ms}$ ,  $\Delta t = 90 \text{ }\mu\text{s}$ ,  $T_{read} = 128.88 \text{ ms}$ ,  $BW = 11.1 \text{ kHz}$ ,  $\Delta t_{os} = 10.0 \text{ s}$ .

## 2.6.2 ADC Experiments

The diffusion-weighted MRI experiment utilized a bipolar trapezoidal gradient and was used to demonstrate the ADC-weighted capabilities of *Sectoral* within phantoms. For each  $^{129}Xe$  scan, two magnetization density images using different  $b$ -values (either  $b_0 = 0 \text{ s/cm}^2$  or  $b_i = 13.7 \text{ s/cm}^2$ ) were acquired. This *Sectoral* pulse sequence permitted a direct computation of ADC maps by extracting the pixel-by-pixel ratio of the generated images (using **Eqn. [1.43]**). The *Sectoral* pulse sequence depicted in **Figure 1-15** was used to measure the ADC of the  $^{129}Xe$  gas at a diffusion time of 2.4 ms. To verify that ADC variations are measurable with *Sectoral*, three syringe flow through phantom experiments (1×MB-*Sectoral* and 2×SB-*Sectoral*) were performed. Prior to imaging, the phantom was vacuumed to remove residual air and maximize the MRI signal. A pre-measured volume of  $N_2$  was injected initially to increase the self-diffusion coefficient of the mixture, followed by  $^{129}Xe$  introduced from an isolated Tedlar<sup>®</sup> bag, until the syringe was filled and the bag sealed off with a clamp. The imaging sequence was then initiated using non-selective RF excitations with VFA to obtain 2-D projection images as described above. The *Sectoral* pulse sequence parameters for ADC-mapping were: matrix = 64×64,  $FOV = 90 \times 90 \text{ mm}^2$ ,  $\Delta x$  and  $\Delta y = 1.41 \times 1.41 \text{ mm}^2$ ,  $TR/TE = 134/4.8 \text{ ms}$ ,  $\Delta t = 90 \text{ }\mu\text{s}$ ,  $T_{read} = 128.88 \text{ ms}$ ,  $BW = 11.1 \text{ kHz}$ . A long enough TE was used to provide enough duration for the diffusion gradient pulse to execute. The diffusion gradient waveform



parameters were: diffusion time  $\Delta = 2.4$  ms, lobe duration  $\delta = 2.4$  ms, ramp time  $\tau = 0.4$  ms, and gradient magnitude  $G = 0.603$  mT or 6.03 G.

## 2.7 *In Vivo* MRI Experiments

To collect ventilation images, the previously described 2-D FGRE pulse sequence (section 2.5) and 2-D *Sectoral* pulse sequences (section 2.6) were used. The pulse sequence parameters for FGRE were:  $FOV = 95 \times 95$  mm<sup>2</sup>,  $\Delta x$  and  $\Delta y = 1.49 \times 1.49$  mm<sup>2</sup>,  $TR/TE = 10/4.8$  ms,  $\Delta t = 20$   $\mu$ s,  $T_{read} = 12.80$  ms,  $BW = 50.1$  kHz. For the case of *Sectoral* imaging, the pulse sequence parameters were:  $FOV = 95 \times 95$  mm<sup>2</sup>,  $\Delta x$  and  $\Delta y = 1.49 \times 1.49$  mm<sup>2</sup>,  $TR/TE = 10/3$  ms,  $\Delta t = 90$   $\mu$ s,  $T_{read} = 128.88$  ms,  $BW = 11.1$  kHz.

The *Sectoral* ADC data obtained *in vivo* using the methods described in section 2.7.1 below were correlated with mean linear intercept,  $L_m$ , measurements obtained from lung histological analysis described in section 2.8.

### 2.7.1 ADC Experiments

In total, 9 male Sprague-Dawley rats with no known lung disease were measured. Five of them were used as control animals, while the other four were irradiated. Diffusion MRI data was obtained using MB-*Sectoral* with an embedded bipolar diffusion-sensitizing gradient with two  $b$ -values of 0 and 17.0 s/cm<sup>2</sup>. The diffusion gradient waveform parameters were: diffusion time  $\Delta = 4.8$  ms, lobe duration  $\delta = 4.8$  ms, ramp time  $\tau = 0.8$  ms, and gradient magnitude  $G = 0.301$  mT or 3.01 G. Each sector of  $k$ -space was collected for both  $b$ -value images before stepping to the next sector, in order to reduce signal decay due to  $T_1$  effects and RF consumption during data acquisition.

## 2.8 Histological Analysis

Following animal euthanization, lungs were removed and insufflated using 8.0 ml of liquid formalin and stored in a 10% formalin solution for 48 hours. Paraffin wax was used as an embedding medium for sectioning lung tissue into four slides covering four transverse regions. The lungs were cut into 5.0- $\mu$ m-thick transverse slices that were stained with hematoxylin and eosin (H&E). The stained histological sections were

examined with an Axio Imager A1 microscope (Carl Zeiss MicroImaging, Thornwood, NY) equipped with a digital Retiga EXi 1294 camera (QImaging, Surrey, Canada) linked to a computer with Image-Pro Plus 7.0 software (MediaCybernetics, Bethesda, MD). The mean linear intercept,  $L_m$ , is a stereological metric for quantifying airspace size of the alveoli by measuring the surface area-to-volume ratio.  $L_m$  was calculated for five images at 10× magnification from each of the four slides. The  $L_m$  was measured on a 3×4 grid for each of the images by counting the total intercepts per slide. Further details on histological analysis are provided in **Appendix B**.

## 2.9 Pre-scan Calibrations

Prior to all imaging, calibration procedures were done to improve the accuracy of measurements. RF pulse tip angle was calibrated with continuously flowing xenon. Using FID signals, a 180° tipping angle was found by varying the RF power and pulse width duration, until a minimum signal response was obtained. The 90° tip angle was then determined by reducing the pulse width duration by 50%.

For the case of VFA calibration, the RF pulse was adjusted to equalize the response of the signal intensity for each sector to avoid an undesired asymmetric  $k$ -space weighting. The pulse width,  $\tau_n$ , for each  $n^{\text{th}}$  RF pulse was determined by:

$$\tau_n(\alpha_n) = \tan^{-1} \left( \sqrt{\frac{1}{n} \cdot \frac{180^\circ}{\pi}} \right) \cdot \frac{\tau_{\max}}{90^\circ}, \quad [2.1]$$

where  $\tau_n$  is the pulse width for the  $n^{\text{th}}$  tip angle,  $\alpha_n$ , and  $\tau_{\max}$  is the final pulse width that always resulted in a 90° tip angle (66) (**Table 2-1**). The equation does not include  $T_1$  loss of magnetization because the loss was expected to be negligible for the acquisition parameters used. Each sector calibration step was performed following the delivery of a fresh  $^{129}\text{Xe}$  injection into the phantom or single breath hold with animals. During a gradient encoding strength of 5% of the maximum (0.45 G/cm), the RF pulse amplitude was calibrated by adjusting the power to the RF coil. The calibration steps were repeated until a constant signal response, with  $\pm 5\%$  acceptable variability, was seen over the course of all 16 pulses associated with a sector (**Figure 2-8**).

**Table 2-1:** Representative tip angles with corresponding pulse width, for a series of 16 VFA RF pulses used in SB-*Sectoral*.

RF pulse (n)	Tip angle, $\alpha_n$ ( $^\circ$ )	Pulse width, $\tau_n$ ( $\mu\text{s}$ )
1	14.48	77.21
2	14.96	79.80
3	15.50	82.67
4	16.10	85.88
5	16.78	89.49
6	17.55	93.59
7	18.43	98.32
8	19.47	103.85
9	20.70	110.43
10	22.21	118.44
11	24.09	128.51
12	26.57	141.68
13	30.00	160.00
14	35.26	188.08
15	45.00	240.00
16	90.00	480.00

Resistive gradient shimming and passive shimming were used to optimize the field uniformity of the main magnetic field. To check the quality of the shim, the  $T_2^*$  was quantitatively measured by acquiring a FID (**Figure 2-9**). For imaging, a readout time lower than the  $T_2^*$  ( $T_{\text{read}} < T_2^*$ ) was selected to avoid  $T_2^*$  effects during acquisition.

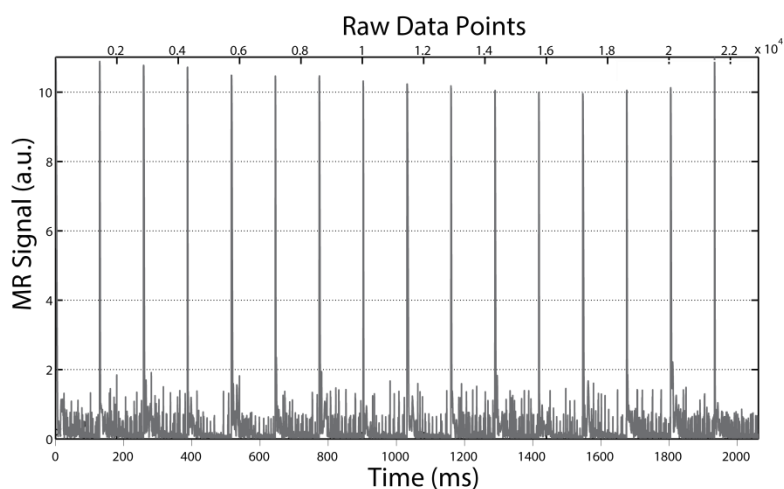


**Figure 2-8:** The VFA calibrated signals from a typical  $^{129}\text{Xe}$  *Sectoral* phantom measurement with appropriate power leading to a constant response with less than 5% variability.

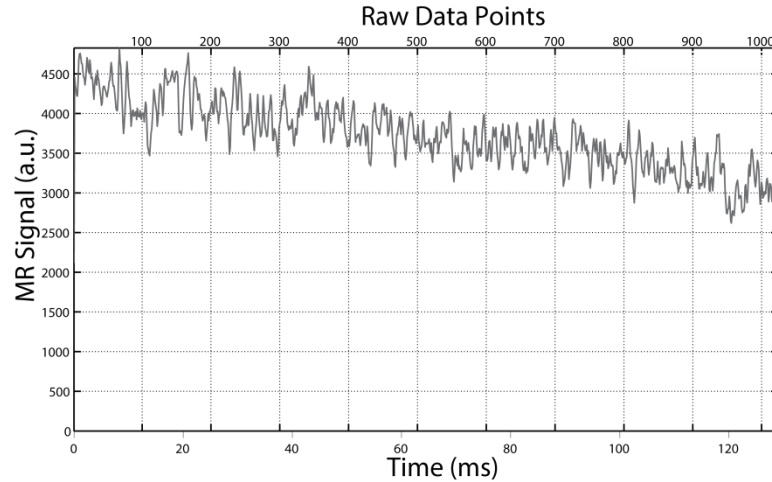


**Figure 2-9:** Representative FID for  $^{129}\text{Xe}$  in a phantom with a measured  $T_2^*$  of 192 ms.  $T_2^*$  was calculated offline in MATLAB with exponential curve fitting.

*Sectoral* waveforms were characterized prior to all imaging in this thesis and the technique is further explained in **Appendix A**.

## 2.10 MRI SNR Efficiency Calculations

To quantify and compare image quality, an SNR efficiency calculation was applied:

$$\chi = \frac{SNR}{(\Delta x \cdot \Delta y) \times \sqrt{t \cdot BW}}, \quad [2.2]$$

where SNR is the signal-to-noise ratio,  $t$  is the total scan time,  $BW$  is the readout bandwidth, and  $\Delta x$  and  $\Delta y$  are  $x$ -axis and  $y$ -axis image resolutions, respectively. The SNR was calculated by dividing the mean signal of a region-of-interest (ROI) measured in the magnitude image (**section 1.6.2.1**) by the standard deviation of a background noise. The standard deviation of background noise was calculated from the magnitude signals in  $k$ -space acquired with an empty RF coil. The receive bandwidth ( $BW$ ) is the reciprocal of the dwell time ( $\Delta t$ ). To calculate resolution (i.e.  $\Delta x$  and  $\Delta y$ ), the field of view (FOV) was divided by the number of pixels in the corresponding direction.

Background noise was also measured in the RF coil, with and without a sample, for both *Sectoral* and FGRE imaging sequences. The ratio of noise obtained with application of magnetic field gradient versus without the application of gradients was 9.0 (all other

imaging parameters held constant) for *Sectoral* and 1.1 for FGRE. To account for these gradient-associated noise differences between *Sectoral* and FGRE, raw SNR and raw SNR efficiency as well as corrected SNR and SNR efficiency were calculated. The correction was made by dividing the background noise by 9.0 for *Sectoral* and 1.1 for FGRE. This correction factor was not required for proton imaging as no additional gradient-induced noise was observed. The origin of the increased gradient-associated noise for *Sectoral* at the  $^{129}\text{Xe}$  frequency (0.883 MHz) compared to proton (3.163 MHz) will be discussed further in **Chapter 4**.

## 2.11 Data Processing and Analysis

Following acquisition, all raw  $k$ -space data sampled were processed and analyzed offline using routines coded in MATLAB (The MathWorks, Natick, MA). The  $k$ -space data were phase and baseline corrected before being ordered and zero-filled. An inverse-Fourier transform was applied to the corrected  $k$ -space to reconstruct a  $^{129}\text{Xe}$  magnetization-density image. For SNR calculations, a MATLAB script was coded to allow the user to select and drag a series of ROI's in real time. The mean signal intensities were calculated from user-defined ROI's drawn on the magnitude images. A single user-defined ROI estimated the standard-deviation of background noise. For each image series, an ROI of  $5\times 5$  pixels was used for signal intensity and an ROI of  $15\times 15$  pixels was used for noise. For the case of  $T_1$ , ADC and  $T_2^*$  mapping, a pair of images were reconstructed corresponding to appropriately weighted and un-weighted images. A signal mask was computed using the normal un-weighted image to separate the pixels used for subsequent processing. The mask was then used to mask out the background of the weighted image. A pixel-by-pixel linear data fitting routine in MATLAB was used along with **Eqns. [1.37]** and **[1.43]** to generate maps of  $T_1$ , and ADC, respectively.

### 2.11.1 $T_1$ and $p_A\text{O}_2$ Mapping

The two  $T_1$ -based images obtained using the  $T_1$  *Sectoral* sequence with an oxygen-sensitization time delay of 10 s were first converted to a  $T_1$  map using **Eqn. [1.37]**. A  $B_1$  map was calculated using **Eqn. [1.34]** for  $B_1$  correction of each  $T_1$  map. Each pixel was then converted to the corresponding  $p_A\text{O}_2$  values using **Eqn. [1.39]**, where the relaxivity

of  $^{129}\text{Xe}$  due to the presence of  $\text{O}_2$  was taken to be:  $\kappa = 4.3 \text{ atm}^{-1} \text{ s}^{-1}$  (53). The mean and standard deviation of the  $T_1$  and  $p_{\text{A}}\text{O}_2$  values from the ROI were calculated using MATLAB functions (mean2.m) and (std2.m). A histogram (hist.m) of the ROI was also used to obtain mean  $T_1$  and  $p_{\text{A}}\text{O}_2$  values and repeatedly showed the same mean values. The histograms of  $T_1$ 's and  $p_{\text{A}}\text{O}_2$ 's were fit by a normal Gaussian distribution (histfit.m) to calculate their full width at half maximum (FWHM). Data are presented as global mean  $\pm$  standard deviation, with FWHM to the next right column, of  $T_1$  or  $p_{\text{A}}\text{O}_2$  from the ROI (i.e. whole syringe).

### 2.11.2 ADC Mapping

The two ADC-based images obtained using the diffusion-weighted *Sectoral* sequence with different  $b$ -values (0 and  $13.7 \text{ s/cm}^2$  for *in vitro* and 0 and  $17.0 \text{ s/cm}^2$  for *in vivo*) were used to generate an ADC map using **Eqn. [1.43]**. The mean and standard deviation of the ADC values from the ROI were calculated using MATLAB functions (mean2.m) and (std2.m). A histogram (hist.m) of the ROI was also used to obtain *mean* ADC values and repeatedly showed the same mean values. The histogram of ADC's was fit by a normal Gaussian distribution (histfit.m) to calculate the FWHM. Data are presented as global mean  $\pm$  standard deviation, with FWHM to the next right column, of ADC from the ROI (i.e. whole syringe).

## 2.12 *In vivo* Statistical Analysis

To compare *Sectoral* diffusion MRI between the healthy and irradiated rat cohorts, the FWHM, which was calculated from the Gaussian distribution of each lung ADC histogram, was obtained. The FWHM ADC was then correlated using a nonparametric Mann-Whitney U-test, employed with a two-tailed 95% confidence interval, where at the  $p < 0.05$  level the differences of the population means are significantly different. To analyze if *Sectoral* diffusivity MRI correlated well with histological measurements, the global *mean* ADC of  $^{129}\text{Xe}$  was calculated and compared with  $L_m$  of that lung. A linear regression fit with 95% confidence band of the best-fit line with residual plot with significance at  $p < 0.05$  was applied. Data are presented as global ADC mean  $\pm$  standard deviation of ADC in the ROI (i.e. whole lung).



## Chapter 3: Results

### 3 Introduction

This chapter presents the results from the techniques described in **Chapter 2**. Fast Gradient Recalled Echo (FGRE) and *Sectoral* MRI approaches are compared on the basis of SNR efficiency using a resolution phantom. The feasibility of producing *Sectoral* maps of apparent diffusion coefficients (ADC), longitudinal relaxation time ( $T_1$ ), and alveolar partial pressure of oxygen ( $p_{AO_2}$ ) from a syringe phantom filled with either a  $^{129}\text{Xe-N}_2$  or  $^{129}\text{Xe-O}_2$  mixture is also demonstrated. Ventilation images of rat lungs are also shown to demonstrate the feasibility of the *Sectoral* sequence *in vivo*. The chapter concludes by presenting ADC maps and histological analysis from a pilot study that investigated the potential of the *Sectoral* sequence to detect changes associated with RILI.

#### 3.1 *In Vitro*

##### 3.1.1 FGRE versus *Sectoral* Proton Imaging

Representative proton resolution phantom FGRE and *Sectoral* images are shown in **Figure 3-1**, confirming that both sequences can be used for reliable  $^1\text{H}$  imaging. Although there is some image blurring due to unavoidable resistive magnet off-resonance effects and  $\vec{B}_0$  non-uniformity, it can be seen that both proton phantom images show good correspondence with each other as well as the expected geometry and dimensions in **Figure 2-1**. The corresponding SNR efficiency calculations extracted from the resulting images are summarized in **Table 3-1**, along with other factors.



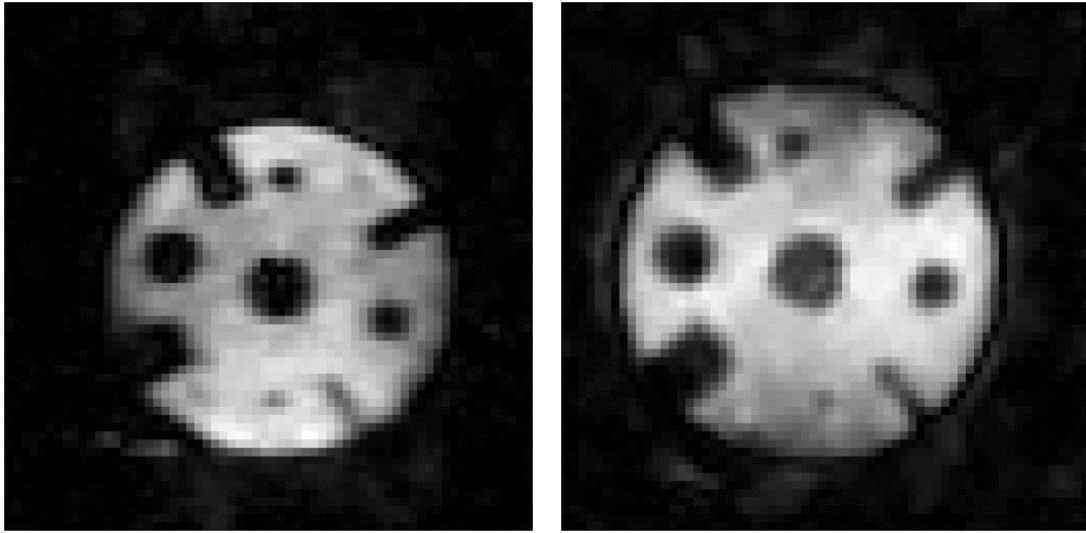


**Figure 3-1:**  $^1\text{H}$  resolution phantom images acquired with the FGRE (left) and SB-*Sectoral* (right) sequence.

**Table 3-1:** Summary of  $^1\text{H}$  resolution phantom imaging results.

	FGRE $^1\text{H}$	SB- <i>Sectoral</i> $^1\text{H}$
<b>Resolution (mm<sup>2</sup>)</b>	1.17	1.11
<b>FOV (mm<sup>2</sup>)</b>	75×75	71×71
<b>BW (kHz)</b>	50.0	28.5
<b>Scan Time (s)</b>	39.2	10.4
<b>Mean Signal</b>	1.56e+07	2.94e+06
$\sigma_{\text{air}}$	5.99e+04	1.04e+04
<b>SNR</b>	260.4	282.7
<b>SNR Efficiency</b>	4.3	13.4

### 3.1.2 FGRE versus *Sectoral* $^{129}\text{Xe}$ Imaging

**Figure 3-2** shows representative spin density images of the flow-through syringe phantom filled with hyperpolarized  $^{129}\text{Xe}$  using FGRE, SB-*Sectoral*, and MB-*Sectoral*. The results for the  $^{129}\text{Xe}$  syringe phantom measurements are summarized in **Table 3-2**.

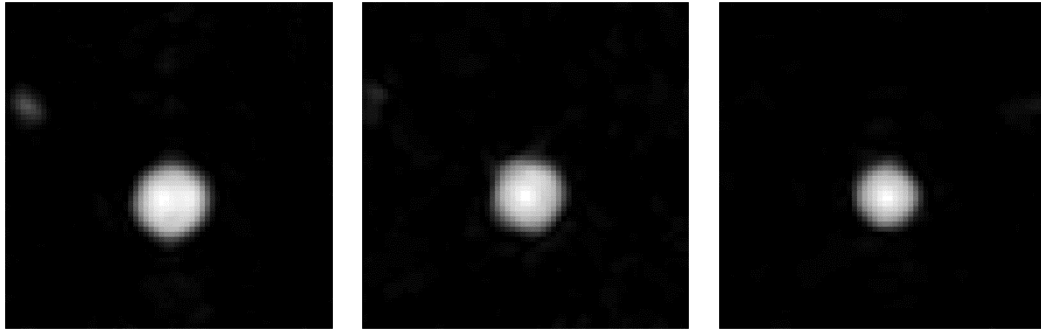


**Figure 3-2:**  $^{129}\text{Xe}$  flow-through syringe phantom images acquired with the FGRE (left), SB-*Sectoral* (middle), and MB-*Sectoral* (right) sequences.

**Table 3-2:** Summary of  $^{129}\text{Xe}$  syringe phantom imaging results.

	FGRE $^{129}\text{Xe}$	SB- <i>Sectoral</i> $^{129}\text{Xe}$	MB- <i>Sectoral</i> $^{129}\text{Xe}$
<b>Breath holds</b>	1	1	16
<b>Resolution (mm<sup>2</sup>)</b>	1.33	1.47	1.50
<b>FOV (mm<sup>2</sup>)</b>	85×85	94×94	96×96
<b>BW (kHz)</b>	50.0	11.1	11.1
<b>Scan Time (s)</b>	1.5	2.2	2.2
<b>Mean Signal</b>	2.05e+06	3.73e+06	1.85e+07
$\sigma_{\text{air}}$	4.79e+04	6.10e+04	6.33e+04
$\sigma_{\text{air}}$ (Corrected)	4.35e+04	6.78e+03	7.03e+03
<b>SNR</b>	42.8	61.1	292.3
<b>SNR (Corrected)</b>	47.1	550.1	2631.6
<b>SNR Efficiency</b>	2.8	5.8	26.1
<b>SNR Efficiency (Corrected)</b>	3.1	51.8	235.3

### 3.1.3 Sectoral ADC Measurements

**Figure 3-3** (pure  $^{129}\text{Xe}$ ) and **Figure 3-4** ( $^{129}\text{Xe}$ -N<sub>2</sub> mixture) show representative normal un-weighted and ADC-weighted images with a corresponding ADC map from the MB-*Sectoral* experiment. The pure  $^{129}\text{Xe}$  results of **Figure 3-3** show a narrow distribution of ADC values across the phantom, indicating uniformity. When N<sub>2</sub> is mixed with  $^{129}\text{Xe}$  the distribution of ADC values across the phantom broadens, as shown in **Figure 3-4**. Five measurements in total, with 16 gas insertions per  $k$ -space sector, were performed in the MB-*Sectoral* experiment. Similarly, seven measurements in total, with 1 gas insertion per  $k$ -space sector, were performed in two SB-*Sectoral* experiments. All syringe phantom diffusion-weighted experiments are summarized in **Table 3-3**. The mean and standard deviation of the calculated ADC values from the ROI of each map, with corresponding

FWHM values determined from the Gaussian distribution of each ADC histogram, are reported. In all three experiments, the *mean* ADC and FWHM ADC values increased with higher concentration of N<sub>2</sub>. The increase in FWHM arises with greater heterogeneity of ADC values throughout the syringe phantom, resulting in a broader spectrum. The mean and reciprocal ADC values acquired using the MB-*Sectoral* approach from the various prepared N<sub>2</sub> volume concentration phantoms are shown in **Figure 3-5** (left) and **Figure 3-5** (right), respectively. **Figure 3-6** shows the mean (top) and reciprocal (bottom) ADC values acquired using the SB-*Sectoral* approach, in two different experiments (left and right, respectively), from seven measurements with various N<sub>2</sub> volume concentrations in the syringe phantoms.

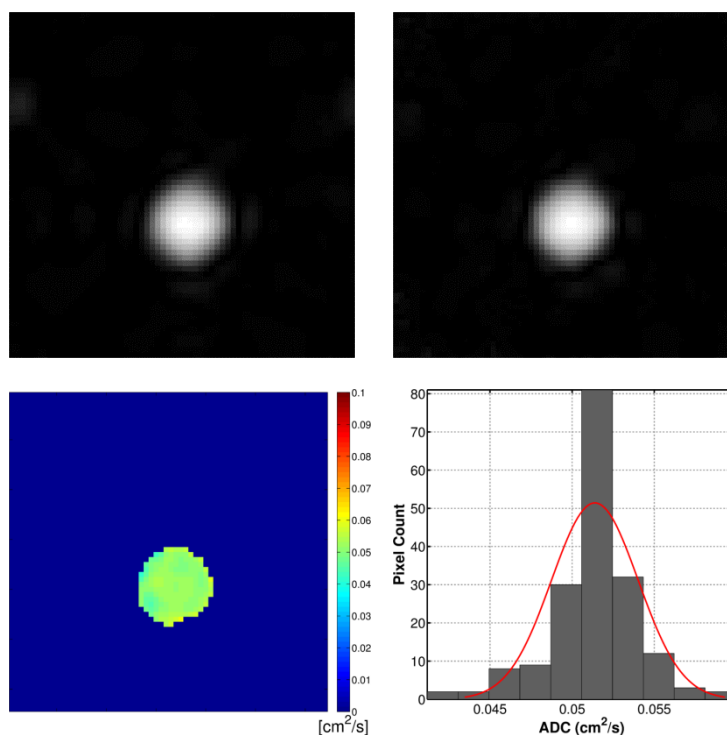


**Figure 3-3:** Representative diffusion-weighted MB-*Sectoral* <sup>129</sup>Xe phantom results filled with pure <sup>129</sup>Xe. Shown are: un-weighted image (top-left), diffusion-weighted image (top-right), corresponding ADC-map (bottom-left) and histogram (bottom-right). *Mean* ADC =  $0.051 \pm 0.003$  cm<sup>2</sup>/s and FWHM ADC =  $0.008$  cm<sup>2</sup>/s.

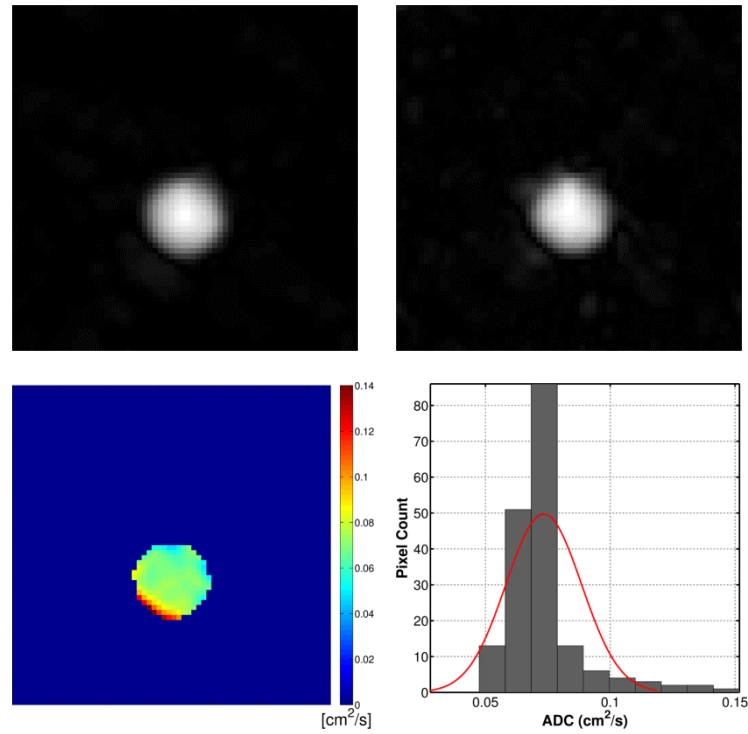


**Figure 3-4:** Representative diffusion-weighted MB-Sectoral  $^{129}\text{Xe}$  phantom results with 6.4 ml of  $\text{N}_2$  added. Shown are: un-weighted image (top-left), diffusion-weighted image (top-right), corresponding ADC-map (bottom-left) and histogram (bottom-right). *Mean* ADC =  $0.073 \pm 0.015 \text{ cm}^2/\text{s}$  and *FWHM* ADC =  $0.037 \text{ cm}^2/\text{s}$ .

**Table 3-3:** Mean and standard deviation of ADC values with corresponding FWHM ADC values obtained from the Gaussian distribution of each ADC histogram, for each ADC map. Data reported were obtained from  $^{129}\text{Xe}$ - $\text{N}_2$  mixture filled syringe using MB-Sectoral and two SB-Sectoral trials.

Added $\text{N}_2$ (ml)	MB-Sectoral ADC ( $\text{cm}^2/\text{s}$ )	FWHM ( $\text{cm}^2/\text{s}$ )	SB-Sectoral 1 ADC ( $\text{cm}^2/\text{s}$ )	FWHM ( $\text{cm}^2/\text{s}$ )	SB-Sectoral 2 ADC ( $\text{cm}^2/\text{s}$ )	FWHM ( $\text{cm}^2/\text{s}$ )
<b>0</b>	$0.051 \pm 0.003$	0.008	$0.056 \pm 0.008$	0.018	$0.057 \pm 0.006$	0.014
<b><math>0.8 \pm 0.2</math></b>	-	-	$0.058 \pm 0.011$	0.027	$0.057 \pm 0.007$	0.016
<b><math>1.6 \pm 0.2</math></b>	$0.051 \pm 0.006$	0.016	$0.058 \pm 0.010$	0.023	$0.061 \pm 0.010$	0.025
<b><math>2.4 \pm 0.2</math></b>	-	-	$0.059 \pm 0.009$	0.020	$0.058 \pm 0.010$	0.023
<b><math>3.2 \pm 0.2</math></b>	$0.053 \pm 0.008$	0.019	$0.066 \pm 0.016$	0.038	$0.063 \pm 0.016$	0.038
<b><math>4.0 \pm 0.2</math></b>	-	-	$0.073 \pm 0.018$	0.042	$0.067 \pm 0.013$	0.030
<b><math>4.8 \pm 0.2</math></b>	$0.061 \pm 0.004$	0.010	$0.075 \pm 0.019$	0.045	$0.073 \pm 0.021$	0.049
<b><math>5.6 \pm 0.2</math></b>	-	-	-	-	-	-
<b><math>6.4 \pm 0.2</math></b>	$0.073 \pm 0.015$	0.037	-	-	-	-

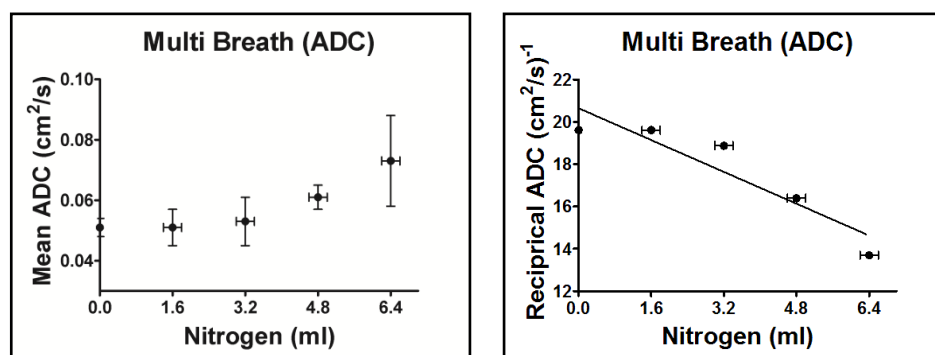


**Figure 3-5:** Results of the phantom experiments using MB-Sectoral. Plots of ADC pixel average versus prepared N<sub>2</sub> volume for five scans (left). The vertical error bars represent the pixel deviation in each map represented from the ROI. The horizontal error bars correspond to the precision of the prepared N<sub>2</sub> volumes ( $\pm 0.2$  ml) in the syringe. Reciprocals of *mean* ADC values (right) with significant ( $p < 0.05$ ) linear regression fit. Calculated  $p = 0.024$  and  $r^2 = 0.86$ .

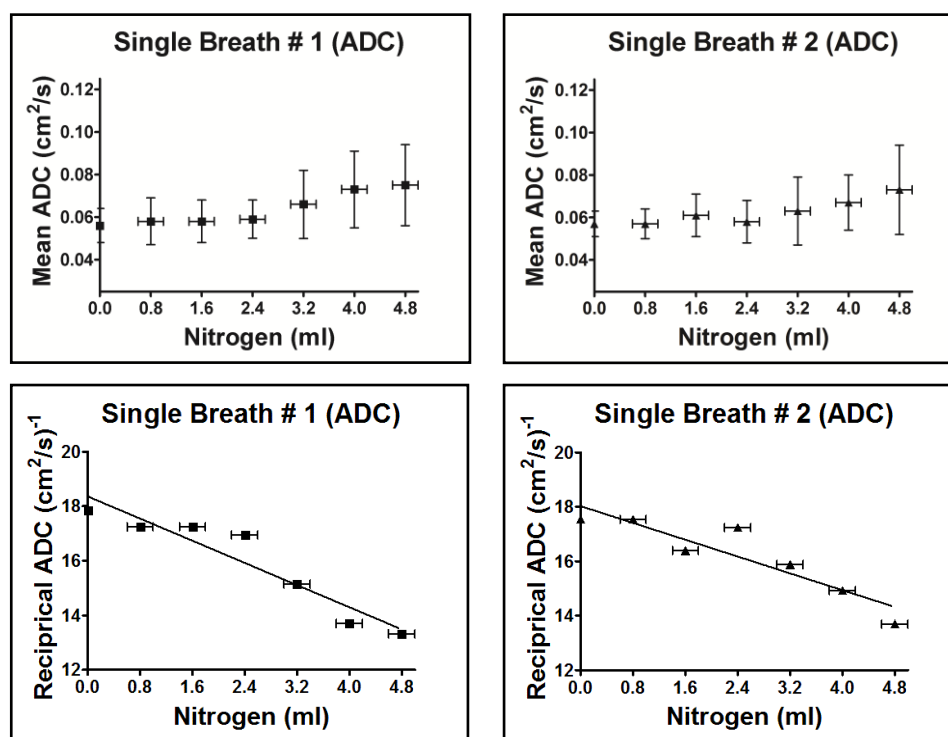


**Figure 3-6:** Results of the two phantom experiments using SB-Sectoral. Plots of ADC pixel average versus prepared N<sub>2</sub> volume for seven scans (top row). The vertical error bars represent the pixel deviation in each map represented from the ROI. The horizontal error bars correspond to the precision of the prepared N<sub>2</sub> volumes ( $\pm 0.2$  ml) in the syringe. Reciprocals of *mean* ADC values (bottom row) with significant ( $p < 0.05$ ) linear regression fit. For experiment 1,  $p = 0.001$  and  $r^2 = 0.90$  and experiment 2,  $p = 0.004$  and  $r^2 = 0.84$ .

### 3.1.4 Sectoral $T_1$ and $p_{A}O_2$ Measurements

**Figure 3-7** shows an example of a calculated transmit RF magnetic field ( $B_1$ ) map (middle) resolved from a  $T_1$  map (left), and used to calculate a  $B_1$  corrected  $T_1$  map (right). **Figure 3-8** (pure  $^{129}\text{Xe}$ ) and **Figure 3-9** ( $^{129}\text{Xe}$ - $O_2$  mixture) shows a representative normal un-weighted and  $T_1$ -weighted image with corresponding  $T_1$  and  $p_{A}O_2$  maps from the MB-Sectoral experiment. The pure  $^{129}\text{Xe}$  results of **Figure 3-8** show a narrow distribution of  $T_1$  values across the phantom, demonstrating a homogenous distribution of  $T_1$  and  $p_{A}O_2$  values as expected.

A total of four measurements, with 16 gas insertions per  $k$ -space sector, were performed in the MB-Sectoral experiment. Similarly, a total of five measurements in total, with 1 gas insertion per  $k$ -space sector, was performed in two SB-Sectoral experiments. The mean  $T_1$  and corresponding  $p_{A}O_2$  measurements for all syringe phantom  $T_1$ -weighted experiments are summarized in **Table 3-4** and **Table 3-5**, respectively. The standard deviation of the calculated  $T_1$  and  $p_{A}O_2$  values from the ROI of each map, with corresponding FWHM values determined from the Gaussian distribution of each histogram, are also reported. As expected, the addition of  $O_2$  to the  $^{129}\text{Xe}$  causes a decrease in the global  $T_1$  and increase in the  $p_{A}O_2$  across the phantom, as shown in **Figure 3-9**. Furthermore, the FWHM  $T_1$  decrease and FWHM  $p_{A}O_2$  increase with added  $O_2$ .

The mean  $T_1$  and  $p_{A}O_2$  with corresponding standard deviations from the prepared  $O_2$  volume concentrations in the phantoms are shown in **Figure 3-10**. **Figure 3-11** shows the mean  $T_1$  (top) values and  $p_{A}O_2$  (bottom) acquired using the SB-Sectoral approach, in two different experiments (left and right, respectively), from five measurements with varied  $O_2$  volume concentrations in the syringe phantoms. In all three experiments, the values for mean and standard deviation of  $T_1$  and corresponding FWHM  $T_1$  decrease linearly with higher concentration of  $O_2$ . However, the  $T_1$  of the first measurements in all three experiments shows a much greater mean of  $T_1$  compared to the other measurements, suggesting that the  $\Delta t_{os}$  was too short to induce significant  $T_1$ -weighting, as indicated by the large standard deviation. The mean and standard deviation of  $p_{A}O_2$  values and

corresponding FWHM increase linearly with added  $O_2$ , showing agreement with the significant ( $p < 0.05$ ) linear regression plots in **Figure 3-10** and **Figure 3-11**.

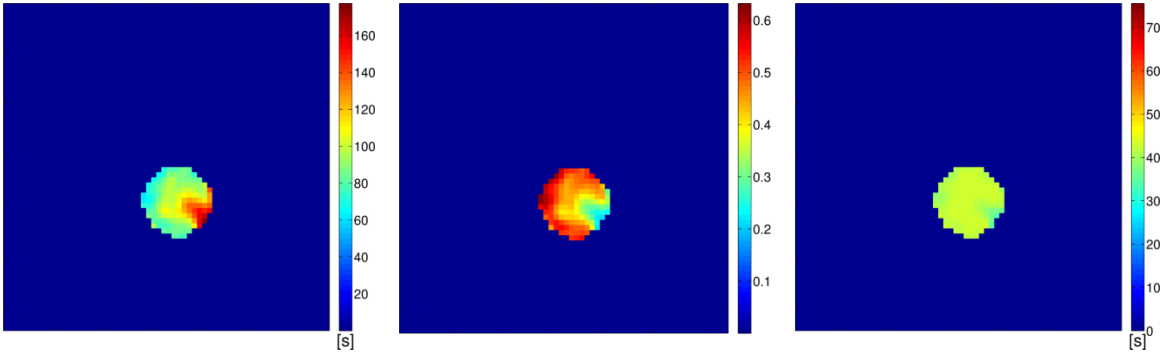


**Figure 3-7:** Representative *Sectoral*  $T_1$ -maps before (left) and after (right)  $B_1$  correction using a  $B_1$  map (middle).

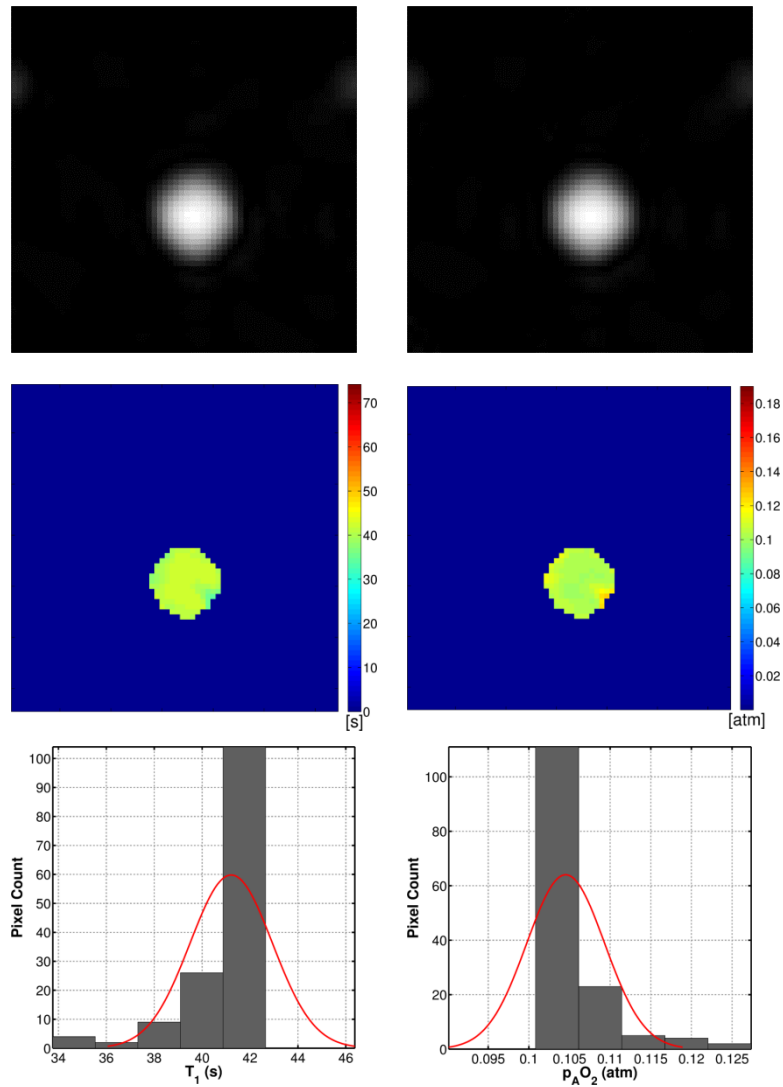


**Figure 3-8:** Representative  $T_1$ -weighted MB-Sectoral  $^{129}\text{Xe}$  phantom experiment filled with pure  $^{129}\text{Xe}$ . Un-weighted image (top-left),  $T_1$ -weighted image (top-right), corresponding  $T_1$ -map (middle-left) & histogram (bottom-left), and the corresponding  $p_{\text{A}}\text{O}_2$ -map (middle-right) & histogram (bottom-right). Mean  $T_1 = 41.21 \pm 1.72$  s, FWHM  $T_1 = 4.05$  s, mean  $p_{\text{A}}\text{O}_2 = 0.0057 \pm 0.003$  atm, and FWHM  $p_{\text{A}}\text{O}_2 = 0.0006$  atm.

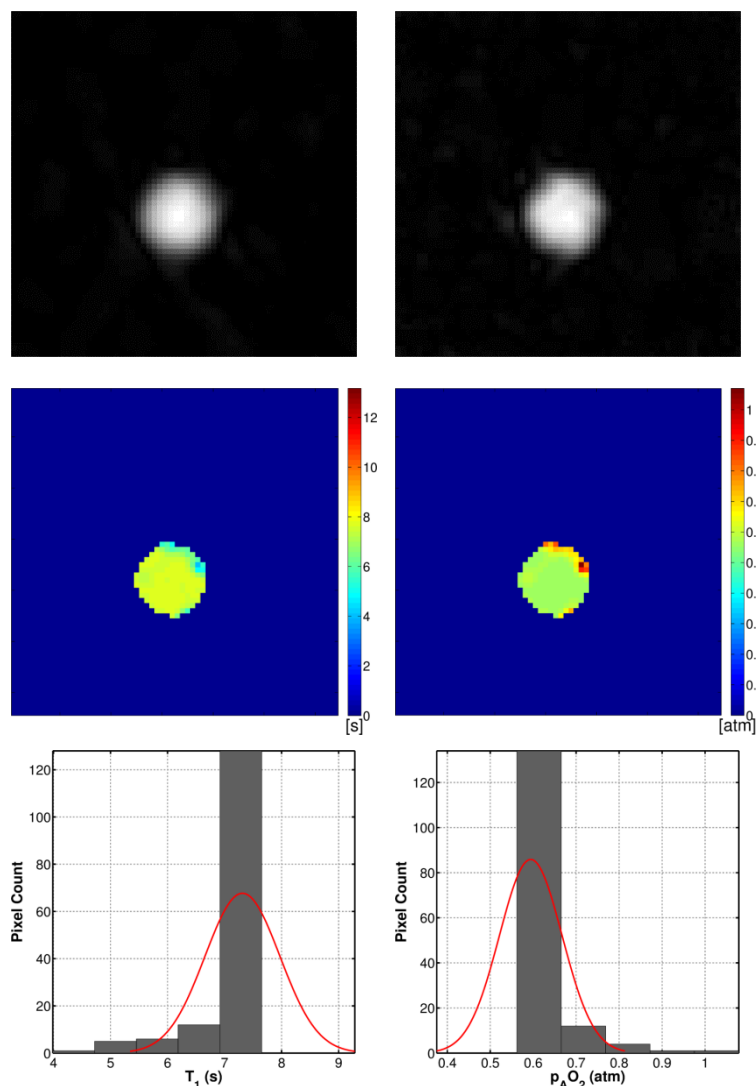


**Figure 3-9:** Representative  $T_1$ -weighted MB-Sectoral  $^{129}\text{Xe}$  phantom experiment with 2.4 ml of  $\text{O}_2$  added. Un-weighted image (top-left),  $T_1$ -weighted image (top-right), corresponding  $T_1$ -map (middle-left) & histogram (bottom-left), and the corresponding  $p_{\text{A}}\text{O}_2$ -map (middle-right) & histogram (bottom-right). Mean  $T_1 = 7.31 \pm 0.66$  s, FWHM  $T_1 = 1.55$  s, mean  $p_{\text{A}}\text{O}_2 = 0.0321 \pm 0.004$  atm, and FWHM  $p_{\text{A}}\text{O}_2 = 0.0092$  atm.



**Table 3-4:** Mean and standard deviation of  $T_1$  values with corresponding FWHM ADC values obtained from the Gaussian distribution of each  $T_1$  histogram, for each  $T_1$  map. Data reported were obtained from  $^{129}\text{Xe-O}_2$  mixture filled syringe using *MB-Sectoral* and two *SB-Sectoral* trials.

Added $\text{O}_2$ (ml)	<i>MB-Sectoral</i> $T_1$ (s)	FWHM ( $\text{cm}^2/\text{s}$ )	<i>SB-Sectoral 1</i> $T_1$ (s)	FWHM ( $\text{cm}^2/\text{s}$ )	<i>SB-Sectoral 2</i> $T_1$ (s)	FWHM ( $\text{cm}^2/\text{s}$ )
0	$41.21 \pm 1.72$	4.05	$53.04 \pm 17.95$	42.27	$61.158 \pm 20.45$	48.16
$0.8 \pm 0.2$	$22.26 \pm 1.79$	4.21	$13.69 \pm 0.49$	1.14	$16.87 \pm 1.02$	2.41
$1.6 \pm 0.2$	$10.65 \pm 0.78$	1.83	$8.37 \pm 0.60$	1.42	$8.49 \pm 0.79$	1.87
$2.4 \pm 0.2$	$7.31 \pm 0.66$	1.55	$7.61 \pm 0.58$	1.37	$6.24 \pm 0.40$	0.94
$3.2 \pm 0.2$	-	-	$5.72 \pm 1.55$	3.67	$5.22 \pm 1.18$	2.78

**Table 3-5:** Mean and standard deviation of  $p_{\text{A}}\text{O}_2$  values with corresponding FWHM ADC values obtained from the Gaussian distribution of each  $p_{\text{A}}\text{O}_2$  histogram, for each  $p_{\text{A}}\text{O}_2$  map. Data reported were obtained from  $^{129}\text{Xe-O}_2$  mixture filled syringe using *MB-Sectoral* and two *SB-Sectoral* trials.

Added $\text{O}_2$ (ml)	<i>MB-Sectoral</i> $p_{\text{A}}\text{O}_2$ (atm)	FWHM ( $\text{cm}^2/\text{s}$ )	<i>SB-Sectoral 1</i> $p_{\text{A}}\text{O}_2$ (atm)	FWHM ( $\text{cm}^2/\text{s}$ )	<i>SB-Sectoral 2</i> $p_{\text{A}}\text{O}_2$ (atm)	FWHM ( $\text{cm}^2/\text{s}$ )
0	$0.0057 \pm 0.003$	0.0006	$0.0047 \pm 0.001$	0.0026	$0.0042 \pm 0.001$	0.0028
$0.8 \pm 0.2$	$0.0105 \pm 0.001$	0.0022	$0.0170 \pm 0.001$	0.0016	$0.0138 \pm 0.001$	0.0020
$1.6 \pm 0.2$	$0.0220 \pm 0.003$	0.0069	$0.0280 \pm 0.005$	0.0113	$0.0279 \pm 0.006$	0.0142
$2.4 \pm 0.2$	$0.0321 \pm 0.004$	0.0092	$0.0307 \pm 0.002$	0.0054	$0.0375 \pm 0.003$	0.0059
$3.2 \pm 0.2$	-	-	$0.0439 \pm 0.014$	0.0326	$0.0471 \pm 0.012$	0.0288

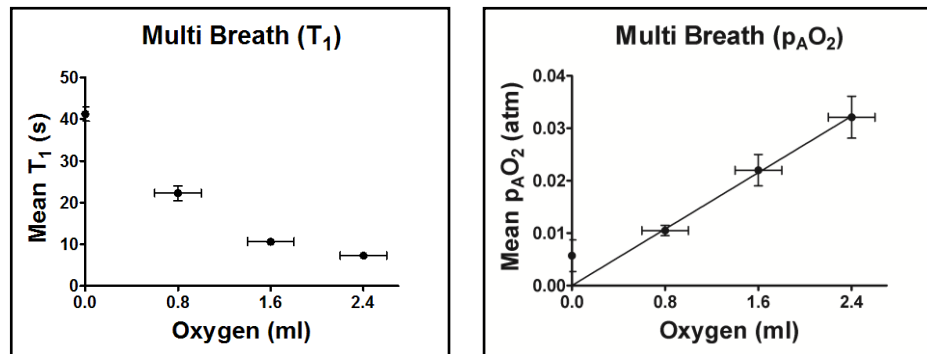


**Figure 3-10:** Results of the phantom experiments using *MB-Sectoral*. Plots of  $T_1$  (left) and corresponding  $p_{\text{A}}\text{O}_2$  (right) pixel average versus prepared  $\text{O}_2$  volume for four scans. The vertical error bars represent the pixel deviation in each map represented from the ROI. The horizontal error bars correspond to the precision of the prepared  $\text{O}_2$  volumes. The solid line shows the expected results. The solid line shows a significant ( $p < 0.05$ ) linear regression fit of  $p_{\text{A}}\text{O}_2$  values. Calculated  $p = 0.01$  and  $r^2 = 0.98$ .

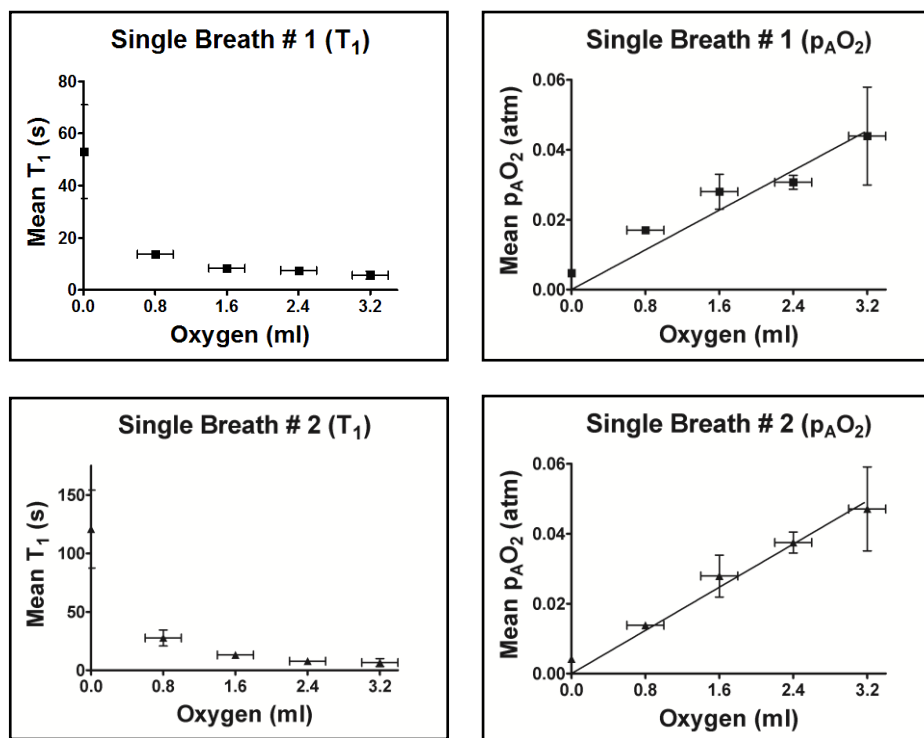


**Figure 3-11:** Results of the two phantom experiments using SB-Sectoral. Plots of  $T_1$  (top-row) and corresponding  $p_AO_2$  (bottom-row) pixel average versus prepared  $O_2$  volume for five scans. The vertical error bars represent the pixel deviation in each map represented from the ROI. The horizontal error bars correspond to the precision of the prepared  $O_2$  volumes. The solid line shows a significant ( $p < 0.05$ ) linear regression fit of  $p_AO_2$  values. For experiment 1,  $p = 0.001$  and  $r^2 = 0.98$  and experiment 2,  $p = 0.0002$  and  $r^2 = 0.99$ .

## 3.2 *In Vivo*

### 3.2.1 FGRE and *Sectoral* $^{129}\text{Xe}$ Imaging

**Figure 3-12** shows a representative whole lung 2-D projection image in coronal (middle) and axial (right) views obtained with *MB-Sectoral* with  $^{129}\text{Xe}$ . The coronal and axial images were obtained in separate *Sectoral* measurements. A photograph of an excised rat lung is also shown (**Figure 3-12**, left) for comparison, indicating the various lobes. **Figure 3-13** shows representative coronal images using  $^{129}\text{Xe}$  from the same rat following a single breath with FGRE (left), *SB-Sectoral* (middle), and with *MB-Sectoral* (right). **Table 3-6** summarizes the whole-lung results, in particular SNR efficiency calculations, measured from the resulting images obtained using the three sequences.

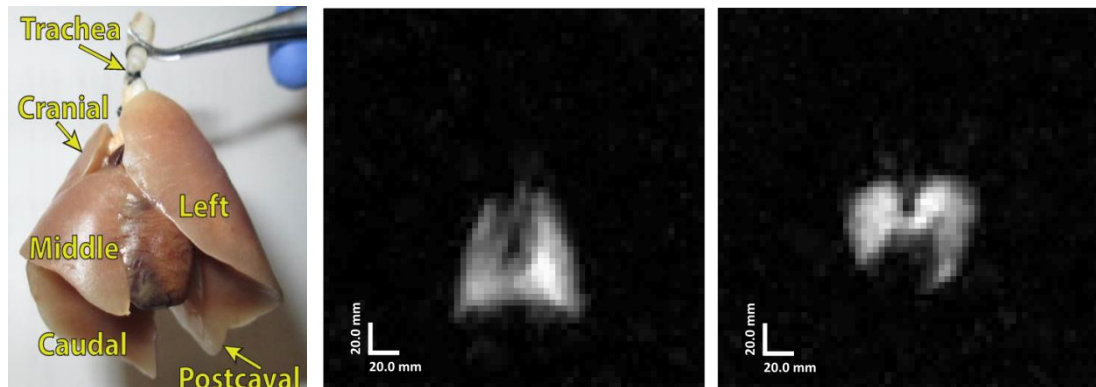


**Figure 3-12:** Photograph of a rat lung (left). Representative *MB-Sectoral* 2-D whole-lung projection image of a rat lung in coronal view (middle) and axial view (right) obtained at low field with  $^{129}\text{Xe}$ . FOV =  $112 \times 112 \text{ mm}^2$ .

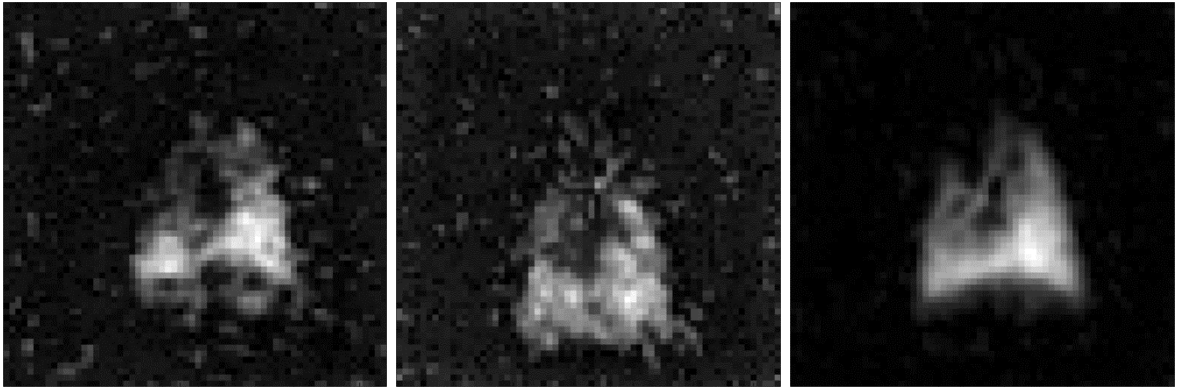


**Figure 3-13:** 2-D coronal *in vivo*  $^{129}\text{Xe}$  rat lung MRI obtained at low field with: FGRE (left), SB-*Sectoral* (middle), and MB-*Sectoral* (right). FGRE and SB-*Sectoral* used 1 breath hold and MB-*Sectoral* used 16 breath holds.

**Table 3-6:** *In vivo* comparison using the different sequences.

	FGRE	SB- <i>Sectoral</i>	MB- <i>Sectoral</i>
<b>Breath holds</b>	1	1	16
<b>Resolution (mm<sup>2</sup>)</b>	1.49	1.49	1.49
<b>FOV (mm<sup>2</sup>)</b>	95×95	95×95	95×95
<b>BW (kHz)</b>	50.1	11.1	11.1
<b>Scan Time (s)</b>	1.5	2.2	2.2
<b>Mean Signal</b>	1.87e+05	2.36e+05	1.35e+06
<b><math>\sigma_{\text{air}}</math></b>	4.79e+04	6.09e+04	6.33e+04
<b><math>\sigma_{\text{air}}</math> (Corrected)</b>	4.35e+04	6.78e+03	7.03e+03
<b>SNR</b>	3.90	3.87	21.33
<b>SNR (Corrected)</b>	4.30	8.98	192.03

### 3.2.2 Sectoral ADC Measurements of RILI

**Figure 3-14** (top) shows representative *Sectoral*  $^{129}\text{Xe}$  ADC maps, with corresponding histograms (bottom), at baseline (left) and 2-weeks post-irradiation (right) for rat lungs from the healthy and irradiated cohorts. The irradiated rat (**Figure 3-14**, right) has greater apparent heterogeneity than the healthy rat (**Figure 3-14**, left), presumably, due to the differences in tissue damage occurring from radiation treatment. It was observed that the SNR for the *Sectoral*  $^{129}\text{Xe}$  lung images varied from rat to rat, presumably, due to differences in gas polarization and lung heterogeneity. **Table 3-7** shows histological (i.e.  $L_m$ ) and MRI data (i.e. ADC) collected from each rat. Each rat is classified as either healthy or irradiated and includes the rat number.

**Figure 3-15** demonstrates differences in  $^{129}\text{Xe}$  diffusivity between healthy and irradiated rats using FWHM ADC. A two-tailed (Mann Whitney) unpaired t-test revealed a statistically significant ( $p = 0.0317$ ) difference between the healthy and two-week irradiated groups. A linear regression fit with 95% confidence band of the best-fit line and residual plot with statistical significance between  $L_m$  and *mean* ADC ( $p = 0.0061$ ,  $r^2 = 0.7408$ ) is shown in **Figure 3-16** after excluding the outlier observation. These correlations do not show a clear separation of healthy and irradiated mean ADC. Some irradiated rats appear to have high ADC, indicating no inflammation response. The reverse is also observed for some healthy rats, which have low ADC, in particular the outlier.

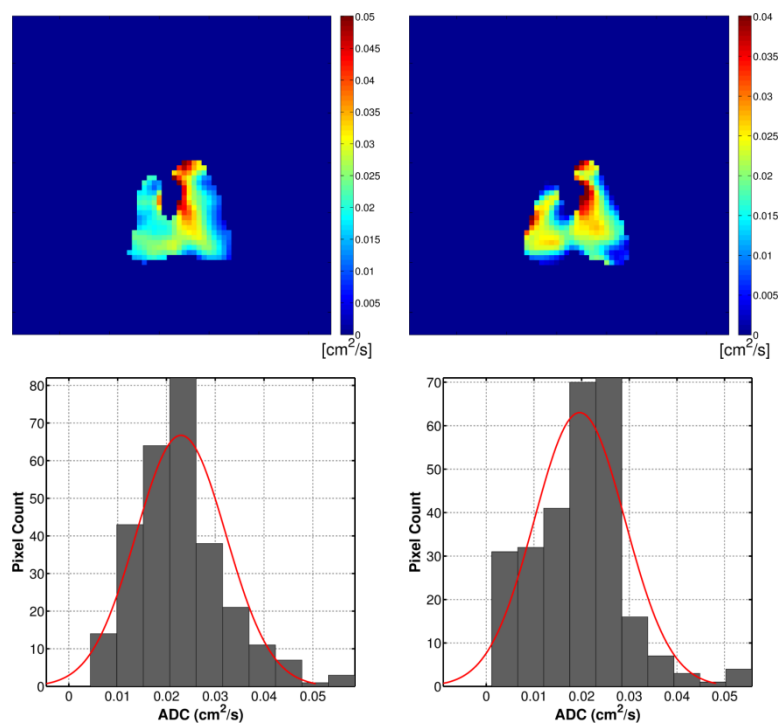


**Figure 3-14:** Representative rat lung ADC-maps for healthy (top-left) with corresponding histogram (bottom-left) and irradiated (top-right) with corresponding histogram (bottom-right). The mean and standard deviation of ADC values, with corresponding FWHM ADC values obtained from the Gaussian distribution of each ADC histogram, for each ADC map of all rat lungs can be found in **Table 3-7**.

**Table 3-7:** *In vivo* mean of ADC values, FWHM ADC values, and  $L_m$  from histological analysis.

N	Cohort	$L_m$ ( $\mu\text{m}$ )	ADC ( $\text{cm}^2/\text{s}$ )	ADC FWHM ( $\text{cm}^2/\text{s}$ )
1	Irradiated	$56.3 \pm 8.8$	$0.028 \pm 0.010$	0.024
2	Healthy	$44.8 \pm 5.9$	$0.017 \pm 0.007$	0.018
3	Healthy	$58.3 \pm 6.8$	$0.024 \pm 0.008$	0.019
4	Irradiated	$47.0 \pm 3.6$	$0.020 \pm 0.010$	0.022
5	Irradiated	$55.0 \pm 1.8$	$0.024 \pm 0.011$	0.025
6	Healthy	$50.0 \pm 2.4$	$0.023 \pm 0.009$	0.022
7	Healthy	$52.5 \pm 1.3$	$0.021 \pm 0.008$	0.018
8	Healthy	$57.5 \pm 3.1$	$0.019 \pm 0.010$	0.023
9	Irradiated	$59.5 \pm 6.8$	$0.026 \pm 0.012$	0.028

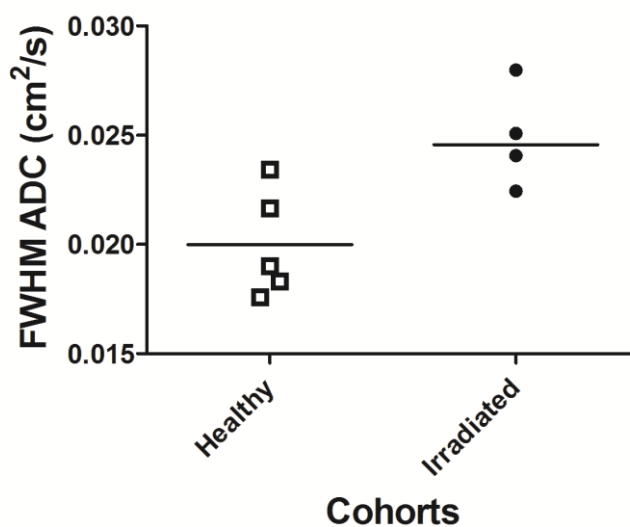


**Figure 3-15:** FWHM ADC values for healthy and irradiated cohorts. Results are obtained using a two-tailed (Mann Whitney) unpaired t-test. At the  $p < 0.05$  level, the differences of the population means are significantly different. The calculated  $p = 0.0317$ .

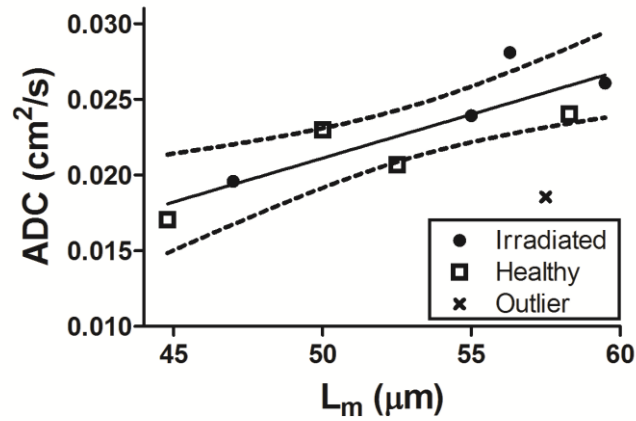


**Figure 3-16:** Summary of data obtained for 9 lung specimens (4 healthy, 4 irradiated, 1 healthy outlier). Each data point is a mean calculated across all imaging pixels for a given ADC map. The horizontal axis shows  $L_m$  obtained from direct histological measurements on the same lungs. Linear regression fit with 95% confidence band of the best-fit line and residual plot with significance  $p < 0.05$ . After excluding the outlier, the calculated  $p = 0.0061$  and  $r^2 = 0.7408$ .

## Chapter 4: Discussion and Future Work

### 4 Introduction

This chapter reflects on the main results from **Chapter 3** and the *Sectoral* waveform characterization from **Appendix A**. Future work involving optimization of the gradient waveforms, low field MRI hardware, and further development of the *Sectoral* technique for *in vivo* imaging are suggested. Conclusions are also drawn on the basis of the findings in this thesis. In particular, an improvement in SNR efficiency of *Sectoral* over the FGRE approach and the potential for *Sectoral* to be a favourable imaging tool for MRI research studies using hyperpolarized gas lung imaging are discussed.

#### 4.1 Gradient Waveform Mapping

The essential problem of eddy currents circulating in the low-field system was reduced in this study by gradient waveform mapping (as described in **Appendix A**). Eddy currents in the low-field 0.074 T MRI induced by gradient switching were measured and analyzed with the MFGM method. The *Sectoral* gradient waveforms were temporally mapped inside the MRI system using a small MFGM probe monitor. The *Sectoral* gradient waveforms for  $^{129}\text{Xe}$  require longer readout durations compared to  $^1\text{H}$  because of the larger gyromagnetic ratio. Therefore, the *Sectoral* gradient waveforms were originally mapped and optimized on a  $^1\text{H}$  filled phantom and scaled to *Sectoral*  $^{129}\text{Xe}$  waveforms. Based on the experimental results, it was determined that the *Sectoral*  $^{129}\text{Xe}$  waveforms did a reasonable job at producing *Sectoral*  $^{129}\text{Xe}$  images. Nevertheless, limitations imposed by the system including bandwidth, gradient slew rate capabilities and low SNR inherent to the initial measurement posed limitations. In future work, gradient waveform mapping with directly flowing  $^{129}\text{Xe}$  from the polarizer using a glass vessel should be performed to validate the accuracy of the waveforms. In this case the coil can remain small while maintaining high enough SNR.

The *Sectoral* input gradient waveforms were analyzed using both measured frequency-encoding (**Figure A-7**) and pure phase-encoding (**Figure A-8**) waveforms. The mapped results of the gradient waveforms indicate that the MFGM technique does a reasonable



job reproducing the desired gradient waveforms required to reconstruct *Sectoral* images. Excellent agreement between the ideal and measured data is observed in all waveforms, as represented in **Figure A-7** and **Figure A-8 (Appendix A)**, after correction by a normalization coefficient (**Figure A-6**). However, since the pre-emphasized waveforms were determined using an empirical approach, it is challenging to predict the exact alignment of data points on the Cartesian grid. Therefore, inconsistencies do exist at some peaks, where the gradient often exceeds or undershoots the desired amplitude. This reflects that some eddy currents are being produced from the previous peak of opposite polarity and contribute to the gradient deviations. Furthermore, the measured waveforms show that the pre-emphasized waveforms of discrete steps were smoothed due to eddy current effects, acting as a low-pass filter in the frequency domain. Although the effects of eddy currents are partly corrected by pre-emphasis and by scaling the  $k$ -space trajectories prior to reconstruction, some residual effects occur even for an optimally configured waveform. The MFGM technique used here was not perfect and there is still room for improvement. Future work could utilize an improved method to calculate a pre-equalized waveform that accurately measures the temporal evolution of the magnetic field gradient from the input function and extracts the system impulse response (57). A potential limitation with this method is that the  $x$ -axis and  $y$ -axis waveforms were mapped separately. It is likely that the simultaneous application of encoding gradients may affect the output gradient waveforms due to interactions between the two. Further work could also be done to expand the MFGM technique to also provide direct characterization when applying both the  $x$ -axis and  $y$ -axis gradients simultaneously.

## 4.2 Comparisons of FGRE and *Sectoral*

The first application of the *Sectoral* pulse sequence was to generate *Sectoral* images of  $^1\text{H}$  spin density, for geometric assessment of the *in vitro* phantom used, and to compare with FGRE images based on SNR efficiency.

Unlike clinical systems, the NTNMR console on the low field MRI does not offer an FOV preset. Instead, the gradient and dwell time must be manually input for each pulse sequence to adjust the FOV. For this reason, slightly different FOV between FGRE and

*Sectoral* were used with the  $^1\text{H}$  resolution phantom ( $75\times 75\text{ mm}^2$  for FGRE and  $71\times 71\text{ mm}^2$  for SB-*Sectoral*) and  $^{129}\text{Xe}$  syringe phantom ( $85\times 85\text{ mm}^2$  for FGRE,  $94\times 94\text{ mm}^2$  for SB-*Sectoral*, and  $96\times 96\text{ mm}^2$  for MB-*Sectoral*). Various gradient strengths and dwell times were tested to produce similar FOV's. However, it was challenging to know the exact gradient strength needed for a particular FOV. Since the signal is proportional to the voxel size, the efficiency equation of **Eqn. [2.2]** takes into consideration the different FOV to allow a fair comparison. Future work will involve a look-up table of different mapped FOV's, obtained by empirically measuring different combinations of gradient strength and dwell time, of a sharp-edged phantom with well-known dimensions.

With the *Sectoral* sequence, a desired number of data points directly fall onto a Cartesian grid, permitting normal image reconstruction with a 2-D inverse Fourier transform, and thus avoiding interpolation/re-gridding steps or optimization density compensation functions. The *Sectoral* sequence in this work utilizes every eighth data point, and ignores the data points between each of the Cartesian bound points during reconstruction. This was implemented in an attempt to mitigate the effects of the abrupt gradient changes seen in the *Sectoral*  $k$ -space trajectory. The consequence of such abrupt gradient changes leads to an overshooting of the  $k$ -space trajectory that can manifest as high intensity noise spikes (i.e. a bright or white pixel artifact). After proper calibration of the MRI system, future studies can use fewer sampling points by increasing the dwell time. Moreover, the sampled points that don't fall onto the Cartesian grid could potentially be salvaged and adopted in future work by implementing additional image reconstruction algorithms. By applying a proper density weighting function and interpolating the sampling points that are outside the Cartesian grid, a secondary image could be constructed and averaged with the Cartesian-based image to improve SNR.

In this work, an improvement in efficiency is demonstrated with *Sectoral* over FGRE, as summarized in **Table 3-1** ( $^1\text{H}$ ) and **Table 3-2** ( $^{129}\text{Xe}$ ). Although *Sectoral* has been developed specifically with  $^{129}\text{Xe}$  applications in mind, SB-*Sectoral* shows 3.12 times greater efficiency than FGRE with  $^1\text{H}$  imaging. In the case of  $^{129}\text{Xe}$ , SB-*Sectoral* is 2.07 and MB-*Sectoral* is 9.32 times more efficient than FGRE. While a high level of noise ( $9.0\times$  greater) is introduced by the *Sectoral* imaging gradients with this MRI system at

the  $^{129}\text{Xe}$  frequency, an improvement in efficiency with *Sectoral* over FGRE is still evident for both  $^1\text{H}$  and  $^{129}\text{Xe}$  imaging. This means that the *Sectoral* approach is expected to provide even greater improvement in SNR efficiency (factor  $\sim 10$ ) if this noise source can be eliminated. In this case, a simple, empirical correction based on the additional gradient-associated noise level was implemented to allow a fair assessment of the data. After correcting for gradient-associated noise, SB-*Sectoral* is 16.71 and MB-*Sectoral* is 79.13 times more efficient than FGRE. This additional gradient-associated noise level seems to be unique to the MRI system occurring only near the xenon frequency (0.883 MHz). *Sectoral* measurements at higher frequencies (3.163 MHz) were performed and the gradient-associated noise was not detected. It is suspected that the source of the gradient-associated noise may either be from a manifestation of mechanical oscillating vibrations that is physically contacting the metal structures of the gradients from something loose in the MRI system or a consequence of an incompatibility of the *Sectoral* switching at the  $^{129}\text{Xe}$  frequency. Future  $^{129}\text{Xe}$  *Sectoral* imaging will attempt to be performed at a higher frequency (above 1.0 MHz) to avoid this noise source.

The second use of the *Sectoral* pulse sequence was to produce ventilation images to show the distribution of a bolus injection of  $^{129}\text{Xe}$  and compare them with FGRE images based on SNR efficiency. The clearest advantage of *Sectoral* over FGRE is the higher achievable SNR with  $^{129}\text{Xe}$  imaging. FGRE requires 64 RF pulses to encode the entire  $k$ -space matrix but *Sectoral* only needs 16. Since *Sectoral* uses fewer RF pulses than FGRE to fill  $k$ -space, the tip angles (**Table 2-1**), and thus generated MRI signals, are greater. This translates to an increase in SNR. However, the sequence could be modified to boost SNR further, at the expense of resolution, by decreasing the amount of sectors. On the other hand, some SNR loss would be expected if it is more desirable to increase resolution by increasing the amount of sectors.

The 2-D *Sectoral* and FGRE sequence can be extended to 3-D imaging. The simplest method being the addition of a slice select gradient along the  $z$ -axis to acquire multi-slice images. A possible future extension of the *Sectoral* sequence will attempt to achieve isotropic spatial resolution using 3-D imaging approaches (59). The advantage of such a true 3-D approach is an expected improvement in SNR efficiency over 2-D multi-slice

acquisitions of similar slice thickness, in addition to well-defined slices observed in any orientation.

### 4.3 ADC of Phantoms

The ADC value is a quantitative parameter of diffusion-weighted MRI representing the mean displacement of  $^{129}\text{Xe}$  atoms. The results graphed in **Figure 3-5** and **Figure 3-6** show that the *Sectoral* technique is able to accurately demonstrate signal alterations caused by the increased diffusion coefficient due to introduced  $\text{N}_2$ . The *mean* ADC values of pure  $^{129}\text{Xe}$  reported here using MB-*Sectoral* ( $0.051 \pm 0.003 \text{ cm}^2/\text{s}$ ) and SB-*Sectoral* ( $0.056 \pm 0.008 \text{ cm}^2/\text{s}$ ) are close to what we expect for the diffusion of xenon gas ( $0.061 \text{ cm}^2/\text{s}$ ) in air (56) and ADC of other studies using similar experiment conditions ( $0.0559 \text{ cm}^2/\text{s}$ ) (55). The *mean* ADC values obtained, which are slightly smaller than the self-coefficient of  $^{129}\text{Xe}$ , indicate that the xenon gas atoms may have been confined by the syringe walls, and thus exhibit slightly restrictive diffusion. In the measurements with mixed  $^{129}\text{Xe}-\text{N}_2$ , the *mean* ADC in the syringe was found to increase to  $0.073 \pm 0.015 \text{ cm}^2/\text{s}$  for MB-*Sectoral* ( $\text{N}_2$  volume = 6.4 ml) and  $0.075 \pm 0.019 \text{ cm}^2/\text{s}$  for SB-*Sectoral* ( $\text{N}_2$  volume = 4.8 ml). These values increase the self-diffusion coefficient of pure xenon, confirming dilution by the lighter  $\text{N}_2$  gas. The discrepancy between MB-*Sectoral* and SB-*Sectoral* values can be explained by the decrease in SNR of SB-*Sectoral*, resulting in greater standard deviation caused by noise in the images. It is expected that this technique will show changes associated with the restriction of molecular  $^{129}\text{Xe}$  movement in healthy and disease lung parenchyma. Greater number of iterations (i.e. more *b*-values) can improve the accuracy of results at a cost of lower SNR and longer scan time.

$\text{N}_2$ , as a low molecular weight molecule, has a much larger diffusion coefficient than  $^{129}\text{Xe}$ , implicating ADC and in turn influencing  $T_2^*$ . The effect of higher diffusion in the  $^{129}\text{Xe}-\text{N}_2$  mixtures shortens  $T_2^*$  as the rapid spin dephasing is enhanced by susceptibility effects. However, such quantification is challenging due to inhomogeneous effects of susceptibility on the  $B_0$  field. Therefore, after improved MRI system calibration in future work, *Sectoral*  $T_2^*$  mapping may be exploited to reveal information related to the microstructure of lung tissue.

## 4.4 $T_1$ and $p_AO_2$ of Phantoms

It is reasonable to expect that the concentration of  $O_2$ , such as during inhalation, will cause a dependence on the expected  $p_AO_2$ . The obtained *SB-Sectoral* (**Figure 3-11**)  $T_1$ -based, and thus  $p_AO_2$ -based, maps are noisier than those of *MB-Sectoral* (**Figure 3-10**) in the underlying  $^{129}\text{Xe}$  images. The higher SNR levels accompanying the *MB-Sectoral* results are related to the lower pixel deviation, represented by the vertical error bars. However, the highest deviations are observed in the first measurement and are likely due to the short  $\Delta t_{os}$  of 10.0 s, thus producing inadequate  $T_1$ -weighting in the absence of  $O_2$ . Although the noise in *SB-Sectoral* data is greater than *MB-Sectoral*, the trends from both types of experiments are similar, showing a linear decrease in  $T_1$  and a linear increase in  $p_AO_2$  with higher concentration of  $O_2$  as expected. The large vertical error bars seen in *SB-Sectoral* are simply a by-product of low SNR occurring as a consequence of both low  $^{129}\text{Xe}$  polarization (< 5%) and longitudinal magnetization consumption by repeated RF excitations (32 VFA pulses for both images).

Although the use of low magnetic field strength provides longer  $T_2^*$  and consequently longer read-out times, residual transverse magnetization from one sector to the next may cause interference (e.g. stimulated echoes). To mitigate this in future, additional crusher gradients could be applied to the sequence, following the readout window, to de-phase any remaining magnetization in the transverse plane before the next excitation RF pulse.

If calibrated correctly, the VFA approach compensates for the RF pulse history by ensuring constant signal intensity between sectors. In practice, the VFA calibration of sectors is straightforward, requiring only a few short duration injections of  $^{129}\text{Xe}$  to optimize the RF power setting. The benefit of VFA implementation is that  $T_1$  can be calculated directly from reconstructed images without further flip angle correction. The sensitivity of *Sectoral*  $p_AO_2$ -mapping to changes in oxygenation measured here *in vitro* is expected to be consistent with the change of *in vivo* lung  $O_2$  concentration per breath (50). In this study, a variation in  $T_1$  values was observed in  $T_1$  maps presumably associated with signal variations arising from non-uniform excitation flip angles and inaccurate RF calibrations. Off-line image reconstruction and analysis was required to

map  $B_1$  in order to compensate for these underlying  $B_1$  variations. In future work, this requirement could be omitted by using more homogenous transmit coils (e.g. bird-cage) and/or better pre-scan calibration techniques.

## 4.5 Ventilation Imaging of Rat Lungs

The primary application of the *Sectoral* pulse sequence *in vivo* was to produce ventilation images that show the distribution of a single bolus of inhaled  $^{129}\text{Xe}$  under breath-hold conditions. The rat lung images obtained with MB-*Sectoral* demonstrate the potential of this new pulse sequence for capturing the features of the lungs with  $^{129}\text{Xe}$  at low field. In **Figure 3-12** a *Sectoral*  $^{129}\text{Xe}$  whole-lung 2-D projection images of a rat lung in the coronal view (middle) and axial (right) view are shown. A photograph of the rat lung is also shown for comparison (**Figure 3-12**, left). The trachea is faintly seen, the general lung shape is visible, and the left and right lobes can be seen branching out. Based on the SNR values shown in **Table 3-6**, the images from the *Sectoral* pulse sequences were improved compared to those from the conventional FGRE sequence. The uncorrected SNR results of FGRE and SB-*Sectoral* are comparable due to the very low polarizations (< 5%) of  $^{129}\text{Xe}$  in this experiment and the additional gradient-associated noise with *Sectoral*. Still, an SNR improvement of 5.47 in MB-*Sectoral* is seen. If the additional gradient-associated noise level was eliminated, the SB-*Sectoral* and MB-*Sectoral* sequence SNR is expected to improve by 2.09 and 44.66, respectively, based on the SNR values after correction. These SNR values differ from the *in vitro* results because the lower SNR *in vivo* may be attributed to a greater reduction in  $T_2^*$  occurring from magnetic susceptibility effects and depolarization from the  $^{129}\text{Xe}$ - $\text{O}_2$  mixing in the lungs. In this study, naturally-abundant  $^{129}\text{Xe}$  (26%  $^{129}\text{Xe}$ ) was used. Improved polarization and the use of enriched (86%)  $^{129}\text{Xe}$  are expected to improve signal in future, potentially eliminating the need for MB-*Sectoral*.

## 4.6 ADC of Rat Lungs

The secondary *in vivo* use of the *Sectoral* pulse sequence was to validate  $^{129}\text{Xe}$  diffusion-weighting with histology to explore whether the sequence can be accepted as a reliable technique to measure lung tissue density. The work presented here shows for the first

time  $^{129}\text{Xe}$  ADC maps of healthy and irradiated rat lungs obtained at low field. Anatomical projection images showing ventilation (**Figure 3-13**) or ADC (**Figure 3-14**) maps, in general, were not very demonstrative of RILI in this pilot study. The present images were generally very similar between the two cohorts although some minor ventilation non-uniformities can be seen in the irradiated rat lung ADC map (**Figure 3-14**, right).

The data presented here provide the first opportunity to directly compare *Sectoral*  $^{129}\text{Xe}$  global ADC with histological measurements in the same lungs. The measured ADC values in the lungs (**Table 3-7**) overall are significantly reduced compared to the self-diffusion coefficient ( $0.061 \text{ cm}^2/\text{s}$ ) and phantom ADC (**Table 3-3**) values. This is expected because the diffusion of the  $^{129}\text{Xe}$  gas atoms is restricted by the walls of the distal air spaces (i.e. alveoli). Therefore, the ADC measured with  $^{129}\text{Xe}$  is a quantitative measure of microstructure, and is potentially useful for detecting changes associated with alveolar wall thickening during inflammation, post-irradiation. It was previously hypothesized that 2-weeks post-irradiation is the initial stage of lung damage where  $^{129}\text{Xe}$  diffusion MRI techniques might be most valuable (32). Both the healthy and the irradiated rat cohorts appeared to have heterogeneous distributions of ADC values, with a slightly more heterogeneous distribution in the irradiated rat (**Figure 3-14**). A decrease in ADC values in the irradiated rats (**Figure 3-14**, right) was expected based on alveolar wall thickening confirmed by histology. However, the heterogeneous distribution of ADC in the healthy rat cohorts (**Figure 3-14**, left) is surprising because much greater homogeneity was expected with the larger alveolar dimension in the normal healthy lung, and therefore subjecting  $^{129}\text{Xe}$  gas to less restriction to diffusion. Furthermore, some rats in the healthy cohort demonstrated reduced ADC and correspondingly showed inflammation by histology. The rats were housed in open-barred cages, exposing them to potential cross-contamination between rats with infections and accidental exposure to infectious material brought in from exposure to personnel. The use of enclosed cage systems and independent high-efficiency particulate air (HEPA) filtration to minimize infection will be an easy implementation for future cohort studies.

The *mean* ADC values for the healthy and irradiated rats were initially compared but showed no significant difference ( $p > 0.05$ ) between the two cohorts. This may be due to the heterogeneous contributions of radiation damage to the *mean* ADC and/or the possibility that some irradiated rats did not demonstrate RILI (discussed further below). The calculations were then repeated by extracting the FWHM ADC, which was calculated from the Gaussian distribution of each lung ADC histogram (as described in **section 2.12**). **Figure 3-15** shows good distinction between the healthy and irradiated rats for the global FWHM ADC *Sectoral* results. A clear separation with a strong correlation ( $p < 0.05$ ) between healthy rats and for irradiated rats was demonstrated using the FWHM ADC of  $^{129}\text{Xe}$  with *Sectoral*. FWHM ADC increases may be attributable to heterogeneous distribution of air space sizes following irradiation, presumably by RILI. Therefore, ADC was directly compared to mean linear intercept,  $L_m$ , measured by histology.

**Table 3-7** and **Figure 3-16** summarize the correlation between  $^{129}\text{Xe}$  diffusion measurements (i.e. *mean* ADC) and  $L_m$  following removal of one outlier (as described below). The *mean* ADC values from *Sectoral* ADC maps did show a strong correlation when compared with  $L_m$ , as measured by lung histology. The  $L_m$  is the mean distance from tissue interfaces, between the air spaces, seen on histological slide samples obtained from fixed lungs. The reason why some (3) irradiated rats did not show evidence of RILI using the *mean* ADC is unclear, but possibly due to the difference in immunological response of different animals or the difference in the time course of RILI for those specific animals.

One healthy outlier was excluded in the statistical analysis because the low *mean* ADC value did changed the distribution skewness to just above significance ( $p > 0.05$ ). The rat with the low *mean* ADC of the healthy outlier was housed in an open-barred cage, exposing it to accidental infection from cross-contamination between rats, which lead to inflammation. To address this concern in future *in vivo* studies, HEPA filters will be used to prevent infection. Sometimes the affected areas of the diseased lung may be minor, heterogeneous, or spread out. This introduces a challenge for quantification strategies of disease severity such as  $L_m$  because it tends to underestimate the influence of variable air



space size and outliers (67). Therefore, future work should investigate other histological analysis that may better assess the ability to detect very early stages of airway constriction such as tissue thickness and percent area.

The ability of *Sectoral* to detect lung injury supports the hypothesis that the *Sectoral* diffusion-weighted sequence, with  $^{129}\text{Xe}$ , possesses the ability and potential to assess RILI and correlate it with histology. Despite the limitation of a relatively low number of rats used in this study, even with the current techniques (i.e. low polarization and high gradient-associated noise), both a strong correlation is seen between  $L_m$  and ADC, allowing separation between healthy and irradiated cohorts using FWHM ADC. A limitation of *Sectoral* diffusion-weighting is that ADC maps are only acquired from measured areas in ventilated regions of the lung. In this study, all the lungs showed good whole lung ventilation, indicating that imaging was not constrained by unventilated areas. However, extending the *Sectoral* diffusion-weighted sequence to lung cancer or human patients with COPD, where regions of low ventilation are commonly seen due to airway obstruction, would be a limitation. Future extensions of this type of study with *Sectoral* will include time courses following the progression of ADC in this and other disease models (i.e. emphysema). A larger number of rats could potentially permit the detection of a separation between healthy and irradiated cohorts using *mean* ADC instead of FWHM ADC.

Even though **Figure 3-16** shows good correlation between morphometric and ADC measurements, the ADC values in healthy lungs can exhibit broad variability. This is because the ADC not only depends on the lung microstructure, but also on pulse sequence parameters (i.e. diffusion time, b-value). Since *Sectoral* is a new pulse sequence and very few *in vivo*  $^{129}\text{Xe}$  ADC studies have been performed to study RILI, the choice of optimal parameters is limited as there is little guidance. Therefore, the sensitivity of *Sectoral* to detect structural changes of RILI with  $^{129}\text{Xe}$  may have been limited due to the choice of imaging parameters. The optimization of *Sectoral*  $^{129}\text{Xe}$  imaging for measuring changes associated with RILI will be an area for future research.

## 4.7 Summary of Thesis

The pseudo-Cartesian *Sectoral* imaging method proposed in this thesis is the frequency-encode extension of the phase-encoding Sectoral-SPRITE sequence. As the  $k$ -space trajectory employs the use of Cartesian patterns to directly sample  $k$ -space points on a Cartesian grid for reconstruction, no further interpolation or density weighting functions are required during re-gridding. In combination with VFA RF pulses, the *Sectoral* imaging pulse sequence is a new approach for the acquisition of hyperpolarized  $^{129}\text{Xe}$  gas lung imaging at low magnetic field strength (0.07 T). *Sectoral* imaging was demonstrated *in vitro* for proof of concept and showed favourable improvements in SNR efficiency over FGRE imaging. A series of *Sectoral*  $^{129}\text{Xe}$  gas images of phantoms were obtained to extract from them a number of structural and functional parameters, including, ADC and  $p_{\text{A}}\text{O}_2$ . Measured global ADC values calculated from *Sectoral* maps of ADC were found to increase with greater dilution by lighter  $\text{N}_2$  gas, confirming that *Sectoral* diffusion-weighted MRI is a sensitive biomarker, capable of detecting a response to diffusivity change. Similarly, *Sectoral*  $p_{\text{A}}\text{O}_2$  values calculated from *Sectoral*  $T_1$  maps of greater  $\text{O}_2$  concentration showed that *Sectoral* is sensitive to the increase in oxygenation measured *in vitro*. In the case of *in vivo*, the *Sectoral* sequence was shown to be effective for imaging of  $^{129}\text{Xe}$  inhalation in rat lungs. In a pilot study of RILI, a significant difference was observed between irradiated and healthy rat lungs by extracting the FWHM of bulk ADC values measured by *Sectoral* diffusion-weighting. *Sectoral* diffusivity measurements showed positive linear correlation between  $^{129}\text{Xe}$  diffusivity and histological interpretation with  $L_m$ , reflecting that *Sectoral* diffusion MRI with  $^{129}\text{Xe}$  may be sensitive to the geometry of the individual alveoli. The work presented here *in vitro* and *in vivo* forms the basis for future *in vivo* *Sectoral* studies of rodent lungs of specific disease models such as RILI. It is expected that the *Sectoral* approach will provide additional information on the physiology and pathophysiology of the lung, with potential for pre-clinical research and clinically-relevant uses and applications.

## References

1. Levitzky M. Pulmonary Physiology (Lange Physiology). McGraw Hill Medical; 2003.
2. Canadian Cancer Society. Canadian Cancer Society's Advisory Committee on Cancer Statistics [Internet]. Canadian Cancer Statistics; 2013. Available from: <http://www.cancer.ca/~media/cancer.ca/CW/cancer%20information/cancer%20101/Canadian%20cancer%20statistics/canadian-cancer-statistics-2013-EN.pdf>
3. Siegel R, Ma J, Zou Z, Ahmedin J. Cancer statistics, 2014. *CA Cancer J Clin*. 2014 Jan;63(1):9–29.
4. Sher T, Dy GK, Adjei AA. Small cell lung cancer. Elsevier; 2008. p. 355–67.
5. Navada S, Lai P, Schwartz A, Kalemkerian G. Temporal trends in small cell lung cancer: analysis of the national Surveillance, Epidemiology, and End-Results (SEER) database. *J Clin Oncol*. 2006;24(18 suppl):7082.
6. Gross NJ. Pulmonary effects of radiation therapy. *Ann Intern Med*. 1977;86(1):81–92.
7. Milano MT, Constine LS, Okunieff P. Normal Tissue Tolerance Dose Metrics for Radiation Therapy of Major Organs. *Semin Radiat Oncol*. 2007 Apr;17(2):131–40.
8. M. Bentzen JS. Quantitative clinical radiobiology of early and late lung reactions. *Int J Radiat Biol*. 2000;76(4):453–62.
9. Keall PJ, Mageras GS, Balter JM, Emery RS, Forster KM, Jiang SB, et al. The management of respiratory motion in radiation oncology report of AAPM Task Group 76. *Med Phys*. 2006;33(10):3874.
10. Barriger RB, Forquer JA, Brabham JG, Andolino DL, Shapiro RH, Henderson MA, et al. A Dose–Volume Analysis of Radiation Pneumonitis in Non–Small Cell Lung Cancer Patients Treated With Stereotactic Body Radiation Therapy. *Int J Radiat Oncol*. 2012 Jan;82(1):457–62.
11. Benveniste MFK, Welsh J, Godoy MCB, Betancourt SL, Mawlawi OR, Munden RF. New era of radiotherapy: An update in radiation-induced lung disease. *Clin Radiol*. 2013 Jun;68(6):e275–90.
12. Movsas B, Raffin TA, Epstein AH, Link CJ. Pulmonary radiation injury. *CHEST J*. 1997;111(4):1061–76.
13. Kocak Z, Evans ES, Zhou S-M, Miller KL, Folz RJ, Shafman TD, et al. Challenges in defining radiation pneumonitis in patients with lung cancer. *Int J Radiat Oncol*. 2005 Jul;62(3):635–8.

14. Khan MA, Hill RP, Van Dyk J. Partial volume rat lung irradiation: an evaluation of early DNA damage. *Int J Radiat Oncol Biol Phys.* 1998;40(2):467–76.
15. Khan MA, Van Dyk J, Yeung IW, Hill RP. Partial volume rat lung irradiation; assessment of early DNA damage in different lung regions and effect of radical scavengers. *Radiother Oncol.* 2003;66(1):95–102.
16. Notter RH, Finkelstein J, Holm B. *Lung Injury: Mechanisms, Pathophysiology, and Therapy.* CRC Press; 2005.
17. Miller MR. Standardisation of spirometry. *Eur Respir J.* 2005 Aug 1;26(2):319–38.
18. Rabe KF, Hurd S, Anzueto A, Barnes PJ, Buist SA, Calverley P, et al. Global Strategy for the Diagnosis, Management, and Prevention of Chronic Obstructive Pulmonary Disease: GOLD Executive Summary. *Am J Respir Crit Care Med.* 2007 Sep 15;176(6):532–55.
19. Miyazaki M, Nakamura H, Chubachi S, Sasaki M, Haraguchi M, Yoshida S, et al. Analysis of comorbid factors that increase the COPD assessment test scores. *Respir Res.* 2014;15(1):13.
20. Vanfleteren LEGW, Spruit MA, Groenen M, Gaffron S, van Empel VPM, Bruijnzeel PLB, et al. Clusters of Comorbidities Based on Validated Objective Measurements and Systemic Inflammation in Patients with Chronic Obstructive Pulmonary Disease. *Am J Respir Crit Care Med.* 2013 Apr;187(7):728–35.
21. Libshitz HI, Shuman LS. Radiation-induced pulmonary change: CT findings. *J Comput Assist Tomogr.* 1984;8(1):15–9.
22. Hill RP. Radiation effects on the respiratory system. *Br J Radiol.* 2005 Jan 1;75–81.
23. Saito S, Murase K. Detection and Early Phase Assessment of Radiation-Induced Lung Injury in Mice Using Micro-CT. Muñoz-Barrutia A, editor. *PLoS ONE.* 2012 Sep 24;7(9):e45960.
24. Seppenwoolde Y, De Jaeger K, Boersma LJ, Belderbos JSA, Lebesque JV. Regional differences in lung radiosensitivity after radiotherapy for non-small-cell lung cancer. *Int J Radiat Oncol.* 2004 Nov;60(3):748–58.
25. Lauterbur PC. Image formation by induced local interactions: examples employing nuclear magnetic resonance. *Nature.* 1973;242(5394):190–1.
26. Bergin C, Glover G, Pauly J. Lung parenchyma: magnetic susceptibility in MR imaging. *Radiology.* 1991;180(3):845–8.
27. Albert M, Cates G, Driehuys B, Happer W, Saam B, Springer C, et al. Biological magnetic resonance imaging using laser-polarized  $^{129}\text{Xe}$ . 1994;

28. Ireland RH, Din OS, Swinscoe JA, Woodhouse N, van Beek EJR, Wild JM, et al. Detection of radiation-induced lung injury in non-small cell lung cancer patients using hyperpolarized helium-3 magnetic resonance imaging. *Radiother Oncol*. 2010 Nov;97(2):244–8.
29. Mathew L, VanDyk J, Etemad-Rezai R, Rodrigues G, Parraga G. Hyperpolarized  $^3\text{He}$  pulmonary functional magnetic resonance imaging prior to radiation therapy. *Med Phys*. 2012;39(7):4284–90.
30. Mathew L, Wheatley A, Castillo R, Castillo E, Rodrigues G, Guerrero T, et al. Hyperpolarized  $^3\text{He}$  Magnetic Resonance Imaging. *Acad Radiol*. 2012 Dec;19(12):1546–53.
31. Allen AM, Albert M, Caglar HB, Zygmanski P, Soto R, Killoran J, et al. Can Hyperpolarized Helium MRI add to radiation planning and follow-up in lung cancer? *J Appl Clin Med Phys* [Internet]. 2011 [cited 2014 May 22];12(2). Available from: <http://www.jacmp.org/index.php/jacmp/article/viewArticle/3357>
32. Fox MS, Ouriadov A, Thind K, Hegarty E, Wong E, Hope A, et al. Detection of radiation induced lung injury in rats using dynamic hyperpolarized  $^{129}\text{Xe}$  magnetic resonance spectroscopy. *Med Phys*. 2014 Jul;41(7):072302.
33. Thind K, Chen A, Friesen-Waldner L, Ouriadov A, Scholl TJ, Fox M, et al. Detection of radiation-induced lung injury using hyperpolarized  $^{13}\text{C}$  magnetic resonance spectroscopy and imaging: Detection of RILI. *Magn Reson Med*. 2013 Sep;70(3):601–9.
34. Thind K, Jensen MD, Hegarty E, Chen AP, Lim H, Martinez-Santesteban F, et al. Mapping metabolic changes associated with early Radiation Induced Lung Injury post conformal radiotherapy using hyperpolarized  $^{13}\text{C}$ -pyruvate Magnetic Resonance Spectroscopic Imaging. *Radiother Oncol*. 2014 Feb;110(2):317–22.
35. Hanson LG. Is quantum mechanics necessary for understanding magnetic resonance? *Concepts Magn Reson Part A*. 2008 Sep;32A(5):329–40.
36. Driehuys B, Cates GD, Miron E, Sauer K, Walter DK, Happer W. High-volume production of laser-polarized  $^{129}\text{Xe}$ . *Appl Phys Lett*. 1996;69(12):1668.
37. Newbury N, Barton A, Cates G, Happer W, Middleton H. Gaseous  $^3\text{He}$ - $^3\text{He}$  magnetic dipolar spin relaxation. *Phys Rev A*. 1993;48(6):4411.
38. Venkatesh AK, Zhang AX, Mansour J, Kubatina L, Oh C-H, Blasche G, et al. MRI of the lung gas-space at very low-field using hyperpolarized noble gases. *Magn Reson Imaging*. 2003 Sep;21(7):773–6.
39. Weathersby P, Homer L. Solubility of inert gases in biological fluids and tissues: a review. *Undersea Biomed Res*. 1980;7(4):277–96.

40. Andersen AM, Ladefoged J. Partition coefficient of  $^{133}\text{Xenon}$  between various tissues and blood in vivo. *Scand J Clin Lab Invest*. 1967;19(1):72–8.
41. Walker TG, Happer W. Spin-exchange optical pumping of noble-gas nuclei. *Rev Mod Phys*. 1997;69(2):629.
42. Happer W, Miron E, Schaefer S, Schreiber D, Van Wijngaarden WA, Zeng X. Polarization of the nuclear spins of noble-gas atoms by spin exchange with optically pumped alkali-metal atoms. *Phys Rev A*. 1984;29(6):3092.
43. Tseng CH, Wong GP, Pomeroy VR, Mair RW, Hinton DP, Hoffmann D, et al. Low-field MRI of laser polarized noble gas. *Phys Rev Lett*. 1998;81(17):3785–8.
44. Qualitätsmanagement in der Medizin. Landsberg am Lech: ecomed; 1996.
45. Marti-Bonmati L, Kormano M. MR equipment acquisition strategies: low-field or high-field scanners. *Eur Radiol*. 1997;7(5):S263–8.
46. Parra-Robles J, Cross AR, Santyr GE. Theoretical signal-to-noise ratio and spatial resolution dependence on the magnetic field strength for hyperpolarized noble gas magnetic resonance imaging of human lungs. *Med Phys*. 2005;32(1):221.
47. Durand E, Guillot G, Darrasse L, Tastevin G, Nacher PJ, Vignaud A, et al. CPMG measurements and ultrafast imaging in human lungs with hyperpolarized helium-3 at low field (0.1 T). *Magn Reson Med*. 2002 Jan;47(1):75–81.
48. Parra-Robles J, Cross AR, Santyr GE. Erratum: “Theoretical signal-to-noise ratio and spatial resolution dependence on the magnetic field strength for hyperpolarized noble gas magnetic resonance imaging of human lungs” [*Med. Phys.* 32, 221–229 (2005)]. *Med Phys*. 2006;33(5):1525.
49. Möller HE, Chen XJ, Saam B, Hagspiel KD, Johnson GA, Altes TA, et al. MRI of the lungs using hyperpolarized noble gases. *Magn Reson Med*. 2002;47(6):1029–51.
50. Ouriadov AV, Lam WW, Santyr GE. Rapid 3-D mapping of hyperpolarized  $^3\text{He}$  spin-lattice relaxation times using variable flip angle gradient echo imaging with application to alveolar oxygen partial pressure measurement in rat lungs. *Magn Reson Mater Phys Biol Med*. 2009 Oct;22(5):309–18.
51. Miller GW, Altes TA, Brookeman JR, de Lange EE, Mugler III JP. Hyperpolarized  $^3\text{He}$  lung ventilation imaging with B<sub>1</sub>-inhomogeneity correction in a single breath-hold scan. *Magn Reson Mater Phys Biol Med*. 2004 Apr;16(5):218–26.
52. Saam, Happer, Middleton. Nuclear relaxation of  $^3\text{He}$  in the presence of  $\text{O}_2$ . *Phys Rev A*. 1995 Jul;52(1):862–5.
53. Kraayvanger RJ, Bidinosti CP, Dominguez-Viqueira W, Parra-Robles J, Fox M, Lam WW, et al. Measurement of alveolar oxygen partial pressure in the rat lung

- using Carr-Purcell-Meiboom-Gill spin-spin relaxation times of hyperpolarized  $^3\text{He}$  and  $^{129}\text{Xe}$  at 74 mT. *Magn Reson Med.* 2010 Nov;64(5):1484–90.
54. Eberle B, Weiler N, Markstaller K, Kauczor H-U, Deninger A, Ebert M, et al. Analysis of intrapulmonary  $\text{O}_2$  concentration by MR imaging of inhaled hyperpolarized helium-3. *J Appl Physiol.* 1999;87(6):2043–52.
  55. Boudreau M, Xu X, Santyr GE. Measurement of  $^{129}\text{Xe}$  gas apparent diffusion coefficient anisotropy in an elastase-instilled rat model of emphysema. *Magn Reson Med.* 2013;69(1):211–20.
  56. Chen XJ, Möller HE, Chawla MS, Cofer GP, Driehuys B, Hedlund LW, et al. Spatially resolved measurements of hyperpolarized gas properties in the lung in vivo. Part I: diffusion coefficient. *Magn Reson Med.* 1999;42(4):721–8.
  57. Goora FG, Colpitts BG, Balcom BJ. Arbitrary magnetic field gradient waveform correction using an impulse response based pre-equalization technique. *J Magn Reson.* 2014 Jan;238:70–6.
  58. Czervionke L, Daniels D, Wehrli F, Mark L, Hendrix L, Strandt J, et al. Magnetic susceptibility artifacts in gradient-recalled echo MR imaging. *Am J Neuroradiol.* 1988;9(6):1149–55.
  59. Khrapitchev AA, Newling B, Balcom BJ. Sectoral sampling in centric-scan SPRITE magnetic resonance imaging. *J Magn Reson.* 2006 Feb;178(2):288–96.
  60. Addy NO, Wu HH, Nishimura DG. Simple method for MR gradient system characterization and k-space trajectory estimation. *Magn Reson Med.* 2012 Jul;68(1):120–9.
  61. Han H, MacGregor RP, Balcom BJ. Pure phase encode magnetic field gradient monitor. *J Magn Reson.* 2009 Dec;201(2):212–7.
  62. Jiru F. Introduction to post-processing techniques. *Eur J Radiol.* 2008 Aug;67(2):202–17.
  63. Aja-Fernandez S, Niethammer M, Kubicki M, Shenton ME, Westin C-F. Restoration of DWI Data Using a Rician LMMSE Estimator. *IEEE Trans Med Imaging.* 2008 Oct;27(10):1389–403.
  64. Dominguez-Viqueira W, Parra-Robles J, Fox M, Handler WB, Chronik BA, Santyr GE. A variable field strength system for hyperpolarized noble gas MR imaging of rodent lungs. *Concepts Magn Reson Part B Magn Reson Eng.* 2008 Apr;33B(2):124–37.
  65. Dominguez-Viqueira W, Berger W, Parra-Robles J, Santyr GE. Litz wire radiofrequency receive coils for hyperpolarized noble gas MR imaging of rodent

- lungs at 73.5 mT. Concepts Magn Reson Part B Magn Reson Eng. 2010 Apr;37B(2):75–85.
66. Zhao L, Mulkern R, Tseng C-H, Williamson D, Patz S, Kraft R, et al. Gradient-Echo Imaging Considerations for Hyperpolarized<sup>129</sup>Xe MR. J Magn Reson B. 1996;113(2):179–83.
  67. Weibel ER, Hsia CCW, Ochs M. How much is there really? Why stereology is essential in lung morphometry. J Appl Physiol. 2006 Sep 7;102(1):459–67.



## Appendix A: Gradient Waveform Mapping

The gradient waveform mapping technique described here is an extension of the work done by a previous undergraduate student in Dr. Santyr's group, Susannah Hickling, during her fourth year thesis project. Here the sequence is updated to use 4 RF pulses instead of 1, decreasing the time required to map the waveforms. This work also utilizes a new RF probe head with phantom and uses a normalization coefficient that eliminates the need for a re-gridding using interpolation.

### A.1 Methodology

Prior to imaging, the MFGM technique was applied using the previously described low field 74 mT MRI system to measure the magnetic field temporal evolution associated with the *Sectoral* gradient waveforms. A small RF probe (radius = 2.0 cm) with an associated circular test phantom (**Figure A-1**) was used to temporally and spatially map the behavior of the gradients. The circular phantom (radius = 1.75 cm, volume = 3.0 ml) was filled with a mixture of 2.0 ml water and 1.0 ml of gadolinium-DTPA contrast agent (Magnevist, Berlex Inc., Lachine, Quebec) to decrease  $T_1$  relaxation times, such that complete magnetization recovery was possible between each excitation.

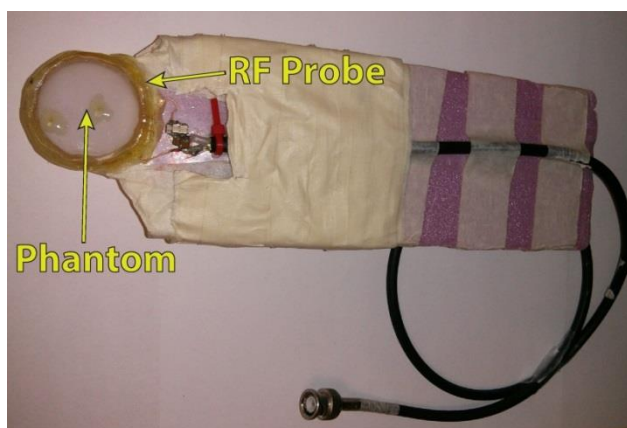


**Figure A-1:** A photograph of the probe head setup with phantom for gradient waveform mapping. The plastic circular phantom contained 2.0 ml of water and 1.0 ml of Magnevist and was placed within a small surface coil wound from Litz wire.

The probe was placed at the gradient isocenter inside the sample space. The small size of the reference phantom allowed for an isolated signal to be obtained at various positions

within the magnet bore. At a specific time during the gradient waveform acquisition, a single FID was acquired along with its associated phase. The mean gradient over the phase-encoding time,  $G_r(t)$ , was then determined using:

$$G_r(t) = \frac{\theta_r(t)}{\gamma \cdot t_p \cdot b_{os}}, \quad [\text{A.1}]$$

where  $r$  was the gradient axis ( $x$  or  $y$ ),  $\gamma$  was the gyromagnetic ratio,  $t_p$  was the constant phase-encoding time,  $\theta_r(t)$  was the signal phase at time,  $t$ , and  $b_{os}$  was the off-set from the gradient isocentre.

The MFGM technique was applied to observe and correct the associated eddy-current effects. **Figure A-2** illustrates the pulse sequence used to implement the MFGM technique. Each sector's corresponding  $x$ -axis and  $y$ -axis gradient waveforms from **Figure 1-13** were mapped individually. A baseline phase was obtained by applying four RF pulses prior to the gradient. Four RF pulses were then applied throughout the duration of the gradient waveform followed by accumulated phase measurements during time  $t_p$ , after the excitation. Each RF pulse was separated by an 8.0 ms interval (i.e. TR) to permit complete relaxation of the signal. The phase-encoding time used was 24.0  $\mu$ s for each RF pulse. Each scan was repeated 32 times. The sequence advanced four times in order to cover the entire span of the waveform. The total mapping duration time required for each gradient waveform was 4 seconds. The conjugate gradient waveform (opposite polarity) of each sector was also mapped.

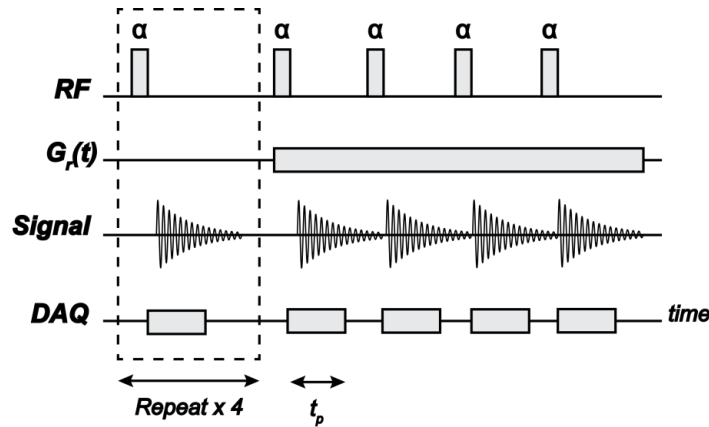


**Figure A-2:** Pulse sequence diagram for the MFGM acquisition to measure the gradient waveform. Small tip angle RF pulses were applied to produce a FID from the phantom. A series of points for each acquisition during phase-encoding time  $t_p$  were sampled.

The impulse response obtained with MFGM was optimized as a pre-emphasized input gradient waveform to provide a desired final gradient response for each sector. **Figure A-3** shows the ideal and pre-emphasized *Sectoral*  $x$ -axis and  $y$ -axis waveforms of the 11<sup>th</sup> sector. The waveforms had a higher number of data points ( $N = 1432$ ) than required for encoding in order to locally smooth each waveform in order to minimize sharp changes in the encoding gradients.

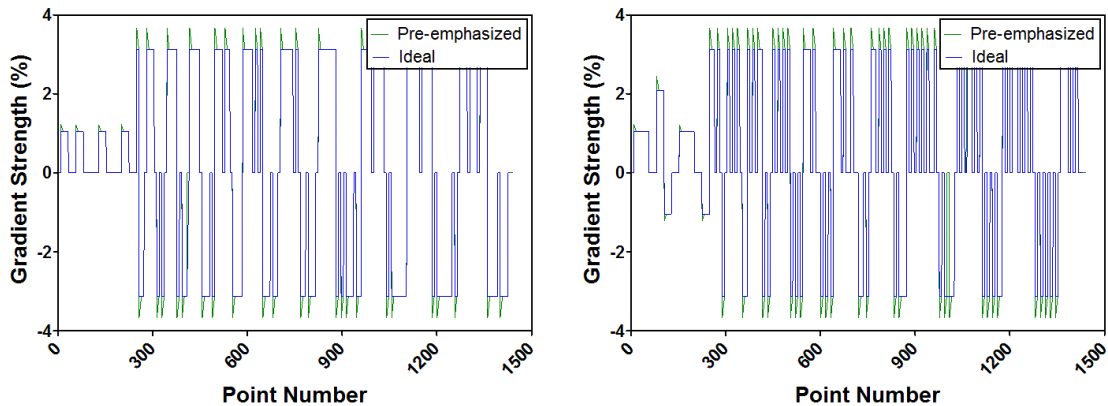


**Figure A-3:** Pre-emphasized (green) and ideal (blue) trajectories through  $k$ -space, or frequency-encoding waveform, for the  $x$ -axis (left) and  $y$ -axis (right) gradient of the 11<sup>th</sup> sector.

Every 8<sup>th</sup> data point from the waveform (**Figure A-4**) corresponded to an individual spatial frequency that related to a point directly on a Cartesian grid. The waveform was integrated to produce the pre-emphasized gradient waveforms in  $x$  and  $y$  (**Figure A-5**) required for the *Sectoral* traversal  $k$ -space trajectory.

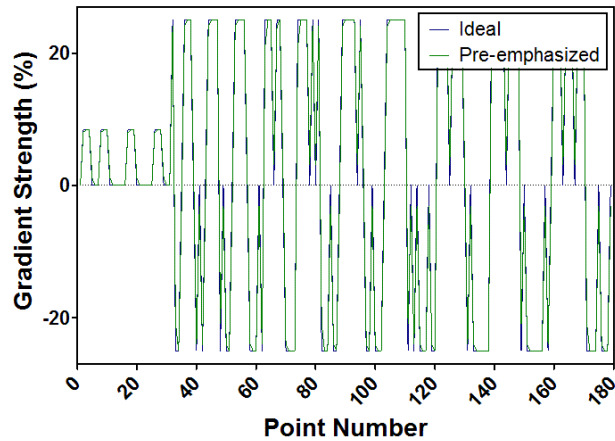


**Figure A-4:** Reduced pre-emphasized (green) and ideal (blue) trajectories through  $k$ -space, or frequency-encoding waveform, for the  $x$ -axis gradient of the 11<sup>th</sup> sector.

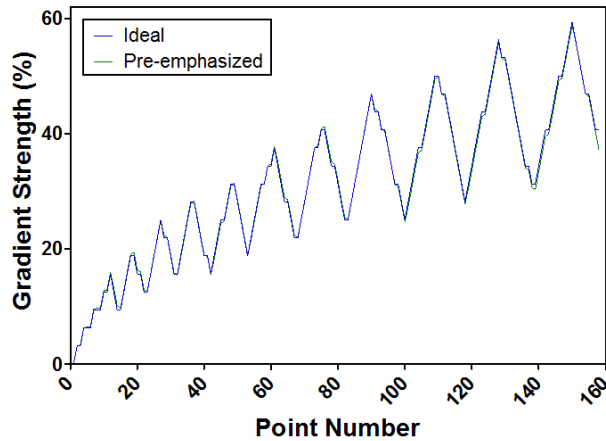


**Figure A-5:** Pre-emphasized (green) and ideal (blue) trajectories through  $k$ -space, or pure phase-encoding waveform, for the  $x$ -axis gradient of the 11<sup>th</sup> sector.

The MFGM technique provides the waveforms proportional to the gradient strength. Therefore, to correct the waveforms, a stepwise input waveform was used in conjunction with a corresponding output waveform (**Figure A-6**) to determine a normalization coefficient. The coefficient was calculated using IDL (Exelis Visual Information Solutions, Boulder) by minimizing the following function with respect to  $n$ :

$$\sum_{i=0} |G_{input} - n \cdot G_{mapped}|, \quad [A.2]$$

where the strengths of the input gradient,  $G_{input}$ , and mapped gradient  $G_{mapped}$ , were used to find the normalization coefficient,  $n$ . The summation was performed over all data points in the gradient waveform. A normalization coefficient was determined independently for each mapped gradient waveform.

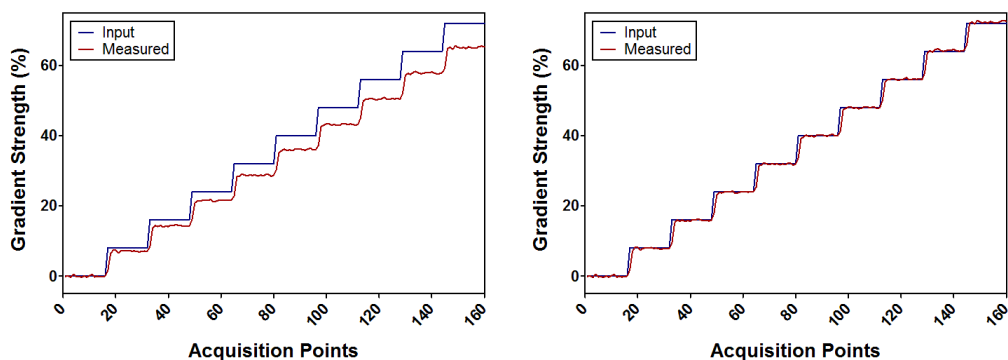


**Figure A-6:** Measured gradient waveforms without (left) and with (right) coefficient correction. The prescribed input waveform (blue) was stepwise with each gradient step corresponding to 24 points (24  $\mu$ s) and measured waveform (red) experienced within the sample space.

## A.2 Results

The  $x$ -axis and  $y$ -axis *Sectoral* gradient waveforms were mapped for all 16 sectors. Similar measured trends were observed in all the mapped waveforms. **Figure A-7** shows the pre-emphasized input waveform for the  $x$ -axis gradient of the 11<sup>th</sup> sector compared to the average measured waveform after correction with the normalization coefficient. A strong agreement between the input and measured waveforms was observed during gradient rise and fall times.

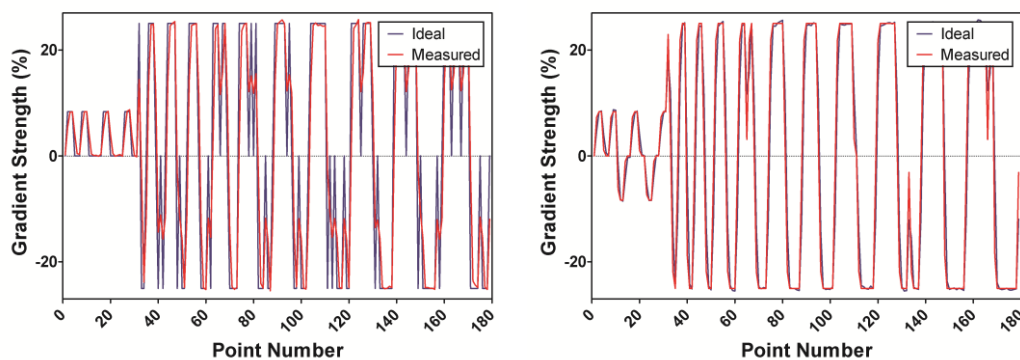


**Figure A-7:** Representative input (blue) and measured (red) *Sectoral* trajectories through  $k$ -space, or frequency-encoding waveform, for the  $x$ -axis gradient of the 11<sup>th</sup> sector (left) and the  $y$ -axis gradient of the 12<sup>th</sup> sector (right).

**Figure A-8** shows the pure phase-encoding  $x$ -axis gradient waveform for the 11<sup>th</sup> sector after integration. The waveforms for a  $64 \times 64$  *Sectoral* acquisition acquire 158  $k$ -space Cartesian data points per sector. These points are sampled with a dwell time of  $90 \mu\text{s}$  for  $^{129}\text{Xe}$  and  $35 \mu\text{s}$  for  $^1\text{H}$ . The total duration (i.e. readout time) of a single gradient waveform is 129 ms for  $^{129}\text{Xe}$  and 50 ms for  $^1\text{H}$ . The eddy currents yield a smooth *Sectoral* waveform compared to the input waveform.

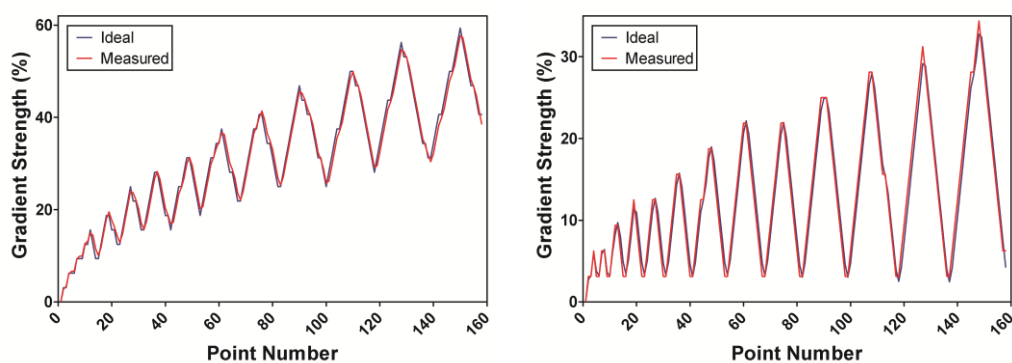


**Figure A-8:** Representative ideal (blue) and measured (red) *Sectoral* trajectories through  $k$ -space, or pure phase-encoding waveform, for the  $x$ -axis gradient of the 11<sup>th</sup> sector (left) and the  $y$ -axis gradient of the 12<sup>th</sup> sector (right).

## Appendix B: Histological Interpretation

The mean linear intercept,  $L_m$ , was measured by placing a 4×3 grid over each image. The vertical and horizontal lines were 1.33 mm and 1 mm respectively. The total numbers of intercepts were automatically counted using a MATLAB code. The  $L_m$  was then determined by dividing the line length ( $l$ ) by the number of intercepts ( $N_i$ ):

$$L_m = \frac{l}{N_i} . \quad [\text{B.1}]$$

The frequency of the intersected tissue with the grid was also hand counted to confirm the accuracy of the MATLAB codes. The total intercepts per slide are reported below in **Table B-1**.

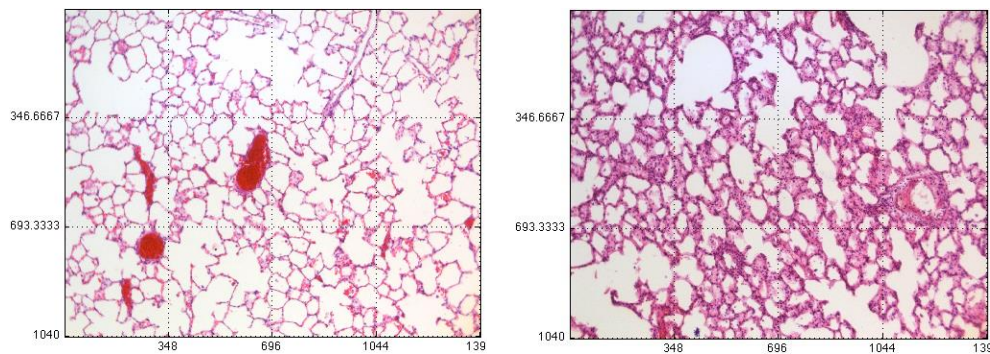


**Figure B-1:** H&E stained histology. Healthy lung tissue from healthy rat (left). Damaged rat lung tissue two weeks post irradiation treatment (right). This specimen shows clear thickening of the alveolar septa compared with the healthy lung, which could reasonably explain the observed correlation in calculated ADC values. However, such thickening was not seen throughout all irradiated lungs which factors into the results.

**Table B-1:** Representative average  $L_m$  values of each rat cohort.

	Irradiated	Healthy
$L_m$ Left-Top ( $\mu\text{m}$ )	68	54
$L_m$ Left-Middle ( $\mu\text{m}$ )	53	56
$L_m$ Right-Top ( $\mu\text{m}$ )	47	61
$L_m$ Right-Middle ( $\mu\text{m}$ )	57	59
$L_m$ Average ( $\mu\text{m}$ )	56.3	57.5



## Appendix C: Animal Use Protocol Approval



2007-083-09::6:

**AUP Number:** 2007-083-09

**AUP Title:** Assessment of Lung Function and Structure in Anaesthetized and Ventilated Rats Using Hyperpolarized Noble Gas Magnetic Resonance Imaging and Xenon-enhanced Computed Tomography

**Yearly Renewal Date:** 11/01/2013

**The YEARLY RENEWAL to Animal Use Protocol (AUP) 2007-083-09 has been approved, and will be approved for one year following the above review date.**

1. This AUP number must be indicated when ordering animals for this project.
2. Animals for other projects may not be ordered under this AUP number.
3. Purchases of animals other than through this system must be cleared through the ACVS office.  
Health certificates will be required.

### **REQUIREMENTS/COMMENTS**

Please ensure that individual(s) performing procedures on live animals, as described in this protocol, are familiar with the contents of this document.

The holder of this Animal Use Protocol is responsible to ensure that all associated safety components (biosafety, radiation safety, general laboratory safety) comply with institutional safety standards and have received all necessary approvals. Please consult directly with your institutional safety officers.

Submitted by: Kinchlea, Will D  
on behalf of the Animal Use Subcommittee  
University Council on Animal Care



## Curriculum Vitae

### KRZYSZTOF WAWRZYN

#### EDUCATION

---

<b>M.Sc. (Medical Biophysics) candidate</b> <i>Western University</i>	<b>2012 – 2014</b> <i>London, ON</i>
<b>B.Sc. (Medical Physics)</b> <i>Ryerson University</i>	<b>2007 – 2012</b> <i>Toronto, ON</i>
<b>Diploma (Computer Systems Technician)</b> <i>Fanshawe College</i>	<b>2003 – 2006</b> <i>London, ON</i>

#### PUBLICATIONS

---

**Wawrzyn K**, Demidov V, Vuong B, Harduar MK, Sun C, Yang VXD, Doganay O, Toronov V, and Xu Y. “*Imaging the Electro-kinetic Response of Biological Tissues with Optical Coherence Tomography*”. *Optics Letters* 38, no. 14 (2013): 2572-2574.

#### CONFERENCE PROCEEDINGS

---

**Wawrzyn K**, Vuong B, Harduar MK, Yang VXD, Demidov V, Toronov V, Xu Y. “*Monitoring Electric Current in Biological Tissues by Optical Coherence Tomography*”. *Biomedical Optics* (2012): BW2A.4.

#### POSTERS AND TALKS

---

**Wawrzyn K**, Ouriadov A, Hickling S, Hegarty E, Santyr G. “*A Pseudo Non-Cartesian Pulse Sequence for Hyperpolarized Xenon-129 Gas Imaging of Rodents at Low Magnetic Field Strength*”. 2014 London Imaging Discovery, London, Canada (Poster).

**Wawrzyn K**, Ouriadov A, Hickling S, Hegarty E, Santyr G. “*A Pseudo Non-Cartesian Pulse Sequence for Hyperpolarized Xenon-129 Gas MRI of the Lungs at Low Magnetic Field Strength*”. 2014 Imaging Network Ontario Symposium, Toronto, Canada (Poster).

Doganay O, Wade T, Hegarty E, **Wawrzyn K**, McKenzie C, Santyr G. “*Hyperpolarized <sup>129</sup>Xe Imaging of the Lung using Spiral IDEAL*”. 2014 Imaging Network Ontario Symposium, Toronto, Canada (Poster).

Hegarty E, Engelberts D, Wade T, **Wawrzyn K**, Doganay O, Kavanagh B, Santyr G. “*Hyperpolarized Xenon-129 MRI for Evaluation of a Continuous Negatively-Applied Pressure (CNAP) Approach for Recruitment of Atelectasis in a Rat Model*”. 2014 American Thoracic Society International Conference, San Diego, USA (Poster).

**Wawrzyn K**, Ouriadov A, Hickling S, Santyr G. “*Implementation of a Novel Non-Cartesian Pulse Sequence for MRI of the Lungs with Hyperpolarized <sup>129</sup>Xe*”. 2013 London Imaging Discovery, London, Canada (Poster).

**Wawrzyn K**, Ouriadov A, Hickling S, Santyr G. “*Development of a non-Cartesian pulse sequence for MRI of the lungs with hyperpolarized  $^{129}\text{Xe}$* ”. Submitted to the 2013 Imaging Network Ontario Symposium, Toronto, Canada (Talk and poster).

**Wawrzyn K**, Yang VXD, Xu Y. “*The Effects of Electric Current in Biological Tissues on Optical Coherence Tomography Signals*”. Submitted to the 2010 Canadian Association of Physicists Congress, Toronto, Canada (Talk).

## RESEARCH EXPERIENCE

---

**Graduate Research Assistant** 2012 – 2014  
*Robarts Research Institute, Western University* *London, ON*

**Thesis:** A pseudo non-Cartesian pulse sequence for hyperpolarized xenon-129 gas MRI of rodent lungs at low magnetic field strength.

**Research Assistant** 2012  
*Robarts Research Institute, Western University* *London, ON*

Assembled a second generation hyperpolarizer for xenon gas-enhanced MRI.

**Research Assistant** 2011 – 2012  
*Physics Department, Ryerson University* *Toronto, ON*

Designed and utilized experimental setups for therapeutic techniques involving high-intensity focused ultrasound (HIFU), low intensity therapeutic ultrasound (LITU), *ex vivo* ultrasound imaging, and phantom model preparation.

**Research Assistant** 2009 – 2012  
*Physics Department, Ryerson University* *Toronto, ON*

Designed and utilized experimental setups for optical measurements involving *ex vivo* OCT imaging, data acquisition for signal analysis and image processing, optical & electric equipment arrangement, and specimen preparation.

**Undergraduate Thesis Student** 2010 – 2011  
*Physics Department, Ryerson University* *Toronto, ON*

**Thesis:** Demonstrated the feasibility of using optical coherence tomography (OCT) to detect and monitor signal change from electric-field induced biological tissue. Presented poster and submitted thesis in support of B.Sc. degree.

**Research Student** 2009  
*Research Operations, Trojan Technologies* *London, ON*

Cultured cells, disinfected waste water samples by irradiating microorganisms using UV collimator beams, and applied chemistry techniques for filtering, testing, and analyzing water contaminants.